الشعبية الديمقراطية الجزائرية الجمهورية

DEMOCRATIC AND POPULAR REPUBLIC OF ALGERIA

MINISTRY OF HIGHER EDUCATION AND SCIENTIFIC RESEARCH

SETIF 1 UNIVERSITY-FERHAT ABBAS

FACULTY OF TECHNOLOGY

THESIS

Submitted to the Process Engineering Department for

DOCTORATE DEGREE

Option : Electrochemical Engineering

BY

LATOUI Mourad

TITLE OF THE THESIS

Synthesis of new hybrid materials, structural characterization, and study of their electrochemical properties

Defended on 27/02/2025 in front of the Jury:

FOUDIA Malika	**Professor**	**Setif 1 university**	**Chairman**
BENGHANEM Fatiha	**Professor**	**Setif 1 university**	**Supervisor**
AIT YOUCEF Hakima	**M.C. A**	**Setif 1 university**	**Co-supervisor**
DJEDOUANI Amel	**Professor**	**E. N. S. Constantine**	**Reviewer**
TABTI Salima	**M.C. A**	**B. B. A university**	**Reviewer**
OUANOUGHI Yasmina	**Professor**	**Setif 1 university**	**Reviewer**
BOURZAMI Riadh	**M.C. A**	**Setif 1 university**	**Guest**

الجمهورية الجزائرية الديمقراطية الشعبية

République Algérienne Démocratique et Populaire

Ministère de L'Enseignement Supérieur et de la Recherche Scientifique

UNIVERSITÉ SETIF1 FERHAT ABBAS
FACULTÉ DE TECHNOLOGIE

THESE

Présentée au Département de Génie Des Procédés

Pour l'obtention du diplôme de

DOCTORAT

Option : Génie Electrochimique

Par

LATOUI Mourad

THÈME

Synthèse de nouveaux matériaux hybride, caractérisation structurale et étude de leurs propriétés électrochimiques

Soutenue le 27/02/2025 devant le Jury :

FOUDIA Malika	**Professeur**	**Univ. Sétif 1**	**Présidente**
BENGHANEM Fatiha	**Professeur**	**Univ. Sétif 1**	**Directrice de Thèse**
AIT YOUCEF Hakima	**M. C. A**	**Univ. Sétif 1**	**Co-Directrice de Thèse**
DJEDOUANI Amel	**Professeur**	**E. N. S. Constantine**	**Examinatrice**
TABTI Salima	**M. C. A**	**Univ. B. B. A**	**Examinatrice**
OUANOUGHI Yasmina	**Professeur**	**Univ. Sétif 1**	**Examinatrice**
BOURZAMI Riadh	**M. C. A**	**Univ. Sétif 1**	**Invité**

Acknowledgements

First of all, I thank the almighty GOD for giving me the will to accomplish this work.

This work was carried out in the laboratory of Molecular Engineering and Redox Catalysis (LEIMCR) of the Faculty of Technology, Ferhat ABBAS University- Setif-1.

I express my deep gratitude and sincere thanks to Professor Fatiha BENGHANEM, and doctor AIT YOUCEF Hakima for their guidance and for guiding me through this work and the valuable help they have brought me for the achievement of this work and their availability and constant help throughout the work.

My most respectful thanks also go to Professor FOUDIA Malika at F. ABBAS Sétif -1 University for the honor he gave me by agreeing to chair the jury of this thesis.

I express all my gratitude to Professor A. DJEDOUANI at E.N.S. Constantine and doctor TABTI Salima at B.B.A university who did me the honor of participating in this jury and judging this work.

I am equally grateful to Professor OUANOUGHI Yasmina and doctor Professor BOURZAMI Riadh from the University-Ferhat Abbas for agreeing to serve as examiners.

I extend my heartfelt thanks to everyone mentioned above and to all those who have supported me in various ways, big and small. This thesis is the culmination of collective efforts and shared dedication.

Table of contents

Chapter II

Table of contents

Nomenclature

DMSO : dimethyl sulfoxide

$LiClO_4$: lithium perchlorate

N: Avogadro number.

h: Plank constant.

I_p: Peak current intensity (A)

n: Number of electrons transferred

A: Electrode surface (cm^2)

C: Concentration (mol.cm-3)

C_{inh}: Inhibitor concentration.

v: Scan speed (V/s)

D: Diffusion coefficient (cm2/s)

α: Coeficient de transfert

s: Surface (cm^2)

K: Equilibrium constant.

t: Immersion time in solution (minute)

EI_p: Compound inhibitory efficiency calculated using polarization curves

EI_z: Inhibitory efficiency of compounds calculated using impedance spectroscopy

θ_p: Compound recovery rate calculated using polarization curves

θ_z: Compound recovery rate calculated using impedance spectroscopy

i_{corr}: Corrosion current density

E_{corr}: Corrosion potential

$ß_c$: Slope of cathodic plate

$ß_a$: Slope of anodic Tafel

Nomenclature

R_s: Resistance of the solution

R_{tc}: Load transfer resistance

C_{dl}: Double layer capacity

E_a: Activation energy

ΔH^o_a: Activation Enthalpy

ΔS^o_a : entropy of activation

K_{ads}: Adsorption constant

R: Perfect gas constant

T: Temperature (K)

ΔG^o_{ads}: Standard free energy adsorption

Chapter I

Chapter III

Chapter IV

Chapter V

Chapter I

Chapter III

Chapter IV

Chapter III

Chapter IV

Chapter V

General Introduction

General Introduction

Scientists and engineers realized early on that mixtures of materials can show superior properties compared with their pure counterparts. One of the most successful examples is hybrid materials which are formed by two moieties blended on the molecular scale. Most of the resulting materials show improved thermal stability, mechanical and optical properties [1-9].

Hybrid materials are emerging as a very potent and promising class of materials. The complementarity results in a complete synergy of the desired material's properties and ultimately an end-product. The diversity of the resulting properties and materials used in the production of hybrid materials applies to a wide variety of applications, from automotive and structural applications to electronics and biomedical applications [10-17].

In recent years, multifunctional materials, are the most advanced and high engineering materials that can exhibit interesting properties nonlinear optical behavior and are featured with high thermal stability, fatigue resistance along with enhancing the chemical and environmental resistance [15,17]. A systematic design concept for of hybridization of functions is required for the development of new functionally-hybridized materials with superior properties and new functions.

Currently, there are four major topics in the synthesis of inorganic-organic materials: their molecular engineering, their nanometer and micrometer-sized organization, the transition from functional to multifunctional hybrids, and their combination with bioactive components.

Organic-inorganic hybrid materials can be applied in many branches of materials chemistry because they are simple to process and are amenable to design on the molecular scale, they are emerging as a promising class of materials with broad applications. These hybrid materials do not represent only a creative alternative to design new materials and compounds for academic research, but their improved or unusual features allow the development of innovative industrial applications. Nowadays, most of the hybrid materials that have already entered the market are synthesized and processed by using conventional soft chemistry-based routes developed in the eighties.

Organic-inorganic materials containing partially 2,4,6-triamino-1,3,5-triazine (melamine) as organic part improved or unusual features allow the development of innovative industrial applications and exhibiting a good thermal stability. Melamine has a

wide application in the industry, is known as an important raw material, is widely used as a fire-retardant additive for polymeric materials and used to form hybrid materials. Those materials containing s-triazine moiety as organic part, give improved hydrolytic and thermal stability. Melamine and related triazine derivatives can form self-assembling, high molecular weight complexes via organized intramolecular networks of hydrogen bonds and π-π aromatic ring stacking [18,19]. In this context, we have synthesized two new organic-inorganic hybrid ionic materials as single crystals based on melamine:

- Tris (2,4,6-triamino-1,3,5-triazinium) monodrogenphosphate dihydrogenphosphate tetrahydrate ($3C_3H_7N_6^+.HPO_4^{2-}.H_2PO_4^-.4H_2O$) (Hyb1).

- Tris (2,4,6-triamino-1,3,5-triazinium) perchlorate monohydrate ($C_3H_7N_6^+.ClO_4^-.H_2O$) (Hyb2).

In addition, we studied the electrochemical behavior of these hybrid materials and their corrosion inhibition performance.

This thesis is presented in five chapters.

- The first chapter presents bibliographic research on organic-inorganic hybrid materials, melamine, chemical of coordination and general notions about corrosion and corrosion inhibitors.

- The second chapter describes experimental physicochemical methods, single-crystal X-ray diffraction (SXRD), Hirshfeld surface analysis and electrochemical methods used in this work.

- The third chapter and the fourth chapter presents the synthesis of the two new hybrid ionic, their affined, studied molecular structures using single crystal X-ray diffraction, Hirshfeld surfaces analysis, their characterized spectroscopic UV-Vis and FT-IR. The study of their thermal decomposition was also studied by TGA/DTG techniques. Otherwise, the synthesis of the new copper complex using Hyb2 as ligand, its characterized by UV-Vis and FT-IR spectroscopy and its thermal decomposition by means of TGA/DTG was mentioned in fourth chapter.

- The last chapter presents the results obtained from the study of the electrochemical properties of the two hybrid materials and their inhibitory action against corrosion of carbon steel X48 in aggressive medium HCl 1 M.

- Finally, a general conclusion crowns this manuscript and some perspectives.

References

[1] C. Sanchez, F. Ribot, Design of hybrid organic-inorganic materials synthesized via sol-gel chemistry, New. J. Chem. 18(10) (1994) 1007-1047.

[2] L. Nicole, C. Laberty-Robert, L. Rozes, C. Sanchez, Hybrid materials science: a promised land for the integrative design of multifunctional materials. Nanoscale. 6(12) (2014) 1-25.

[3] C. Sanchez, G. J. A. A. Soler-Illia, F. Ribot, T. Lalot, C. R. Mayer, V. Cabuil, Designed hybrid organic−inorganic nanocomposites from functional nanobuilding blocks, Chem. Mater. 13 (2001) 3061-3083.

[4] D. B. Mitzi, Thin-film deposition of organic− inorganic hybrid materials, Chem. Mater., 13 (2001) 3283-3298.

[5] E. Cordoncillo, P. Escribano, F. J. Guaita, C. Philippe, B. Viana, C. Optical properties of lanthanide doped hybrid organic-inorganic materials Technol, J. Solgel. Sci. Technol. 24 (2002) 155-165. https://doi.org/10.1023/A:1015204227347.

[6] C. Sanchez, B. Lebeau, F. Chaput, J. P. Boilot, Optical properties of functional hybrid organic–inorganic nanocomposites, Adv. Mater. 15 (2003) 1969-1994.

[7] F. Mammeri, E. L. Bourhis, L. Rozes, C. Sanchez, Mechanical properties of hybrid organic–inorganic materials, J. Mater. Chem. 15 (2005) 3787-3811.

[8] C. Sanchez, B. Julian, P. Belleville, M. Popall, Applications of hybrid organic–inorganic nanocomposites, J. Mater. Chem. 15 (2005) 3559-3592.

[9] M. A. Iramain, A. E. Ledesma, S. A. Brandán, Structural properties and vibrational analysis of Potassium 5-Br-2-isonicotinoyltrifluoroborate salt. Effect of Br on the isonicotinoyl ring, J Mol. Struct. 1184 (2019) 146-156.

[10] C. Sanchez, P. Belleville, M. Popall, L. Nicole, Applications of advanced hybrid organic-inorganic nanomaterials: from laboratory to market. Chem. Soc. Rev. 40(2) (2011) 696-753.

[11] E. Coronado, J. R. Galán-Mascarós, C. J. Gómez-García, V. Laukhin, Coexistence of ferromagnetism and metallic conductivity in a molecule-based layered compound. Nature. 408(6811) (2000) 447-449.

[12] D. B. Mitzi, Thin-film deposition of organic-inorganic hybrid materials, Chem. Mater. 13(10) (2001) 3283–3298.

[13] A. J. Waddon, E. B. Coughlin, Crystal structure of polyhedral oligomeric silsequioxane (poss) nano-materials: a study by x-ray diffraction and electron microscopy, Chem. Mater. 15(24) (2003) 4555–4561.

[14] W. Eerenstein, N. D. Mathur, J. F. Scott, Multiferroic and magnetoelectric materials, Nature. 442(7104) (2006) 759-765.

[15] Y. Chen, L. Chen, G. Qi, H. Wu, Y. Zhang, L. Xue, P. Zhu, P. Ma, and X. Li, Self-assembled organic-inorganic hybrid nanocomposite of a perylenetetracarboxylic diimide derivative and CdS, Langmuir, 26(15) (2010) 12473-12478.

[16] M. Sessolo and H. J. Bolink, Hybrid organic-inorganic light-emitting diodes, Adv. Mater. 23(16) (2011) 1829–1845.

[17] M.A. Iramain, A.E. Ledesma, S.A. Brandán, Structural properties and vibrational analysis of Potassium 5-Br-2-isonicotinoyltrifluoroborate salt. Effect of Br on the isonicotinoyl ring, J Mol. Struct. 1184 (2019) 146-156.

[18] C. T. Seto, G. M. Whitesides, Molecular self-assembly through hydrogen bonding: supramolecular aggregates based on the cyanuric acid-melamine lattice. Journal of the American Chemical Society, 115(3) (1993) 905-916.

[19] G. M. Whitesides, J. P. Mathias, C. T. Seto, Molecular self-assembly and nanochemistry: a chemical strategy for the synthesis of nanostructures. Science, 254(5036) (1991) 1312-1319.

Chapter I:
Bibliographic synthesis

The present chapter provide bibliographic research on hybrid organic-inorganic materials and those based on melamine and their applications. A general description of melamine was also mentioned. In addition, we recall notions about corrosion and corrosion inhibitors in a general way. We will then present a synthesis of some work on hybrids and in particular those derived from melamine.

I.1. Hybrid organic–inorganic materials

I.1.1. Definition

Hybrid organic–inorganic materials are formed by two moieties blended on the molecular scale. Commonly one of these compounds is inorganic and the other one organic.

The main idea in development of the hybrid materials was to take advantage of the best properties of each component that forms a hybrid, trying to decrease or eliminate their drawbacks getting in an ideal way a synergic effect; that results in the development of new materials with new properties.

The design of hybrid to get the best out of two different chemical worlds, frequently with complementary strengths, to form new materials with new or improved properties [1]. The main challenge is synthesizing hybrid combinations that keep or enhance the best properties of each component while eliminating or reducing their particular limitations. Undertaking this challenge provides an opportunity for developing new materials with synergic behavior leading to improved performance or new useful properties [1]. The inorganic components provide mechanical, thermal, whereas the organic features introduce flexibility into the framework and change the optical properties of the solid [2,3].

I.1.2. Classification

According to the nature of the interactions between organic and mineral components, Sanchez [4] distinguishes two types of hybrids depending on the arrangement of these constituents. Class **I** hybrid materials are those that show weak interactions between the two phases, such as van der Waals, hydrogen bonding or weak electrostatic interactions (Scheme II.1.a). Class **II** hybrid materials are those that show strong chemical interactions between the components (Scheme II.1.b). Because of the gradual change in the strength of chemical

interactions, it becomes clear that there is a steady transition between weak and strong interactions.

a.

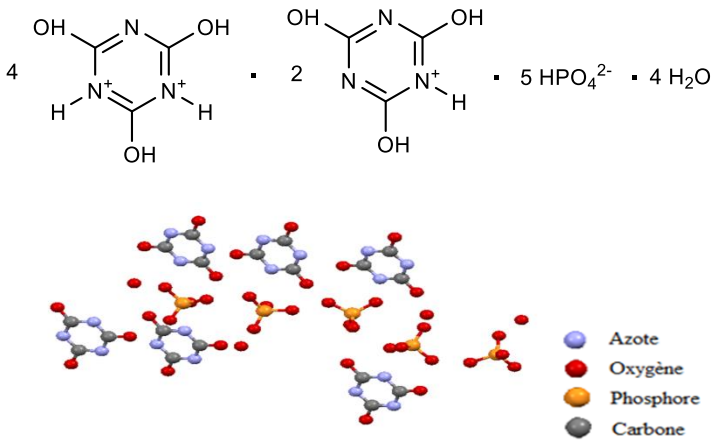

Tetrakis (trihydoxy-2,4,6-triazin-1,3-diium-1,3,5) bis (2,4,6-trihydroxy-2,4,6-triazin-1-ium-1,3,5) pentakis (monohydrogenphosphate) tetrahydrate

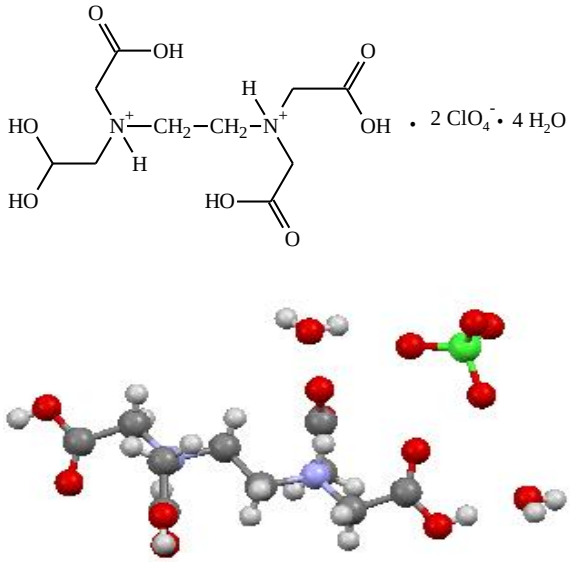

Ethylenediamin-1,2-iumtetraacetic acid bis perchlorate tetrahydrate

b.

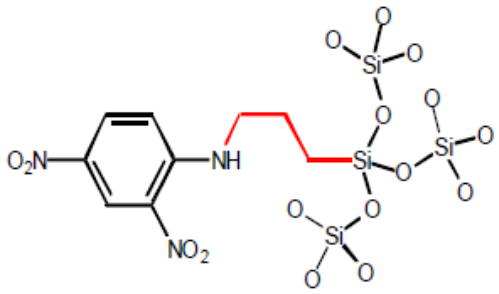

Scheme I.1. Examples of hybrid a. class I, b. class II

I.1.3. Synthesis of hybrid materials

Inorganic–organic hybrids can be applied in many branches of materials chemistry because they are simple to process and are amenable to design on the molecular scale. Currently, there are four major topics in the synthesis of inorganic–organic materials: (a) their molecular engineering, (b) their nanometer and micrometer-sized organization, (c) the transition from functional to multifunctional hybrids, and (d) their combination with bioactive components.

I.2. Hybrid organic–inorganic materials based on 2,4,6-triamino-1,3,5-triazine (melamine)

Hybrid materials based on melamine form the class of solid-state compounds that crystallize with interesting hydrogen-bond networks. Generally, these hybrids have an interesting aspect concerning the hydrogen bond system formed [5-9]. Furthermore, melamine is used for the synthesis of the supramolecular structures and high molecular architectures [10-12]. It is also a famous organic base with a 1,3,5-triazine skeleton, an excellent H-atom donor and acceptor and has been widely utilized to create one-, two- and three-dimensional motifs in combination with various acids [13]. Several researchers have already studied the thermal behavior of melamine and its hybrid materials [14-17].

Some of the crystal structure of hybrids materials contain 2,4,6-triamino-1,3,5-triazin-1-ium (melamine mono- protonated) (schema I.2.a) and 2,4,6-triamino-1,3,5-triazin-1-3-diium (schema I.2.a) melamine double- protonated were published. The both melamine mono-protonated or double-protonated are named melaminium for exemples: melaminium bis (trichloroacetate) dihydrate [18], melaminium chloride hemihydrate [19].

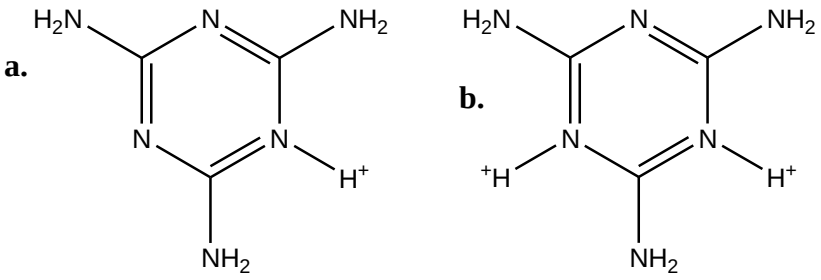

Schema I.2. schema of a. melamine mono- protonated, b. melamine double- protonated

In order to develop materials and devices with innovative properties, in this present work, we have synthesized a new organic-inorganic ionic materials based on melamine.

I.2.1. Description of 2,4,6-triamino-1,3,5-triazine (melamine)

2,4,6-triamino-1,3,5-triazine commonly known as melamine, was first prepared in 1834 by Justus von Liebig [17]. It is an organic chemical commonly found in the form of white crystals rich in nitrogen, it contains 67% nitrogen by mass, is an organic base with pKa of 5. The melamine is characterized by a melting point as high as 345 °C, is a thermally stable crystalline product it is only slightly soluble in water and insoluble in several organic solvents. Melamine can be produced from three different starting materials: urea, dicyandiamide or hydrogen cyanide. Commercially produced melamine is manufactured using urea as a starting material (Scheme **I.3**) [20,21]. There are differences in the literature regarding the manufacture of melamine from dicyandiamide. Some sources indicate that commercial production of melamine from the thermal condensation of dicyandiamide ceased during the 1980 [21]. However, other sources indicate that this process is still used to manufacture melamine [22]. It does not appear that production of melamine from hydrogen cyanide is used commercially.

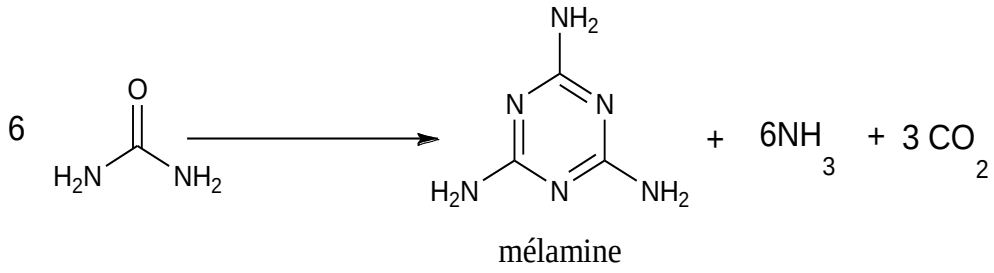

Scheme I.3. Reaction of the production of melamine.

I.2.2. Uses and manufactory of melamine

Since the development of melamine-formaldehyde (MF) resins in the 1930 [23], melamine has gained more and more industrial importance. It represents an important starting material for several industrial applications, such as the fire proof materials [24,25], it acts as a flame retardant [1-3,26] because of its high thermal stability. In addition, it is widely used in plastics, adhesives, countertops, dishware, and whiteboards, it can also be used as a colorant and fertilizer. Other applications of melamine can be given in the area of reinforced plastics, sheet molding compounds etc., [11,12].

Melamine is a manufactured wood similar to particle board, but melamine is exceptionally stronger. Today, many homeowners that are concerned with preserving sustainable resources are choosing melamine as an alternative to hardwood cabinetry.

Melamine and its derivatives are an important class of organic compounds due to the broad variety of their applications as industrial chemicals in the manufacture of dyes, plastics, fertilizers, textiles and its polymers play an important role in technological applications and they are widely used as fire retardant additive systems for polymeric materials.

Melamine is an organic base which is able to form stable organic-organic and organic-inorganic materials with most organic and inorganic acids and exhibit interesting properties [9,27,28]. Many of these materials, such as those with boric acid, phosphoric acid, polyphosphoric acid, cyanuric acid, and sulfuric acid, are either commercial or have the potential to be viable as flame-retardant additives [24,25].

Furthermore, melamine is a planar compound nitrogen-rich, with the ability to form both mono- and deprotonated cations. Its use in the design of hydrogen-bonded supramolecular aggregates is well known [7-9,27,29-31].

An interesting supramolecular assembly based on melamine molecule was recently discovered by Rao and al. [25], it is a planar compound nitrogen-rich, with the ability to form salts containing both mono and diprotonated melaminium cations used in the design of hydrogen-bonded supramolecular aggregates is well known. Furthermore, melamine is used for the synthesis of supramolecular structures and high molecular architectures [32]. It is also a famous organic base with a 1,3,5-triazine skeleton, is an excellent H-atom acceptor and has been widely utilized to create one-, two- and three-dimensional motifs in combination with various

acids [13]. Melaminium may have organic and inorganic ionics which can develop well defined non-covalent architectures via multiple hydrogen bonds, since they contain complementary arrays of hydrogen bonding sites [32].

For example: tetrakis (2,4,6-triamino-1,3,5-triazin-1,3-diium) bis (2,4,6-triamino-1,3,5-triazin-1-ium) pentakis (monohydrogenphosphate) tetrahydrate

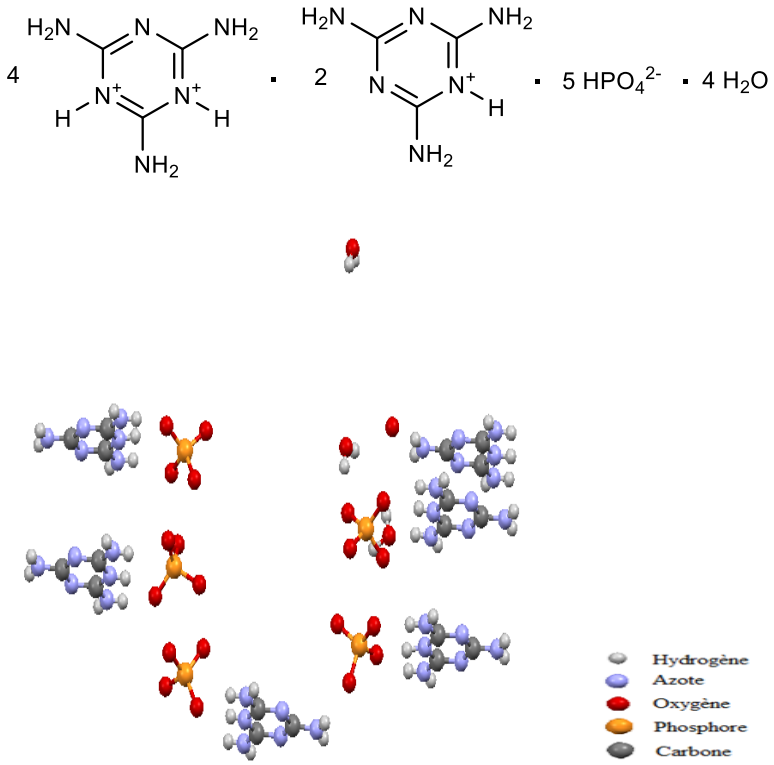

I.3. Applications of hybrid materials

Hybrid materials do not represent only a creative alternative to design new materials and compounds for academic research, but their improved or unusual features allow the development of innovative industrial applications. Looking to the future, there is no doubt that these new generations of hybrid materials, born from the very fruitful activities in this research field, will open land of promising applications in many areas: optics, mechanics, electronics, energy, environment...etc.

The application areas of hybrids include:

- Decorative coatings obtained by the embedding of organic dyes in hybrid coatings.
- Scratch-resistant coatings with hydrophobic or anti-fogging properties.

- Fire retardant materials for construction industry.
- Proton conducting membranes used in fuel cells.
- Corrosion protection
- Supramolecular

The scope of application of hybrid material is extremely broad and touches all aspects of everyday life, namely, chemistry, pharmaceutical industry, medicine as well as biology. These applications are not limited to the laboratory scale, but have been extrapolated to the industrial scale, being among the most exploited innovative systems in the field of research. In this context, some areas of application are mentioned.

I.3.1. Hybrid porous materials

Porous materials are substances characterized by the presence of voids or empty spaces within their structure, which allows them to absorb or contain gases, liquids, or solids. These voids can range in size from nanometers to millimeters and can be interconnected or isolated. Hybrid porous solids result from the interaction between organic and inorganic species to build up three-dimensional frameworks whose skeleton contains both organic and inorganic moieties only linked by covalent bonds, at variance to supramolecular chemistry, such as metal-organic frameworks [6].

I.3.2. Hybrid lamellar materials

Hybrid lamellar material refers to the structures composed of lamellar phases derived from different materials or systems. These hybrid lamellar materials might combine layers or lamellae from disparate sources, resulting in materials with unique properties or functionalities. A way to obtain a directly functionalized lamellar structure is the sol-gel process which has been used to prepare many layered magnesium, nickel, aluminum, and Mg-Al silsesquioxane hybrids [2].

I.3.3. Supramolecular hybrid materials

Supramolecular hybrids are materials that integrate supramolecular chemistry concepts with hybrid material structures, often involving the assembly of organic and inorganic components. These hybrids are designed to exhibit emergent properties or functionalities

resulting from the synergistic interactions between the supramolecular motifs and the diverse components of the hybrid system. Molecular self-assembly is the spontaneous association of molecules under equilibrium conditions into stable aggregates, joined by noncovalent bonds, with well-defined composition and structure [15].

Supramolecular coordination complexes are well-defined, discrete 2D or 3D molecular entities with suitable metal centers undergoing coordination-driven self-assembly with ligands containing multiple binding sites. The host−guest properties of supramolecular complexes are certainly one of their key features, making them not only interesting architectures but also attractive for a wide range of potential applications in catalysis, fluorescent probe design, and the development of novel therapeutics [16].

I.3.4. Optic properties

Some melaminium based crystals hybrid ionic exhibit interesting properties nonlinear optical behavior (NLO), like second harmonic generation (SHG) because of their non-centrosymmetric structures based on hydrogen-bond interactions have recently been discovered [33-39] and have over the years been subjected to extensive investigation by several researchers for their (NLO) properties used in the field of Photonic and Opto-electronic technologies [40-42], Marchewka and al. [41,43] revealed the suitability of melamine family of crystals for their nonlinear optical properties and future applications, for exemples melaminium bis (trichloroacetate) dihydrate[44], melaminium tartrate monohydrate [45]. The SHG has been observed in case of tetra kis(2,4,6-triamino-1,3,5-triazin-1-ium) bis(selenate)trihydrate [33] and 2,4,6-triamino-1,3,5-triazin-1,3-ium tartrate monohydrate [41]

I.3.5. Properties thermal

Melamine [1-8]. and its hybrid [54-56]. are a conventional material used as a fire-retardant additive for polymeric materials, several researchers have already studied their thermal behavior [57-60]. Many of these hybrids, such as those with boric acid, phosphoric acid, polyphosphoric acid, and sulfuric acid, have the potential to be viable as flame-retardant additives. The presence of triazine ring in their structure gives improved hydrolytic and thermal stability [46].

I.4. Corrosion

I.4.1. Generality

Metal corrosion is widely acknowledged as one of the biggest problems facing human society. It affects not just the economy but also society and the environment since it puts the health and safety of those who live nearby in cities or work in connected industries at risk [61]. Metal corrosion brought on by variations in the surrounding environment or the heterogeneities of the metal itself. For metals and their alloys, acidic aqueous solutions are usually the most aggressive media. Furthermore, inhibitors-compounds added to the media at low concentrations can be used to mitigate or even totally eliminate the influence of corrosion [62]. Consequently, a number of organic compounds have been studied for their role in the corrosion process and are employed as steel corrosion inhibitors in acidic environments. By creating a barrier between a metal's surface and solution, these organic inhibitors can take the place of pre-adsorbed acid and water molecules at the interface [23]. Organic compounds containing heteroatoms including oxygen, nitrogen, sulfur, and phosphorus, as well as aromatic rings and π conjugate bonds, can combine to produce organic inhibitors [24]. Furthermore, the physicochemical characteristics of the molecule, the metallic surface, and the electrolytic solution all influence the adherence of organic inhibitors to metallic surfaces as well as the type of interactions that occur between the molecule and the metal [25].

I.4.2. Corrosion types

Depending on the nature of the material and the characteristics of its environment, two types of corrosion can be distinguished: uniform corrosion and localized corrosion [63-66].

I.4.2.1. Uniform Corrosion

This corrosion is caused by a metal in contact with the electrolyte that continuously moves its anode and cathode zones, which attacks the entire surface of the metal almost uniformly. The rusting of steel plates in seawater is an illustration of this type of corrosion (Figure I.1).

Figure I.1. Uniform corrosion of storage tanks

I.4.2.2. Localized corrosion

It is a localized attack that can develop in depth. It occurs when there is heterogeneity of metal, medium, or the physicochemical conditions existing at the surface. Several types of localized corrosion can be distinguished, which are:

Galvanic Corrosion

Galvanic corrosion occurs when two different metals are in direct electrical contact and exposed to an electrolyte, such as water or saline. The most reactive or less noble metal of the pair becomes the anode and begins to corrode, while the more noble metal becomes the cathode and does not corrode.

Crevice Corrosion

It is due to a difference in oxygen accessibility between two parts of a structure, thus creating an electrochemical cell often called concentration cell. This selective attack of the metal is observed in the cracks and other places not easily accessible to oxygen.

Pitting Corrosion

It occurs in the presence of certain anions, particularly chlorides ions. It is one of the most destructive forms of corrosion. It occurs on metals protected by an oxide film. It usually covers cavities of ten micrometers in diameter and significant depth Figure I.2.

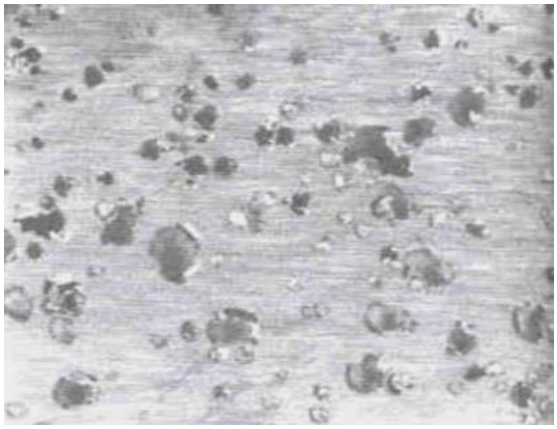

Figure I.2. Localized pitting of stainless steel

Selective corrosion

The formation of a porous metal structure is caused by the oxidation of one component of the alloy compared to another.

Erosion Corrosion

is due to the joint action of an electrochemical reaction and mechanical removal of matter. It often takes place on metals exposed to the rapid flow of a fluid. This type of corrosion affects metals of low hardness

Stress corrosion cracking

The combination of mechanical stress and electrochemical reaction causes the metal to crack.

Intergranular corrosion

It is an attack on the grain joints of the metal or often, there is a precipitation of carbides of oxidizable metals.

I.4.3. Mechanisms of electrochemical corrosion

Electrochemical corrosion results from a succession of reactions that occur at the metal-solution interface. The phenomena of corrosion are the coupling of two reactions:

An anodic metal dissolution reaction (M):

$$M \rightarrow M^{n+} + ne^{-} \qquad \text{I.1}$$

A cathodic reaction for the reduction of the oxidizing agent (Ox)

$$Ox + ne^- \rightarrow Red \qquad I.2$$

The reduction reactions are as follows:

- **Reduction of oxygen**

$$O_2 + 2H_2O + 4e^- \rightarrow 4\ OH^- \qquad I.3$$

- **Reduction of H^+ ions**

$$2H^+ + 2e^- \rightarrow H_2 \qquad I.4$$

When oxygen is absent or at very low concentrations, the most easily reduced element is the H^+ ion. In aerated acid medium oxygen is reduced to water following this reaction:

$$2O_2 + 4H^+ + 4e^- \rightarrow 4H_2O \qquad I.5$$

In neutral or basic medium, oxygen is reduced to hydroxyl. The thermodynamic condition necessary to cause corrosion of a metal M is to have an Ox/red electron acceptor, having a thermodynamic voltage superior to that of the metal.

I.4.4. Protection of metals against corrosion

The avoidance of metal corrosion has been a fundamentally practical concern since the creation of metal technology several millennia ago. Since the noble metals were naturally resistant to corrosion, iron metallurgy was developed by the Celtic tribes 3000 years ago, which marked the beginning of the accumulation of information about how to prevent corrosion. Since then, numerous primary directions have emerged [67]:

- ✓ **Natural passivation**

Certain non-noble metals exhibit corrosion resistance indefinitely, whereas others only do so under specific oxidizing circumstances. One such instance is iron in intense nitric acid contact, a phenomenon that was first identified in 1797. Iron exhibits a metallike surface and is stable in nitric acid, despite dissolving in non-oxidizing acids. The development of an extremely thin layer of protective oxide is the cause.

- ✓ **Inhibition**

Certain chemicals possess the ability to either completely stop corrosion or significantly slow it down. We refer to the compounds as inhibitors. These compounds find application in closed systems such as cooling aggregates.

- ✓ **Phosphatizing**

Iron can have its surface treated to create a thin layer that, although not completely protecting it, slows down the corrosion process and helps subsequent layers stick to the iron. In the auto business, this is currently a widespread procedure.

- ✓ **Conversion coatings**

Certain metals can be treated with oxidizing chemicals, chromate solutions being the preferred choice, to create an oxide coating saturated with chromate ions. Applying this treatment to aluminum, copper, and zinc surfaces is one of the best ways to prevent corrosion. Toxic effects are well-known for chromate ions. This superficial therapy is now prohibited going forward due to political decisions. There hasn't been a comparable effective alternative corrosion protection treatment created as of yet.

- ✓ **Surface coating with another metal with better resistance against corrosion**

One option is to plate the metal layer. Among these, zinc plating is the most significant. However, there are alternative ways to get a metal layer ready, like mechanical plating, which involves spraying or dipping the pieces into a liquid metal bath.

- ✓ **Surface coating with a non-metallic inorganic material like enamel**.

Because the parts may be utilized at greater temperatures thanks to this coating, which covers the surfaces with an isolating material, it is particularly effective. Anodic oxidation and the development of a thick surface oxide layer can result in the production of an intrinsic inorganic coating for some metals. The oxidation of aluminum by the Local process is one instance.

- ✓ **Surface coating with an organic material**.

Although the metallic surface appearance is removed, this is still quite effective. At the very least, the metallic conductivity is warped. Moreover, higher temperatures are not suitable for using the coated parts. Because corrosion can occur beneath the covering, even a little scratch in the coating might have disastrous consequences. Recently, a unique type of organic covering known as inherently conductive polymers has been reported. These substances might possess unique anti-corrosion qualities.

- ✓ **Cathodic protection**

A metal is shielded if it is polarized to a potential that is sufficiently negative to its Nernst potential. The application of an external voltage makes polarization possible. Making a galvanic element out of a metal that is less noble than the metal that needs to be protected is another technique. Magnesium is a characteristic metal for iron. This technique is widely applied in subterranean construction, marine technology, and concrete reinforcements.

I.4.5. Corrosion inhibitors

According to ISO 8044 (International Organisation for Standardisation): "An inhibitor is a chemical substance added to the corrosion system at a concentration chosen for its effectiveness, and which results in a decrease in the corrosion rate without significantly altering the concentration of any corrosive agent contained in the aggressive medium"[68].

I.4.5.1. Inhibitor operating conditions

The nature of the metal: The protection of two metals requires the use of two different inhibitors, because an inhibitor that is effective on iron is not necessarily effective on copper. [70,71].

Inhibitor concentration: It is essential to know the minimum effective concentration to be used, while taking care not to exceed the maximum recommended concentration. [72,73].

Temperature: As a general rule, inhibitors lose their protective properties when exposed to high temperatures [74].

Cleanliness of the metal surface: A clean surface will require less product than one fouled by pre-existing corrosion products [73].

The nature of the environment: the presence of aggressive ions (Cl; SOr, NO;) can modify the behavior of an inhibitor [74].

Compatibility between different additives

Several considerations need to be taken into account when using an inhibitor [75]. These include:

✓ The possibility of its degradation in the liquid medium; the loss of inhibitor can be caused by precipitation, chemical reactions with other substances (such as oxygen), its adsorption on different surfaces (metals, suspended particles, corrosion products, etc.), its degradation by micro-organisms or even its thermal degradation.

✓ Its solubility and ability to disperse properly in the medium.

✓ Its compatibility with other chemical substances presents in the solution.

✓ The risk of forming emulsions; inhibitors often have surface-active properties that can lead to the formation of emulsions, which are sometimes difficult or even impossible to separate.

I.4.5.2. Classification of inhibitors

There are several possible ways of classifying inhibitors, which differ from one another in various ways [76]:

✓ The nature of the products (organic or mineral inhibitors).

✓ Their electrochemical mechanism of action (cathodic, anodic or mixed inhibitors).

✓ Based on their interface mechanisms and principles of action (adsorption to the metal surface and/or formation of a protective film).

✓ From the field of application.

a- Nature of inhibitor

➢ **Organic inhibitors**

Organic inhibitors are an essential group of corrosion inhibitors. Their effectiveness depends on the structure, concentration and chemical properties of the layer formed under specific conditions. The action of an organic inhibitor is the result of its adsorption to the surface of the material. Once adsorbed to the surface, they have a dual action, simultaneously slowing down the anodic and cathodic processes. Most of these inhibitors have nitrogen, sulphur or oxygen atoms in their structure. Inhibitors containing sulphur are more effective than those containing nitrogen, because sulphur is a better electron donor than nitrogen. The main characteristic of these inhibitors is their high effectiveness, even at low concentrations. The inhibitory effect often increases with the molecular weight of the inhibitor. The use of organic inhibitors is preferred for reasons of ecotoxicity.

Some organic inhibitors, such as dicyclohexylamine nitrite, can be transported in the vapor phase (volatile inhibitors). In condensation zones, they undergo hydrolysis, releasing benzoate ions. They must have a vapor pressure such that they can rapidly saturate large volumes. In some cases, impregnated papers (urea + sodium nitrite) can also be used [77].

- **Mineral inhibitors**

Mineral compounds are generally used in environments that are close to neutral, or even alkaline, and more rarely in acidic environments. When they are in solution, these compounds dissociate, and it is often the products of this dissociation that provide the inhibition phenomena, namely anions and cations. The predominant inhibiting cations are mainly Ca^{2+} and Zn^{2+}, and they can form insoluble salts with certain anions such as hydroxide (OH^-). The main inhibiting anions are XO4n-type oxo-anions such as chromates, molybdates, phosphates and silicates [78,79].

Currently, the number of molecules in use is gradually decreasing due to the fact that most effective products have a negative impact on the environment. However, progress has been made with the development of new organic complexes of chromium III and other cations (such as Zn^{2+}), which are both effective against corrosion and non-toxic [80].

b- Classification by mechanism of action

There is no single mode of action for corrosion inhibitors. Indeed, the mechanism of action of any given compound will often depend on the corrosion system (metal/solution) in which it is found. However, whatever the exact mechanism by which each inhibitor acts in the conditions in which it is placed, there are a number of basic considerations that apply to all inhibitors. Since corrosion is essentially an electrochemical process, the inhibitor can only act at one of the elementary reaction stages (transport of species in solution, formation of surface intermediates, adsorption of species to the surface of solid phases, electronic charge transfer).

The inhibitor is unlikely to be involved in the process of transporting electroactive species (oxygen, proton, reaction products) within the solution, so the mechanism of action of an inhibitor is usually to be found in the immediate vicinity of the metal surface. However, in a closed circuit, oxygen can be eliminated, and corrosion is then controlled by simply adjusting the pH to a sufficiently high value.

1. Electrochemical mechanism of action

There are three types of corrosion inhibitor that act by forming a barrier layer on the metal surface. This layer modifies the electrochemical reactions by blocking either the anodic or cathodic sites, by influencing the rate of partial electrochemical reactions [81].

Anodic inhibitors

Also known as passivation inhibitors [82], they react to form protective films, reducing the anodic partial current density and shifting the corrosion potential in a positive direction [83].

If the inhibitor adsorbs preferentially on the anodic dissolution sites of the metal where the following reaction takes place, it is an anodic inhibitor.

$$M \rightarrow M^{n+} + ne^- \qquad I.6$$

The anodic inhibitors react with the Me^{n+} metal ions produced on the anode, generally forming insoluble oxides that deposit on the metal surface as an insoluble film that is impermeable to the metal ion. The hydrolysis of the inhibitors produces OH^- ions.

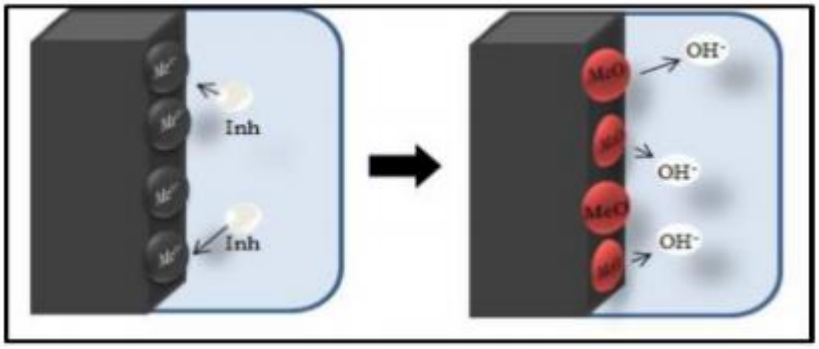

Figure I. 3. Illustration of the effects of anodic inorganic inhibitors and their mechanism of action

Although anodic inhibitors are commonly used and very effective, they generally have a major drawback: if the amount of inhibitor gradually decreases, the metal surface is no longer fully protected and acts as an anode. This creates a dangerous combination of a small anode and a large cathode, leading to pitting corrosion. In this case, the inhibitor does more harm than good, hence their reputation as dangerous substances. However, benzoate ion seems to be an exception, as even a very low concentration of inhibitor only leads to widespread corrosion [77].

Cathodic inhibitors

These inhibitors act by causing the precipitation of a salt or hydroxide on the cathodic surface, thanks to the OH^- ions produced by the reduction of dissolved oxygen during the cathodic reaction. This leads to a reduction in the cathodic partial current density and a shift in the corrosion potential towards more negative values [83].

In a neutral aqueous medium, the following cathodic reaction takes place:

$$O_2 + 2\ H_2O + 4e^- \rightarrow OH^- \qquad I.7$$

It is mainly applied to bare surface areas and stabilizes the protective oxide layer. In an acidic aqueous medium, the cathodic reaction:

$$2\ H^+ + 2e^- \rightarrow H_2 \qquad I.8$$

Cathodic inhibitors create a layer of insoluble precipitates on the metal, covering it. This limits the metal's contact with the environment, even if it is completely immersed, preventing corrosion from occurring. This is why the cathodic inhibitor is concentration-independent and considerably safer than the anodic inhibitor.

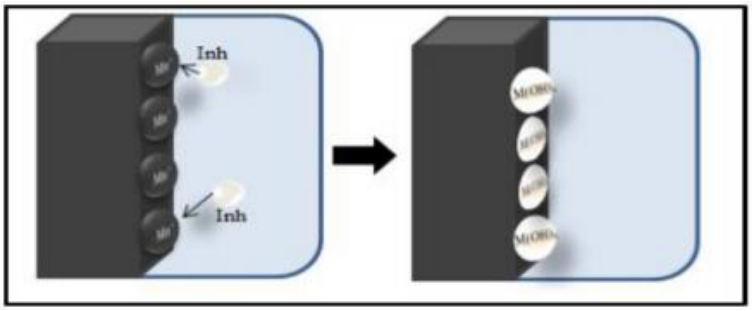

Figure I. 4. Illustration showing the mechanism of action of cathodic inhibitor

Mixed inhibitor

If the inhibitor adsorbs indifferently to both types of sites, it is a mixed inhibitor. They reduce the rate of both partial reactions with little change to the corrosion potential [84].

2. Mechanisms of interfacial action

Inhibitors can be classified according to how they attach to the metal surface. A distinction is made between adsorption or "interface" inhibitors and so-called "interphase" inhibitors. Adsorption inhibitors are mainly present in acidic environments and act by forming

one- or two-dimensional films of molecules that attach to the metal surface. Interphase inhibitors, on the other hand, are specific to neutral or alkaline environments and form threedimensional films that integrate the substrate's dissolution products.

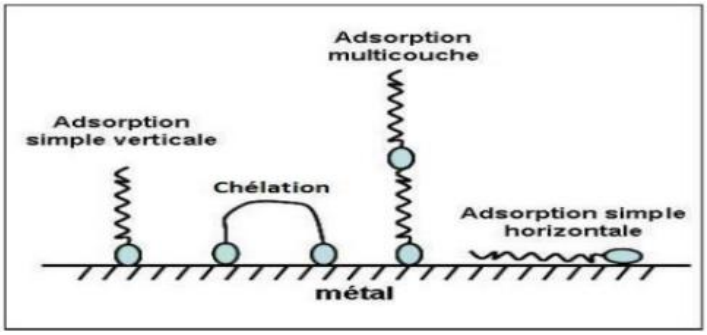

Figure I. 5. Schematic representation of the modes of adsorption of inhibiting organic molecules on a metal surface.

Adsorption is a surface phenomenon that occurs universally because all surfaces are composed of atoms that do not have all their chemical bonds satisfied. Consequently, these surfaces tend to fill this gap by capturing nearby atoms and molecules. The inhibitor/metal surface bond is mainly due to two types of interaction: physisorption, which involves the formation of weak bonds, and chemisorption. The nature and charge of the metal, the chemical structure of the organic product and the type of electrolyte influence these two types of adsorptions [85].

- **Physical adsorption or physisorption**

Physical adsorption results from electrostatic interaction between the ions or dipoles of the organic molecules and the electrically charged metal surface. Dipoles of organic molecules and the electrically charged metal surface. It is linked to the formation of Vander Waals bonds and electrostatic polarisation interactions. Physical adsorption occurs without modifying the molecular structure and the adsorbed molecules can be easily desorbed by reducing the pressure or increasing the temperature [83].

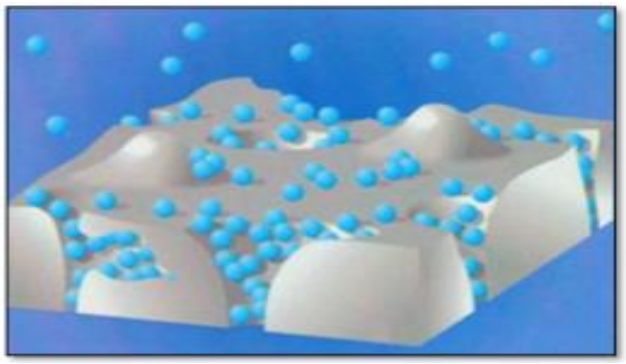

Figure I.6. Physisorption phenomena.

- **Chemisorption**

Chemisorption is a more common mechanism than physisorption and leads to higher inhibitor efficacy. This mechanism involves a transfer of electrons between the metal orbitals and the inhibitor molecule, resulting in the formation of more stable chemical bonds due to the increase in binding energies. Generally, there is a transfer from the donor molecule to the acceptor metal, but there are also cases where the metal is the electron donor and the molecule is the acceptor [86].

Most of the electrons come from the unpaired duplicates of the inhibitor molecules, such as O, N, S, P, etc. (all these atoms are distinguished from the others by their high electronegativity). Chemical adsorption is accompanied by a profound change in the electronic charge distribution of the adsorbed molecules [72].

I.4.5.3. Classification by field of application

Although their use can theoretically be envisaged in most cases of corrosion (with, as main limitations, too large a volume of the corrosive medium or the possible impossibility of incorporating additives), inhibitors have several traditional areas of application

- ✓ Water treatment (sanitary water, industrial process water, boiler water, etc.).
- ✓ The oil industry: drilling, extraction, refining, storage and transport. At all stages of this industry, the use of corrosion inhibitors is essential to safeguard installations.
- ✓ Temporary protection of metals, whether during acid pickling, cleaning of installations or storage in the atmosphere (volatile inhibitors, incorporation into temporary protection oils and greases) or for the treatment of cutting oils.

- ✓ The metal paint industry, where inhibitors are additives used to protect metals against corrosion [84].

I.4.5.4. Adsorption isotherm

Adsorption isotherms are very important in determining the mechanism of organoelectrochemical reactions. The best known are the isotherms of: Langmuir, Frumkin, Hill deBoer, Parsons, Temkin, Flory -Huggins and Dhar -Flory Huggins and Bockris -Swinkels [87]. The most frequently encountered isotherms include:

a- Langmuir isotherm

Langmuir's model assumes that there is a fixed number of sites on the surface. Each of these sites can adsorb only one particle. Furthermore, as interactions between adsorbed particles are neglected, the adsorption energy is constant [88].

The rate of adsorption is proportional to the inhibitor concentration and to the fraction of unoccupied adsorption sites (1 -θ)**.**

$$v_{ads} = (1-\theta)C_{inh} \qquad \text{I.9}$$

b- Temkin isotherm

The adsorption free energy of the adsorbate is a linear function of the recovery rate θ. The chemical rate constants are a function of θ. There is attraction or repulsion between species adsorbed to the surface [89,90]**.** The equation for the Temkin isotherm is expressed as follows:

$$KC_{ads} = \frac{\exp(a\theta)-1}{1-\exp(a(\theta+1))} \qquad \text{I.10}$$

c- Frumki isotherm

The Frumkin isotherm is established by a statistical method and allows interactions between adsorbed molecules to be taken into account. The variation in the recovery rate as a function of concentration is given by the following relationship [83]:

$$KC_{ads} = (1-\theta)^{-1}\exp(-a\theta) \qquad \text{I.11}$$

d-Freundlich isotherm

The Freundlich equation is an empirical model based on adsorption on heterogeneous surfaces. It is used when more than one adsorption monolayer can form on the surface and the sites are heterogeneous with different binding energies [75]**.** The isotherm is expressed by the following equation:

$$\theta = KC_{inh}^{n} \qquad \text{I.12}$$

With:

n: Degree of non-linearity in the relationship between et Cinh ($0 < n < 1$)

a: Interaction constant between adsorbed particles

k: Adsorption coefficient

Cinh: Concentration of inhibitor in the electrolyte.

I.4.5.5. Bibliographic reference

In 2016 H. Ait Youcef and al. [29] synthesized and characterized a new melamine-based hybrid compound. Tetrakis (melamine^{2+}) bis (melamine+) pentakis (monohydrogenophosphate) tetrahydrate was obtained by the reaction of the melamine and phosphoric acid in an acid medium HCl/H_2O. Its structure was identified by X-ray diffraction. The UV-vis absorption spectrum showed that the crystal obtained has a good optical transmittance throughout the visible region. The FT-IR spectrum indicates the presence of functional groups in the hybrid. Several modes of stretching and deformation confirmed the presence of intermolecular hydrogen bonds in the crystal. The TGA-DTA results indicate that tetrakis (melamine^{2+}) bis (melamine^{+}) pentakis (monohydrogenophosphate) tetrahydrate has better thermal stability, making it suitable for thermal applications

The same researchers have found a simple method for synthesizing a new inorganic-organic compound, $4C_3H_5N_3O_3^{2+}.\ 2C_3H_4N_3O^{3+}.\ 5HPO_4^{2-}.4H_2O$ resulting from the reaction of melamine and phosphoric acid in methanol [30]. It was identified using X-ray diffraction on single crystals and characterized using different physicochemical studies.

UV-vis analysis shows good transmittance in the visible range, with an absorption threshold at 255 nm. Thermal behavior shows good thermal stability up to 230°C [30].

H. Ait Youcef and al. [31] prepared and characterized by DRX, UV-vis, FT-IR, FT-Raman and 1H NMR a new hybrid material bis (2,4,6-trihydroxy-1,3,5-triazin-1-ium) bischloride monohydrate ($2C_3H_4N_3O^+$. $2Cl^-$.H_2O).

Spectroscopic and radiographic characterization confirm the structure of the compound. The hybrid shows thermal stability up to 207°C.

References

[1] P. Gomez-Romero, Hybrid Organic-Inorganic Materials In Search of Synergic Activity. Adv. Mater. 13 (3) (2001) 163-174.

[2] M. Jaber, J. Miehe- Brendle, R. L. Dred, New Lamellar Si-Al Inorganic-Organic Hybrid Material. J. Mater. Sci. 39 (4) (2004) 1489-1490.

[3] M. Faustini, L. Nicole, E. Ruiz-Hitzky, C. Sanchez, History of Organic–Inorganic Hybrid Materials: Prehistory, Art, Science, and Advanced Applications. Adv. Funct. Mater. 28 (27) (2018) 1704158.

[4] C. Sanchez, F. Ribot, Design of hybrid organic-inorganic materials synthesized via sol-gel chemistry, New. J. Chem. 18 (10) (1994) 1007-1047.

[5] Y. Sakatani, D. Grosso, L. Nicole, C. Boissière, G. J. de AA Soler-Illia, C. Sanchez, Optimised photocatalytic activity of grid-like mesoporous TiO_2 films: effect of crystallinity, pore size distribution, and pore accessibility. J. Mater. Chem. 16(1) (2006) 77-82.

[6] G. Férey, Hybrid Porous Solids: Past, Present, Future. Chem. Soc. Rev. 37 (1) (2008) 191-214.

[7] H. Rao, M. Chen, H. Ge, Z. Lu, X. Liu, P. Zou, Y. Wang, A novel electrochemical sensor based on Au@ PANI composites film modified glassy carbon electrode binding molecular imprinting technique for the determination of melamine. Biosensors and Bioelectronics. 87 (2017) 1029-1035.

[8] A. Ranganathan, V. R. Pedireddi, C. N. R. Rao, Hydrothermal synthesis of organic channel structures: 1: 1 hydrogen-bonded adducts of melamine with cyanuric and trithiocyanuric acids. J. Am. Chem. Soc. 121(8) (1999) 1752-1753

[9] W. H. Rao, Z. Y. Hu, H. X. Xu, Y. J. Xu, M. Qi, W. Liao, Y. Z. Wang, Flame-retardant flexible polyurethane foams with highly efficient melamine salt. Ind. Eng. Chem. Res. 56(25) (2017) 7112-7119.

[10] S. P. Petrova, V. Christova-Bagdassarian, Migration of Melamine and Formaldehyde from Kids' Bamboo Dinner Sets. J. Food Eng. 2 (2021) 128-136.

[11] H. S. Kim, Y. J. Lee, Y. J. Koo, E. C. Pack, K. M. Lim, D. W. Choi, Migration of monomers, plastic additives, and non-intentionally added substances from food utensils made of melamine–formaldehyde resin following ultraviolet sterilization, Food Chem. 125 (2021) 107981.

[12] I. Ebner, S. Haberer, S. Sander, O. Kappenstein, A. Luch, T. Bruhn, Release of melamine and formaldehyde from melamine-formaldehyde plastic kitchenware. Molecules. 25(16) (2020) 3629.

[13] J. Zieba-Palus, The usefulness of infrared spectroscopy in examinations of adhesive tapes for forensic purposes. Forensic Sci. Criminol. 2(2) (2017) 1-9.

[14] S. Chuhadiya, Himanshu; D. Suthar, S. L. Patel, M. S. Dhaka, Metal Organic Frameworks as Hybrid Porous Materials for Energy Storage and Conversion Devices: A Review. Coord. Chem. Rev. 446 (2021) 214115.

[15] K. Bretterbauer, C. Schwarzinger, Melamine derivatives-a review on synthesis and application. Curr. Org. Synth. 9(3) (2012) 342-356.

[16] J. C. Maxwell, The 21 irrefutable laws of leadership: Follow them and people will follow you. HarperCollins Leadership. (2007).

[17] S. Bizzari, K. Yokose, Melamine. Chemical economics handbook. (2008).

[18] G. J. Perpétuo, J. Janczak, Two crystals of doubly protonated melaminium salts: melaminium bis (trifluoroacetate) trihydrate and melaminium bis (trichloroacetate) dihydrate. Cryst. Struc. Comm. 62(7) (2006) 372-375.

[19] J. Janczak, G. J. Perpétuo, Melaminium maleate monohydrate. Cryst. Struct. Commun. (3) (2004) o211-o214.

[20] S. Ono, T. Funato, Y. Inoue, T. Munechika, T. Yoshimura, H. Morita, C. Shimasaki, Determination of melamine derivatives, melame, meleme, ammeline and ammelide by high-performance cation-exchange chromatography. J. Chromatogr. A. 815(2) (1998) 197-204.

[21] S. Landertshamer, C. Schwarzinger, On the oxidation of allylmelamines. JUnQ. 2(1) (2011) 5-8.

[22] I. Ebner, S. Haberer, S. Sander, O. Kappenstein, A. Luch, T. Bruhn, Release of melamine and formaldehyde from melamine-formaldehyde plastic kitchenware. Mol. 25(16) (2020) 3629.

[23] A. Chaouiki, M. Chafiq, Y. G. Ko, A. H. Al-Moubaraki, F. Z. Thari, R. Salghi, H. Lgaz, Adsorption mechanism of Eco-Friendly corrosion inhibitors for exceptional corrosion protection of carbon steel: electrochemical and First-Principles DFT evaluations. Metals. 12(10) (2022) 1598.

[24] H. Elmsellem, M. H. Youssouf, A. Aouniti, T. Ben Hadda, A. Chetouani, B. Hammouti, Adsorption and inhibition effect of curcumin on mild steel corrosion in hydrochloric acid. Russ. J. Appl. Chem. 87 (2014) 744-753.

[25] A. Kokalj, Molecular modeling of organic corrosion inhibitors: Calculations, pitfalls, and conceptualization of molecule–surface bonding. Corros. Sci. 193 (2021) 109650.

[26] F. Mammeri, E. L. Bourhis, L. Rozes, C. Sanchez, Mechanical Properties of Hybrid Organic–Inorganic Materials. J. Mater. Chem. 15 (35–36) (2005) 3787-3811.

[27] K. Sivashankar, A. Ranganathan, V. R. Pedireddi, C. N. R. Rao, Novel supramolecular organizations in melamine complexes with 4, 4′-bipyridyl and silver nitrate. J. Mol. Struct. 559(1-3) (2001) 41-48.

[28] C. T. Seto, G. M. Whitesides, Molecular self-assembly through hydrogen bonding: supramolecular aggregates based on the cyanuric acid-melamine lattice. JACS. 115(3) (1993) 905-916.

[29] H. C. AitYoucef, S. Chafaa, R. Doufnoune, T. Douadi, Synthesis, characterization and thermal behavior of tetrakis (melamine2+) bis (melamine+) pentakis (monohydrogenphosphate) tetrahydrate. J. Mol. Struct. 1123 (2016) 138-143.

[30] R. Bourzami, H. C. AitYoucef, N. Hamdouni, M. Sebais, Synthesis, crystal structure, vibrational spectra and thermal properties of novel ionic organic-inorganic hybrid material. Chem. Phys. Lett. 711 (2018) 220-226.

[31] H. C AitYoucef, R. Bourzami, Synthesis, single crystal X-ray structure and vibrational spectroscopic characterization study of a new hybrid material crystal: Bis (2, 4, 6-trihydroxy-1, 3, 5-triazin-1-ium) bischloride monohydrate. J. Mol. Struct. 1191 (2019) 218-224.

[32] A. Casini, B. Woods, M. Wenzel, The Promise of Self-Assembled 3D Supramolecular Coordination Complexes for Biomedical Applications. Inorg. Chem. 56 (24) (2017) 14715-14729.

[33] M.K. Marchewka, J. Baran, A. Pietraszko, A. Haznar, S. Debrus, H. Ratajczak, Crystal structure, vibrational spectra and nonlinear optical properties of new melaminium salt: 2,4,6-triamino-1,3,5-triazin-1,3-ium tartrate monohydrate. Solid State Sci. 5 (2003) 509-518.

[34] H. Ratajczak, J. Barycki, A. Pietraszko, J. Baran, S. Debrus, M. May, J. Venturini, Preparation and structural study of a novel nonlinear molecularmaterial: the L-histidinum dihydrogenarsenate orthoarsenic acid crystal. J. Mol. Struct. 526 (2000) 269-278.

[35] H. Ratajczak, S. Debrus, M. May, J. Barycki, J. Baran, Hydrogen-bonded organic solids with nonlinear optical properties. Bull. Pol. Acad. Sci. Chem. 48 (2000) 189-192.

[36] H. Ratajczak, J. Baran, J. Barycki, S. Debrus, M. May, A. Pietraszko, H.M. Ratajczak, A. Tramer, J. Venturini, New hydrogen-bonded molecular crystals with nonlinear second-order optical properties. J. Mol. Struct. 555 (2000) 149-158.

[37] S. Debrus, H. Ratajczak, J. Venturini, N. Pinçon, J. Baran, J. Barycki, T. Glowiak, A. Pietraszko, Novel nonlinear optical crystals of noncentrosymmetric structure based on hydrogen bonds interactions between organic and inorganic molecules. Synth. Met. 127 (2002) 99-104.

[38] H. Ratajczak, S. Debrus, R. Jakubas, J. Baran, Second harmonic generation properties of [CH3 NH3] 5 Bi2 Br11 ferroelectric crystal. Bull. Pol. Acad. Sci. Chem. 48 (2000) 193-194.

[39] J. Janczak, G.J. Perpétuo, Bis (melaminium) sulfate dihydrate. Acta Cryst. C. 57 (2001) 1431-1433

[40] J. Janczak, G.J. Perpétuo, Bis (melaminium) DL-malate tetrahydrate. Acta Cryst. C. 59 (2003) o349–o352.

[41] M. K. Marchewka, J. Janczak, S. Debrus, J. Baran, H. Ratajczak, Crystal structure, vibrational spectra and nonlinear optical properties of tetrakis (2, 4, 6-triamino-1, 3, 5-triazin-1-ium) bis (selenate) trihydrate crystal, Solid State Sci. 5 (2003) 643-652.

[42] S. Debrus, M. K. Marchewka, M. Drozd, H. Ratajczak, Vibrational, calorimetric and nonlinear optical studies of melaminium-bis (trichloroacetate) monohydrate molecular–ionic crystal, Opt. Mater. 29 (2007) 1058-1062.

[43] S. Kalyanaraman, S. Vijayalakshmi, M. Kanagavalli, M. Kalaselvi, S. Maheswari, P. Kirthika, Optical properties of melamine-based materials, Optik. 125 (2014) 6634-6636.

[44] N. Kanagathara, N.G. Renganathan, M.K. Marchewka, N. Sivakumar, K. Gayathri, P. Krishnan, S. Gunasekaran, G. Anbalagan, Growth and characterization of Melaminium bis (trichloroacetate) dihydrate, Spectrochim. Acta. A. Mol. Biomol. Spectrosc.101 (2013) 112-118.

[45] A. Pekparlak, D. Avcı, Y. Atalay, K. Esmer, Theoretical studies of molecular structure and vibrational spectra of melaminium salt: 2, 4, 6-Triamino-1, 3, 5-triazin-1, 3-ium Tartrate Monohydrate. Arab. J. Sci. Eng. 37 (2012) 171-181

[46] E. D., Weil, S. V. Levchik, Commercial flame retardancy of unsaturated polyester and vinyl resins. J. Fire Sci. 22(4) (2004) 293-303.

[47] G.M. Crews, W. Ripperger, D.B. Kersebohm, J. Seeholzer Melamine and guanamines. Ullmann Encycl Ind Chem. 16 (1990) 171-185.

[48] A. Casu, G. Camino, M. De Giorgi, D. Flath, V. Morone, R. Zenoni, Fire-retardant mechanistic aspects of melamine cyanurate in polyamide copolymer Polym. Degrad. Stab. 58 (3) (1997) 297-302.

[49] J. Zieba-Palus, Application of micro-Fourier transform infrared spectroscopy to the examination of paint samples, J. Mol. Struct. 511 (1999) 327-335.

[50] A.I. Belabanovich, S.V. Levchik, G.F. Levchik, J. Engelmann, Fire retardant synergism between cyclic diphosphonate ester and melamine in poly (butylene terephthalate), J. Fire Sci. 20 (1) (2002) 71-83.

[51] K. Slimer, P. Cristjanson, T.Kaljuvee , T. Pekh, I. Lasn , I. Saks, TG-DTA study of melamine-urea-formaldehyde resins, J. Therm. Anal. Calorim. 92 (2008) 19-27.

[52] Kuryla, W. C. Papa, A. J. Flame Retardancy of Polymeric Materials; Dekker: New York. 3 (1973) 1-5.

[53] K. Sha, Y. L. Hu, Y. H. Wang, R. Xiao, Preparation of flame-retardant polyamide 6/melamine cyanurate via in situ polymerisation and its characterization. Mater. Res. Innov. 18 (2014) 843-847.

[54] G. Bertelli, P. Busi, L. Costa, G. Camino, R. Locatelli, Fire retardant systems based on melamine hydrobromide: Part 2- Overall thermal degradation, Polym. Degrad. Stab. 18 (4) (1987) 307-319.

[55] V. Sangeetha, M. Govindarajan, N. Kanagathara, M. K. Marchewka, S. Gunasekaran, G. Anbalagan, Vibrational, DFT, thermal and dielectric studies on 3-nitrophenol-1, 3, 5-triazine-2, 4, 6-triamine (2/1). Spectrochim. Acta - A: Mol. Biomol. Spectrosc. 118 (2014) 1025-1037.

[56] Y. Liu, Q. Wang, G. Fei, Y. Chen, Preparation of polyamide resin-encapsulated melamine cyanurate/melamine phosphate composite flame retardants and the fire-resistance to glass fiber-reinforced polyamide 6. J. Appl. Polym. Sci. 102 (2) (2006) 1773-1779.

[57] L. Costa, G. Camino, Thermal behaviour of melamine. J. Therm. Anal. 34 (2) (1988) 423–429.

[58] X. G. Li, Thermogravimetric kinetics of thermotropic copolyesters containing p-oxybenzoate unit by multiple heating-rate methods. J. Appl. Polym. Sci. 74 (8) (1999) 2016-2028.

[59] D. L. Yu, J. L. He, Z. Y. Liuetal, Phase transformation of melamine at high pressure and temperature. J. Mater. Sci. 43 (2008) 689-695.

[60] N. Kanagathara, M.K. Marchewka, N. Sivakumar. A study of thermal and dielectric behavior of melaminium perchlorate monohydrate single crystals. J. Therm. Anal. and Cal. 112 (2013) 1317-1323.

[61] S. K. Manu, R. Manivannan, A review on the role of eco-friendly inhibitors for mitigation of microbial influenced corrosion of steel and its impacts. IOP Conf. Ser. Mater. Sci. Eng. .1057(1) (2021) 12002.

[62] H. M. Yang, Role of organic and eco-friendly inhibitors on the corrosion mitigation of steel in acidic environments-A state-of-art review. Mol. 26(11) (2021) 3473.

[63] C. L. Jones, Principles and Prevention of Corrosion, Second Edition, Prentice Hall, Upper Saddle River, NJ, 119, (1996).

[64] M. P. Schultz, OCE-4518 Protection of Marine Materials Class Notes. Florida Institute of Technology, (1997).

[65] G. W. Swain, OCE-4518 Protection of Marine Materials Class Notes. Florida Institute of Technology, (1996).

[66] T. Dawson, EN380 Engineering Aspects of Materials Class Notes. United States Naval Academy, (1993).

[67] W. Plieth, Electrochemistry for materials science. First Edition, Elsevier, (2008).

[68] G. Beranger, H. Mazille, Corrosion et anticorrosion (pratique industrielle), Mécanique et ingénierie des matériaux, Lavoisier, Paris, Hermés Science Publication, (2002).

[69] NACE, Glossary of corrosion Terms, Materials Protection, (1965).

[70] M. H. Hussin, M. J. Kassim, The corrosion inhibition and adsorption behavior of Uncaria gambir extract on mild steel in 1 M HCl. Mater. Chem. Phys, 125 (2011) 46.

[71] S Garai, S Garai, P Jaisankar, JK Singh, A Elango, A comprehensive study on crude methanolic extract of Artemisia pallens (Asteraceae) and its active component as effective corrosion inhibitors of mild steel inacid solution. Corros. Sci. 60 (2012) 193-204

[72] D. Ben Hmamou, Corrosion inhibition of steel in 1 m hydrochloric acid medium by chamomile essential oils. Int. J. Electrochem. Sci, 7(3) (2012) 2361-2373

[73] E.Oguzie. Inhibition of acid corrosion of mild steel by biomass extract from the petersianthus macrocarpus plant. J. Mater. Environ. Sci, 4(2) (2013) 217-226.

[74] A. M. Abdel-Gaber, B. A. Abd-El-Nabey, I. M. Sidahmed, A. M. El-Zayady, M. Saadawy, Inhibitive action of some plant extracts on the corrosion of steel in acidic media, Corros. Sci. 48(9) (2006) 2765-2779.

[75] P. Raja, M. Sethuraman, Natural product as corrosion inhibtor for metals in media. Mater. Lett. 62 (2008) 113-116.

[76] D. Landolt, Corrosion et Chimie de Surface des Métaux, 1st Edition, Alden Press, Oxford,(1993).

[77] F. Constantin, Étude de l'efficacité d'inhibiteurs de corrosion utilisés dans les liquides de refroidissement, Thèse de doctorat, université de Piteşti-Roumanie, (2011).

[78] I.L. Rozenfeld, Corrosion Inhibitors, McGraw-Hill, (1981).

[79] C.C. Nathan, Corrosion Inhibitors, NACE, Houston, (1973).

[80] F. Bentiss, Partie, A. Lutte contre la corrosion par l'utilisation d'inhibiteurs. HDR de Fouad Bentiss, Lille 1, 2006

[81] S.M. Kuzmin, S.A. Chulovskaya, V.I. Parfenyuk, Mechanism and superoxide scavenging activity of hydroxy substituted tetraphenylporphyrins via coulometric approach. J. Electroanal. Chem. 772 (2016) 80-88.

[82] R. Ahmed, S. Zhang, Alchemilla vulgaris extract as green inhibitor of copper corrosion in hydrochloric acid. Int. J. Electrochem. Sci. 14(11) (2019) 10657-10669.

[83] A. Abd almajeed Madi abdallah, Synthèse, Caractérisation de nouveaux ligands bases de Schiff en vued'application dans la protection contre la corrosion et en biologie, Doctoral thesis, University of Ferhat Abbas University - Setif1.

[84] B. A. Abd-El-Nabey, A. M. Abdel-Gaber, M. E. S. Ali, E. Khamis, S. El-Housseiny, Inhibitive Action of Cannabis Plant Extract on the Corrosion of Copper in 0.5 M H_2SO_4. Int. J. Electrochem. Sci. 8(5) (2013) 7124-7137.

[85] K. Tebbji, A. Aouniti, M. Benkaddour, H. Oudda, I. Bouabdallah, B. Hammouti, A. Ramdani, New bipyrazolic derivatives as corrosion inhibitors of steel in 1 M HCl. Progress in organic coatings, 54(3) (2005) 170-174.

[86] O.K. Abiola, Y. Tobun, Cocos nuciferal. water as green corrosion inhibitor for acid corrosion of aluminium in HCl solution, Chin. Chem. Lett, 21(12) (2010) 1449-1452.

[87] S.A. Umoren, I.B. Obot, E.E. Ebenso, N.O. Obi-Egbedi, The Inhibition of aluminium corrosion in hydrochloric acid solution by exudate gum from Raphia hooker. Desalination, 247 (1-3) (2009) 561-572.

[88] G. O. Avwiri, F.O. Igho. Inhibitive action of Vernonia amygdalina on the corrosion of aluminium alloys in acidic media, Mater. Lett, 57(22-23) (2003) 3705-3711.

[89] N. Manwani, M. Batra, S. K. Arora, R. K. Upadhyay, A study of corrosion inhibition efficacy of leaves extract of solanum xanthocarpum and salvodera persica on aluminium and mild steel in HCl. (2023).

[90] A.J. Revathi Mohan, Corrosion protection of mild steel in hydrochloric acid up to 313 K using propyl benzimidazole: electroanalytical, adsorption and quantum chemical studies Egypt. J. Pet. 27 (1) (2016).

Chapter II: Methods and Experimental Techniques

In this chapter, we describe the various experimental physico-chemical methods such as UV-Visible (UV-Vis), infrared spectroscopy (IR), single-crystal X-ray diffraction (SXRD), Hirshfeld surface analysis and electrochemical methods such as cyclic voltammetry, potentiodynamic polarization (TAFEL) and electrochemical impedance spectroscopy (EIS) used to study corrosion inhibitors. and the experimental procedure, as well as a reminder of certain definitions and concepts that are necessary for our work and that will enable us to master the phenomena involved and interpret the results obtained.

II.1. Study Methods

II.1.1 DRX

X-rays are short-wavelength electromagnetic radiation produced by electron transitions involving electrons in the surrounding of the nucleus of the atom. When the rays hit the first layer of atoms on the surface of a crystalline solid at an angle, a certain amount of the rays is scattered.

II.1.2. Hirshfeld surface analysis

Its main purpose is to visualize and investigate molecular crystal structures, particularly through the decorated Hirshfeld surface and its corresponding two-dimensional fingerprint, as well as to visualize void spaces in the crystal through isosurfaces of the promolecule electron density. Crystal Explorer is a native cross-platform program that works with Windows, MacOS, and Linux. The program has undergone substantial modifications and improvements over the last ten years, including the ability to compute and visualize quantitative intermolecular interactions with accuracy and speed, and perhaps most importantly the ability to interface with the Gaussian and NWChem programs to compute the quantum-mechanical properties of molecules [1].

II.1.3. Spectroscopic analysis

II.1.3.1. Infrared (IR) absorption spectroscopy

Infrared spectroscopy is one of the most widely used tools for characterizing and identifying organic molecules based on their vibrational properties. It is based on the absorption of very low-energy photons that modify the fundamental vibrational energy of molecules. It is a rapid and sensitive functional characterization method. The electromagnetic infrared spectrum

is divided into three regions: near (14000 - 4000 cm^{-1}), medium (4000 - 400 cm^{-1}) and far (<400 cm^{-1}).

The infrared spectrum represents a range of electromagnetic radiation between visible light and microwaves. In the context of structural determinations, is primarily focused on the central region of this spectrum, which generally extends from 2.5 μm to16 μm. The characteristics of infrared radiation are often expressed in terms of frequency, defined by the wavenumber (ν) in inverse relation to the wavelength (λ): $\nu = 1/\lambda$, this frequency range generally covers values between 4000 and 400 cm^{-1}

The bands observed are mainly associated with two distinct modes of vibration:

- ✓ Elongation vibration (valence wave): oscillation of two bonded atoms along the axis of their bond, producing a periodic variation in their distance.
- ✓ Deformation vibration: oscillation of two atoms bonded to a third, producing a periodic variation in the angle of two bonds.

An IR spectrum is roughly divided into two parts:

- ✓ This region, between 4000 and 1500 cm^{-1}, represents the range of valence vibrations characteristic of the main functions.
- ✓ The region between 1500 and 400 cm^{-1} known as the fingerprint zone, which is most often used to compare the spectra of products with controls [2].

II.1.3.2. UV-Vis spectroscopy

UV-Vis spectroscopy is a straightforward, affordable, and adaptable method for determining a sample's absorption or transmission of ultraviolet and visible light. It is based on the properties of molecules to absorb light radiation of a certain wavelength. UV-Visible spectroscopy allows to access information qualitatively as to the nature of the bonds present within the sample but also to determine quantitatively the concentration of absorbing species in this spectral range. Ultraviolet-visible spectroscopy is a spectroscopic technique involving photons with wavelengths in the range of ultraviolet (100 nm - 400 nm), visible (400 nm - 750 nm) or near infrared (750 nm - 1 400 nm).

II.1.3.3. Thermal analysis

Thermal analyses are methods to monitor the thermal exchange between a sample and the external environment as a function of temperature. Heat treatment can be isothermal or dynamic with a programmed temperature rise rate. This analysis allows to study the chemical, physical or physicochemical phenomena, which are translated under the effect of temperature and in controlled atmosphere by a variation of mass. ATG quantifies the loss of material components and monitors their thermal stability. ATD measures the temperature difference between a sample and a reference when both are heated under the same atmosphere

II.1.4. Atomic force microscope (AFM)

Atomic force microscopy (AFM) is a method for analysing the surface topography and calculating the deposition roughness of a sample. This technique involves scanning the surface of the sample using a tip mounted on a lever, which is moved by a piezoelectric tube. The interactions (attractions or repulsions) between the atoms at the tip and those on the sample surface are used for this analysis. A laser beam is directed at the end of the lever and its reflection is detected by a photodiode, enabling the deformation of the lever to be measured. The vertical position of the sample is adjusted to maintain a constant force during the measurement. Using this method, it is possible to determine the topography of the sample [3-5].

II.1.5. Electrochemical methods used

II.1.5.1. Cyclic Voltammetry (VC)

Cyclic voltammetry (VC) is a highly effective electrochemical method for the characterization of charge transfer reactions and allows to characterize species and the degree of reversibility of the electrochemical process. The general principle of voltammetry is therefore to obtain a response (current) from the system under study to the excitation (potential) which is responsible for the desired electrochemical reaction. This is done by performing an exploration by imposition and progressive variation of the electrode potential (potential scanning). The main advantages of cyclic voltammetry include:

- The speed of measurements.

- The possibility of stopping a reaction sequence by playing on the potential scanning domain.

- The study of re-oxidation of products formed at electrodes.

- Analysis of solutions and determination of the concentration of species present.

- The possibility of studying adverse reactions [6].

In the case of linear voltammetry, the evolution of voltage is expressed.

$$E(t) = E_0 + v\,t \qquad \text{II.1}$$

The plus sign in the previous equation corresponds to a sweep towards positive voltages, the minus sign corresponds to a sweep towards negative voltages.

where:

E: Potential of the indicator electrode (volt).

Ei: Initial potential applied to the electrode.

v: Scan speed, v = dE/dt (V/s).

t: Time (s).

E_0: is the initial value of the electrode voltage.

v: is the scanning speed in voltage. Figure II.1 represents the evolution of the electrode potential following a potential that has changed linearly over time.

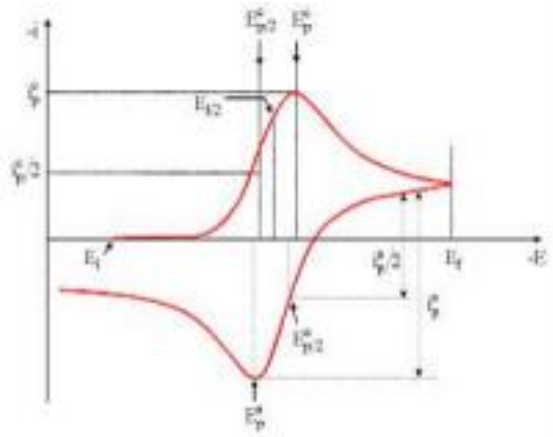

Figure II.1. The general shape of the voltammetry curve.

The potential is measured between the reference electrode and the working electrode, and the current is measured between the working electrode and the counter-electrode. These data are then plotted in the form of intensity versus potential. As the potential shape shows, the

subsequent sweep produces a current peak for all species that can be oxidized or reduced in the sweep potential interval.

Reversible system: In a fast electron transfer kinetics, the maximum current for a reversible torque at 25°C is given by the Randles-Sevcik equation:

$$I_p = \pm(2.69*10^5)n^{3/2}AD^{1/2}Cv^{1/2} \qquad \text{II.2}$$

The potential difference between anode and cathode peaks is:

$$\Delta E = E_{pc} - E_{pa} = 0.059/n \qquad \text{II.3}$$

Peak potentials do not change with the scan speed. The ratio of peak currents is equal to one (I_{pa}/I_{pc} =1).

Quasi-reversible system: The peak current is given by the equation:

$$I_p = (2.99*10^5)n^{3/2}AD^{1/2}K_sCv^{1/2} \qquad \text{II.4}$$

The potential difference between anode and cathode peaks is $\Delta E > 0.059/n$,

Irreversible system: When the electron transfer kinetics is slow (irreversible) the current expression becomes:

$$I_p = (2.99*10^5)n(\alpha n_a)^{1/2}AD^{1/2}Cv^{1/2} \qquad \text{II.5}$$

Where:

Ip: Peak current intensity (A)

n: Number of electrons transferred

A: Electrode surface (cm^2)

C: Concentration ($mol.cm^{-3}$)

v: Scan speed (V/s)

D : Diffusion coefficient (cm^2/s)

Studying the variations of current and peak potential as a function of the scanning speed ($I_p = f(v^{1/2})$ and $E_p = f(\text{Log}(v))$ can inform us about the nature of the limiting step and the kinetics of the electrochemical reaction at the electrode.

* If $I_p = f(v^{1/2})$ is a straight line, the reaction is governed by diffusion only.

* If $I_p = f(v^{1/2})$ is a concavity curve oriented towards the current axis, the electrode process involves a charge transfer with adsorption. In the case where the concavity is turned towards the axis of the scan speeds, the electrode process is associated with a chemical reaction.

* If $E_p = f(\text{Log}(v))$ is a straight line: - Zero slope, the electrode reaction is fast. - With a slope of not zero and equal to 30/nF (mV), this is a slow load transfer.

* If $E_p = f(\text{Log}(v))$ is a curve and $I_p = f(v^{1/2})$ is a straight line, this is a semi-fast process.

II.1.5.2. Polarisation curves

Polarisation curves, known as Tafel lines, illustrate the metal-solution interface and are a fundamental characteristic of electrochemical kinetics. However, they only reflect the slowest stage of the overall process (such as the transport of matter or the adsorption of species onto the electrode) at the electrochemical interface. The plot of the polarization curves (Figure II.2) allows to determine precisely the electrochemical parameters of a metal in contact with an electrolyte, such as corrosion current density (i_{corr}), anode plate slopes (β_a) and cathodic (β_c), corrosion potential (E_{corr}) and corrosion rate (v_{corr}) [7].

A potentiodynamic curve is made up of two branches:

- an anode branch corresponding to the superposition of currents resulting from oxidation reactions: $M \rightarrow M^{n+} + ne^-$ corrosion of the metal, for example.

- a cathode branch corresponding to the superposition of the currents resulting from the reduction reactions.

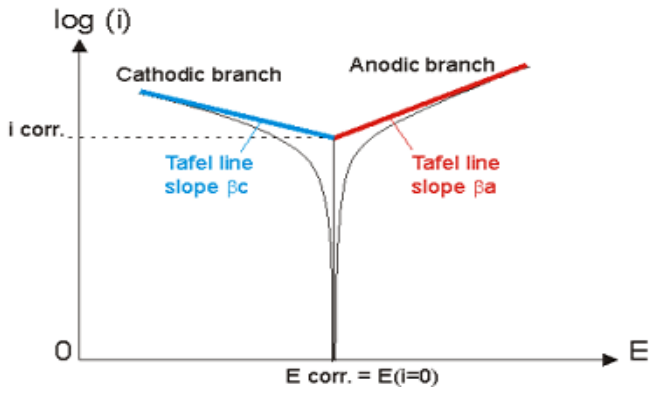

Figure II.2. Schematic representation of a current-potential curve (Tafel lines).

II.1.5.3. Electrochemical impedance spectroscopy (EIS)

EIS is the most widely used electrochemical technique for studying corrosion processes and corrosion protection (inhibitors or coatings). It is a non-destructive method that enables the evolution of a system to be followed over time. It can be used to identify the mechanisms taking place at the metal/solution interface and to propose kinetic models [8].

This method consists of superimposing a low-amplitude sinusoidal potential modulation on the electrode potential and monitoring the current response for different frequencies of the disturbance signal. Frequency analysis of the electrochemical impedance will enable the various elementary phenomena to be differentiated according to their characteristic frequency (or time constant). The electrochemical phenomena of charge transfer occur in the high-frequency range, while the phenomena of diffusion, and adsorption.... occur at low frequencies [9]. Impedance is derived from two types of plots, the Nyquist diagram and the Bode diagram (**Figure II.3**).

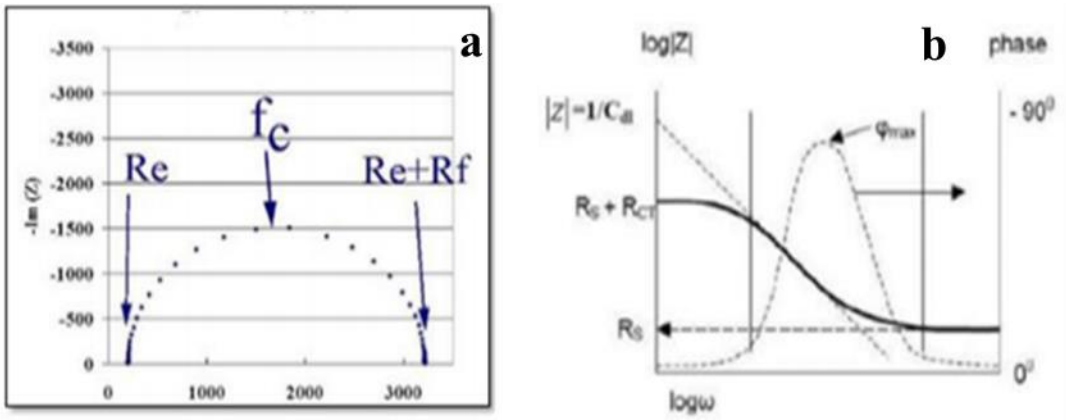

Figure II.3. a. Impedance diagram in the Nyquist plane. b. Bode diagram

This diagram shows the imaginary part of the impedance as a function of the real part. It allows the solution resistance to be determined directly by reading the real part of the impedance at high frequency, as well as the charge transfer resistance by reading the real part of the impedance at low frequency. The capacitance C is calculated using the frequency at the top of the loop [10].

The Bode representation consists of two graphs plotting the logarithm of the modulus $|Z|$ and the phase φ of the impedance versus the logarithm of the frequency [11].

II.2. Equipment used and operating conditions

II.2.1. Single crystal X-ray diffraction

The single-crystal X-ray diffraction (SXRD) was performed at 150 K, using Bruker D8 Venture photon diffractometer, equipped with a Mo(Kα) anticathode and a graphite monochromator (λ=0.71073 Å). The refinement was performed by the full-matrix least square method using SHELXL-2017 (Sheldrick, 2017) programs [12]. All observed reflections and data reduction were used for the unit cell refinement, by the mean of CrysAlisRed program [13]. At the end, the structures were plotted by using Mercury software [14]. The X-ray crystallographic data for the structure reported in this paper have been deposited at "Cambridge Crystallographic Data Centre" (CCDC) with the reference number 2236655 for Hybrid 1 and 2236678 for hybrid compound 2.

II.2.2. Hirshfeld surface analysis

The Hirshfeld Surface analysis was performed to determine the intermolecular interactions in the crystal lattice of Tris(melaminium) monodrogenphosphate dihydrogenphosphate tetrahydrate and 2,4,6-triamino-1,3,5-triazinium perchlorate monohydrate. The Crystal Explorer program has been used to obtain the fingerprint plots. The fingerprint plots are identified based on the d_e and d_i distances from the HS to the nearest nucleus outside and inside the surface, respectively.

II.2.3. Infrared (IR) absorption spectroscopy

The infrared spectra of the mattes were recorded in a frequency range from 500 to 4000 cm^{-1}. The analyses were carried out in solid phase using a spectrophotometer equipped with a module made of a crystal in Germanium (IR Spirit).

II.2.4. UV-Vis spectroscopy

The UV-visible absorption electronic spectrum was recorded in distilled water between 200 and 800 nm using a UV-1900i UV–Vis. Spectrophotometer, using quartz cells of 1 cm path length. The solvent used is water

II.2.5. Thermal analysis

The thermal behavior of the materials was investigated from the room temperature to 825 °C, utilizing a simultaneous thermo-gravimetric analysis and differential thermal analysis (TGA–DTG), and differential scanning calorimetry (DSC) techniques, using a Perkin Elmer TGA 4000 apparatus, under nitrogen atmosphere, with a heating step of 20 °C/min.

II.2.6. Electrochemical measurement

The electrochemical studies use a set-up consisting of a thermostated electrochemical cell with three electrodes, connected to a Potentiostat / Galvanostat, controlled by a computer (voltamaster 4 software).

The cell is made of PYREX glass, with a capacity of 25 ml, a sufficient volume to ensure that the concentration of electroactive species remains constant during the manipulation. The cell has a double wall and a 4-hole lid to accommodate the three electrodes and the degassing tube.

electrodes

- ✓ Working electrode**:** Platinum electrode with an area of 3 mm^2, and round X48 carbon steel electrode in the form of a cylindrical rod
- ✓ The auxiliary electrode (counter electrode): we used a platinum wire as the counter electrode.
- ✓ Reference electrode: all potential measurements are taken against a saturated potassium chloride (Ag/AgCl) and calomel electrode (ECS).

II.3. Products and solvents used

The reagents and solvents used in this study are commercial and were used without prior treatment:

-2, 4,6-triamino-1, 3,5-triazine (Melamine).

- Phosphoric acid (H_3PO_4).

- Perchloric acid ($HClO_4$).

- Lithium perchlorate ($LiClO_4$).

- Ethanol / Methanol.

- Dimethysulfoxide (DMSO).

- Nitrogen.

- Distilled water.

-Acetone.

-The carbon steel XC48, which was cut into a cylindrical shape with dimensions that differed from the exterior surface S, had the following chemical composition: Fe (98.098%), C (0.418%), F (0.777%), Mn (0.730%), Si (0.245%), Ni (0.079%), S (0.019%), P (0.016%), and Mo (0.012%). Following that, three cleaning procedures were carried out: washing with distilled water, rinsing with acetone, and abrading with Emery paper 600, 800, 1200, 1500, and 2400.

Synthesis montage

The experimental set-up includes:

- A balloon heater with magnetic stirring.

- A coolant that condenses the solvent during the reaction.

- A ball with a magnetic bar.

References

[1] P. R. Spackman, M. J. Turner, J. J. McKinnon, S. K. Wolff, D. J. Grimwood, D. Jayatilaka, M. A. Spackman, CrystalExplorer: a program for Hirshfeld surface analysis, visualization and quantitative analysis of molecular crystals. J. Appl. Crystallogr. *54*(3) (2021) 1006-1011.

[2] J. Mendham. Analyse Chimique quantitative de Vogel. (2005).

[3] A. Gaudon, Thèse Doctorat, Limoges : Université de Limoges, (2005).

[4] G. Binnig, H. Rohrer, Microscope à effet tunnel. IBM J. Res. Dev.30(4) (1986) 355-369.

[5] G. Binning, C. Quate, C. Gerber, Atomic Force Microscope. Phys. Rev.Lett. 56 (1986) 930-933.

[6] P. M. Monk, R. J. Mortimer, D. R. Rosseinsky, Electrochromism: fundamentals and applications. John Wiley & Sons. (2008).

[7] A. Abd almajeed Madi abdallah, Synthèse, Caractérisation de nouveaux ligands bases de Schiff en vued'application dans la protection contre la corrosion et en biologie, Doctoral thesis, University of Ferhat Abbas University - Setif1. (2021).

[8] M. Duprat, A. Bonnel, F. Dabosi, J. Durand, L. Cot, Les monofluorophosphates de zinc et de potassium en tant qúinhibiteurs de la corrosion d'un acier au carbone en solution de NaCl a 3%. J. Appl. Electrochem. 13 (1983) 317-323.

[9] H. S. Magar, R. Y. Hassan, A. Mulchandani, Electrochemical impedance spectroscopy (EIS): Principles, construction, and biosensing applications. Sensors, 21(19) (2021) 6578.

[10] A. C. Lazanas, M. I. Prodromidis, Electrochemical impedance spectroscopy a tutorial. ACS Publications.3(3) (2023) 162-193.

[11] O. Lavigne; Caractérisation des films passifs pour la définition de nouveaux matériaux:

Application aux plaques bipolaires métalliques des systèmes PEMFCs, thèse doctorat, Institut

National des Sciences Appliquées de Lyon, (2009).

[12] A. V. Nemtareva, V. F. Mironova, R. R. Fayzullina, I. A. Litvinova, R. Z. Musina, Reactions of Arylenedioxytrihalophosphoranes with Acetylenes: XV.1 Reaction of 2, 2, 2-Tribromo-

4, 6-di-tert-butylbenzo-1, 3, 2 λ5-dioxaphospholedioxaphosphole with Pent-1-yne, Russ. J. Gen. Chem. 88 (2018) 2290–2295.

[13] Oxford Diffraction CrysAlisCCD and CrysAlisRED. Versions 170.10. Oxford Diffraction Poland Sp., Wrocław, Poland. (2003).

[14] C. F. Macrae, I. J. Bruno, J. A. Chisholm, P. R. Edgington, P. McCabe, E. Pidcock, L. Rodriguez-Monge, R. Taylor, J. van de Streek, P. A. Wood, Mercury CSD 2.0-new features for the visualization and investigation of crystal structures. J. Appl. Crystallogr. 41 (2008) 466-470.

CHAPTER III
Synthesis, structural characterization and thermal stability of Hyb 1

This chapter will be devoted to the description of the synthesis of a new hybrid ionic material named tris(melaminium) monodrogenphosphate dihydrogenphosphate tetrahydrate ($3C_3H_7N_6^+.HPO_4^{2-}.H_2PO_4^-.4H_2O$) ((Hyb 1) as single crystal, its detailed structural study by single crystal X-ray diffraction and its Hirshfeld Surface. As well as, its characterization by UV-Vis and FT-IR spectroscopic analysis and its thermal decomposition behavior studied by TGA/DTG.

III.1. Synthesis and crystallization

The starting compounds, melamine (Sigma Aldrich, 99%) and phosphoric acid (Sigma Aldrich, 85%) were used as supplied. The dissolved acid was added dropwise to the melamine in hot distilled water with the help of a dropper. Then the reaction mixture was brought to reflux under magnetic stirring. After 6 hours, the mixture evaporated slowly at room temperature. The solid compound formed was filtered and washed with ethanol several times to obtain highly purified material a reaction for the synthesis of $3C_3H_7N_6^+.HPO_4^{2-}.H_2PO_4^-.4H_2O$ is shown in Scheme III.1.

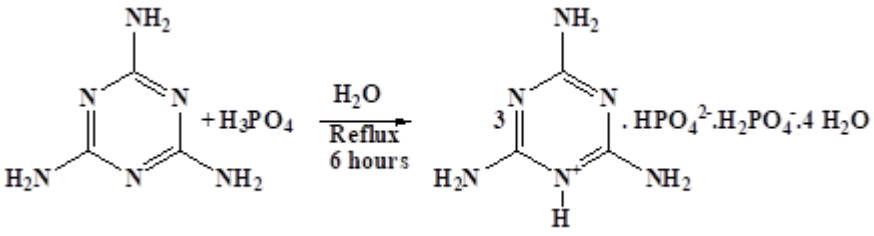

Scheme III. 1 Reaction scheme for the synthesis of $3C_3H_7N_6^+.HPO_4^{2-}.H_2PO_4^-.4H_2O$.

III.2. Structural Characterization

III.2.1. Single crystal study

Figure III.1 (a) shows the asymmetric unit of title material, it is made up by three singly protonated melamine ($3M^+$) cations at the N atom of the s-triazine ring, one simple and one double negatively charged phosphoric acid anions $2HPO_4^{1-}$ and $2HPO_4^{2-}$ respectively, and four water molecules, giving the chemical formula $3C_3H_7N_6^+.HPO_4^{2-}.H_2PO_4^-.4H_2O$. In addition, the Figure III.1 (b) shows the internal angle measurements and bond lengths characteristic of melaminium, illustrating that are skewed from the ideal form, as reported R. Bourzami and al [1]. and according to the valence-shell

electron pair repulsion theory (VSEPR), this distortion can be well explained by the lone pair electron steric effect [2].

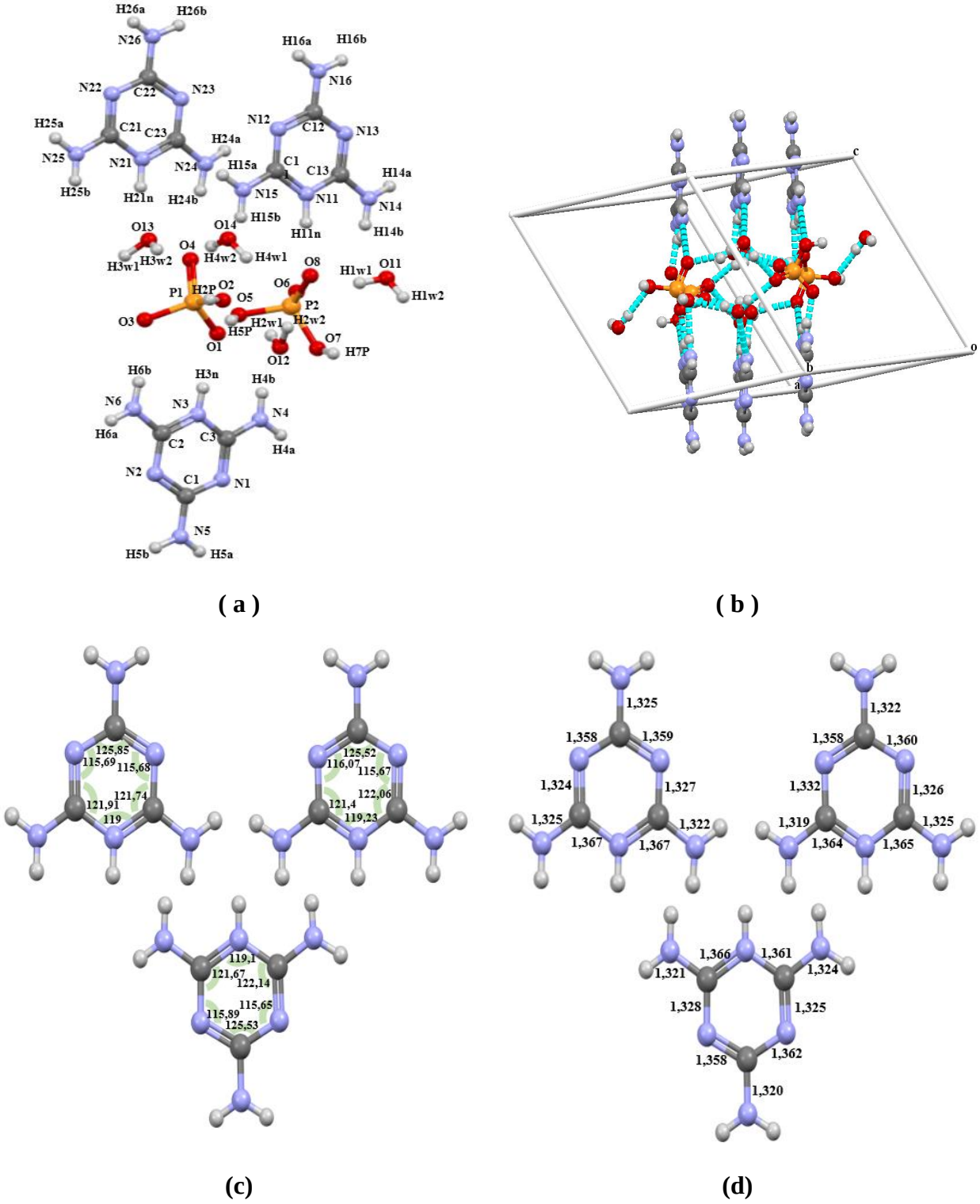

Figure III.1. (a) Asymmetric unit provided by atomic labelling, (b) unit cell provided by hydrogen bonding system, (c) internal angles of s-triazing of the asymmetric unit (d) bond lengths of s-triazing of the asymmetric unit.

Furthermore, two asymmetric units (Z = 2) form the triclinic unit cell (Figure III.1 (c)), that has P_1^- space group and the cell parameters a = 11.242(9), b = 11.846(9), c = 11.983(9) Å and α = 66.929(3), β = 115.341(2) and γ = 64.303(3) °, the experimental crystal data and structure refinement parameters are listed in Table III.1. The unit cell is non-centrosymmetric, but characterized by identity symmetry and an inversion center at the origin (000). In addition, the SXRD reveals that crystalline structure is maintained by weak bonds mainly hydrogen ones, giving a type one hybrid material; considering 3 Å as max donor-acceptor distance, 13 extramolecular hydrogen bonds per asymmetric unit of the type N-H···N, N-H···O, N^+-H···O and O-H···O were predicted. The N-H···N type joins the melaminium molecules, N-H···O and N^+-H···O types connect the organic and the inorganic parts, while the O-H···O type connects the molecules of phosphoric acid and water, which are either inorganic part. The Table III.2 lists one formal asymmetric unit's hydrogen bonds and their characteristics: bond lengths, angle measurements, and symmetry codes.

Table III.1. Crystal data and structure refinement parameters.

Empirical formula	$3C_3H_7N_6^+.HPO_4^{2-}.H_2PO_4^-.4H_2O$
Crystal system	Triclinic
Molecular weight (g/mol)	646.46
Space group	P_1^-
a (Å)	11.242 (9)
b (Å)	11.846 (9)
c (Å)	11.983 (9)
α (°)	66.929 (3)
β (°)	71.555 (3)
γ (°)	64.303 (3)
V ($Å^3$)	1302.24 (18)
Z	2
Crystal size (mm^3)	0.22 × 0.19 × 0.16
Crystal color/habit	Colourless/Prism
Dcalc (mg/m^3)	1.649
$\lambda_{MoK\alpha1}$ (Å)	0.71073
Temperature (K)	150

μ (mm^{-1})	0.26
F(000)	676
θ Range (°)	2.3→27.5
Δ ρ_{max} ($eÅ^{-3}$)	0.63
Δ ρ_{min} ($eÅ^{-3}$)	-0.45
h	-14→14
k	-15→ 15
l	- 15→15
Measured reflections	29641
Independent reflections	5909
reflections with I>2σ(I)	4410
No. of parameters	502
R_{int}	0.072
R [F^2>2σ(F2)]	0.040
wR(F^2)	0.099
S	1.04

Table III.2. Hydrogen-bond geometry and their symmetry codes.

D-H···A	D-H (Å)	H···A (Å)	D···A (Å)	D-H···A (°)
N3-H3N···O1	0.87 (3)	1.81 (3)	2.678 (2)	175 (2)
N5-H5A···O12^{i}	0.88 (3)	2.12 (3)	2.972 (2)	164 (2)
N5-H5B···O14^{ii}	0.89 (3)	2.04 (3)	2.908 (3)	166 (2)
N6-H6A···N23^{ii}	0.86 (3)	2.13 (3)	2.983 (3)	174 (2)
N6-H6B···O3	0.88 (3)	2.02 (3)	2.890 (2)	175 (2)
N11-H11N···O6	0.93 (3)	1.73 (3)	2.657 (2)	174 (3)
N14-H14A···N13^{iii}	0.90 (3)	2.07 (3)	2.959 (3)	174 (2)
N14-H14B···O11	0.85 (3)	2.36 (3)	3.008 (2)	133 (2)
N16-H16A···O4^{iv}	0.91 (2)	2.01 (3)	2.904 (2)	169 (2)
N16-H16B···O11^{iii}	0.86 (2)	2.25 (3)	3.090 (3)	163 (2)
N21-H21N···O13	0.91 (3)	1.72 (3)	2.616 (2)	169 (3)
N26-H26A···O7^{v}	0.86 (2)	2.04 (2)	2.878 (2)	164 (2)
N26-H26B···O2^{iv}	0.89 (3)	2.25 (3)	3.025 (2)	145 (2)

Symmetry codes: (i) −x, −y+1, −z+2; (ii) x, y−1, z+1; (iii) −x, −y+2, −z; (iv) −x+1, −y+1, −z; (v) x+1, y, z−1.

The Figure III.2 illustrates the 3D supramolecular network, it shows clearly the formation of melaminium planar supramolecular chains along (Oa) direction (Figure III.2 (a)), comparing to our previous similar compound [3], those supramolecular chains are laid parallel along a diagonal direction of the unit cell, but in non-stacked form as shown in the Figure III.2 (b), with a separation distance about 3.2 Å, at this distance no direct contact between the chain was observed, whereas, the chains are inter-connected indirectly by N-H···O, N^{+}-H···O hydrogen bonds via the water and phosphoric acid of the inorganic part (Figure III.2 (c)), forming finally hybrid lamellar material along the (Oc) direction (Figure III.2 (c)).

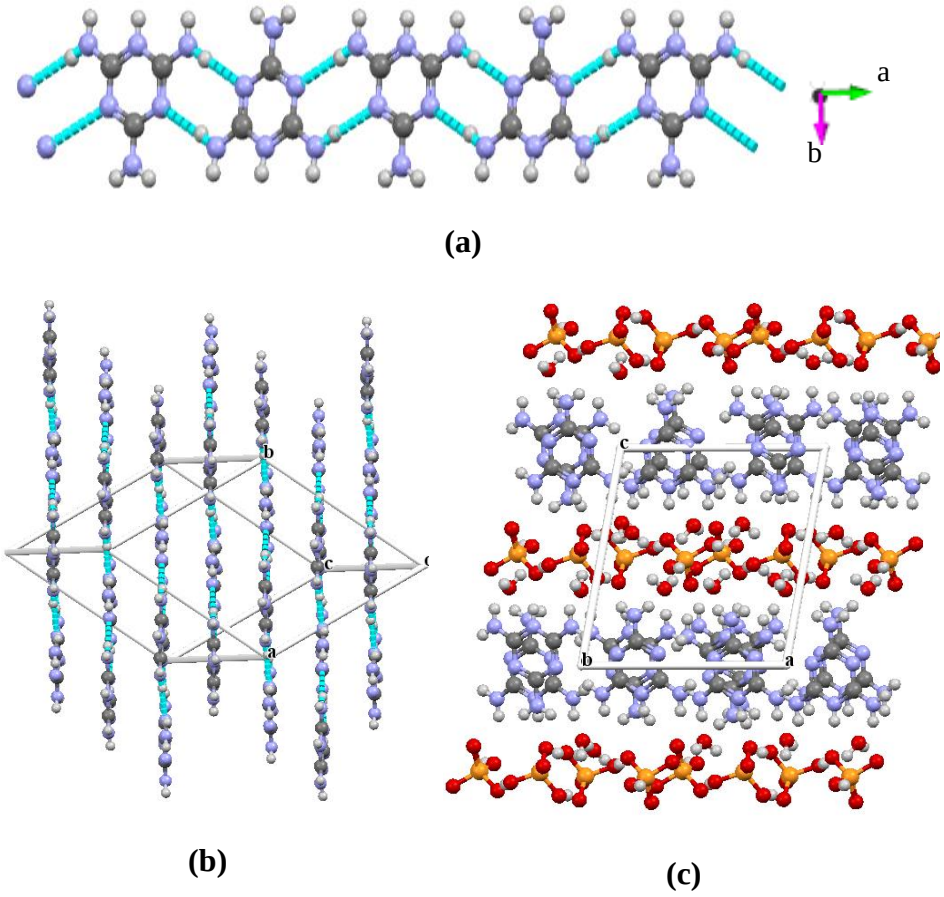

(a) **(b)** **(c)**

Figure III.2. 3D supramolecular network (a) melaminium chains laid along the direction 'oa' (b) diagonal view showing the non stacked parallel melaminium chains, (c) 3D supramolecular network.

III.2.2. Hirshfeld Surface (HS) analysis

The Hirshfeld surface (HS) analysis was performed using Crystal Explorer 21 to study the different intermolecular close contacts in the crystal structure [4,5]. The two-dimensional HS fingerprint plots allowed the identification of the close contacts, and estimated by the nearest nucleus external (d_e) as function of the nearest nucleus internal (d_i) distances to the HS surface [6]. In the crystal, the distances d_e and d_i mapped on the Hirshfeld surface provide a three-dimensional picture of intermolecular close contacts [7]. Considering the Van der Waals rays, the normalized contact distance d_{norm} is given by the following formula [8]:

$$d_{norm} = \frac{d_i - r_i^{\upsilon dW}}{r_i^{\upsilon dW}} + \frac{d_e - r_e^{\upsilon dW}}{r_e^{\upsilon dW}} \qquad \textbf{III.1}$$

Where: r_e^{vdW} and r_i^{vdW} are the van der Waals radius of the appropriate atom external and internal respectively [7]. The d_{norm} values is displayed using a red–white–blue color scheme, where red highlights shorter contacts, white is used for contacts around the vdW separation, and blue is for longer contacts. In addition, two additional colored representation (shape index and curvedness) based on the HS can be specified.

The Figure III.4 shows the surfaces mapped over d_{norm}, shape index and curvedness. The HS of the Tris(melaminium) monodrogenphosphate dihydrogenphosphate tetrahydrate were generated utilizing a standard (high) surface resolution with the 3D d_{norm} surfaces mapped over a fixed color scale of -1.487 Å (red) to +1.368 Å (blue), the shape index mapped in the color range of -0.997 Å to +0.999 Å and curvedness was in the range of -4.823 Å to +0.772 Å are simulated and plotted with Crystal Explorer software. Very close intermolecular interactions were identified by the 3D d_{norm} surface. The shape index is shown with 2D-fingerprint plots; it is sensitive to the very slight surface shape fluctuations. The curvedness is a function of the number of forms in the crystal.

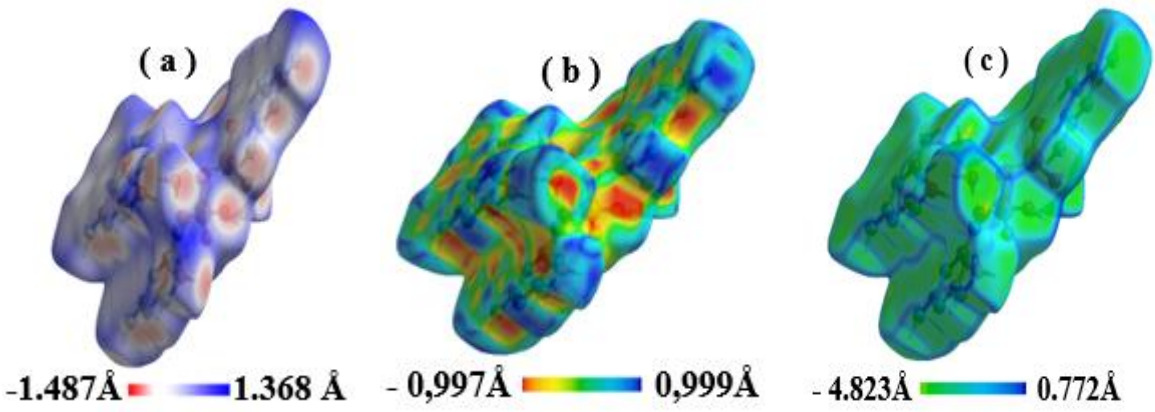

Figure III.3. Hirshfeld surfaces (a) d_{norm}, (b) shape index, (c) curvedness for Tris (melaminium) monodrogenphosphate dihydrogenphosphate tetrahydrate.

In addition, the HS calculations allowed the determination of some quantitative measures like Hirshfeld area (S_H = 641.11 Å^2), Hirshfeld volume (V_H = 550.35 Å^3), asphericity (Ω = 0.194) and globularity (G = 0.653) (Table III.3). The Globularity G is a measure of the degree to which the surface area differs from a sphere of the same volume and is equal to $(36\pi V_H^2)^{1/3}/S_H$, and it is inferior to 1, it will be 1 for an ideal sphere. The value of G indicate that the molecular surface is more structured, not a sphere [9]. The term asphericity is a measure of structural anisotropy [10,11], and is calculated by the following Formula:

$$\Omega = \frac{1}{2}\left\{\sum_{i\neq j}(\lambda_i - \lambda_j)^2\right\}\left\{\sum_{i\neq 1}^{n}\lambda_i\right\}^{-2} \qquad \textbf{III.2}$$

Where: λ_i are the three principal moments of inertia of the molecule.

Table III.3. Quantitative measures of HS.

Molecular volume V_H (Å^3)	Surface area S_H (Å^2)	Globularity (G)	Asphericity (Ω)
550.35	641,11	0.653	0.194

For the title crystal material, the HS analysis reveals that the major intermolecular contacts interactions are H···H, O···H, and N···H, and having a partial contribution in the total contact 39.8%, 26.1%, and 19.3% respectively. In addition, we noted that the HS analysis of the molecule showed also H···C/C···H, C···N/N···C, N···N/ N···N and C···C/C···C contacts of 3.8; 6.2; 3.5, and 1.1% respectively (Figure III.4 and Figure III.5). These results agree well with the XRD analysis.

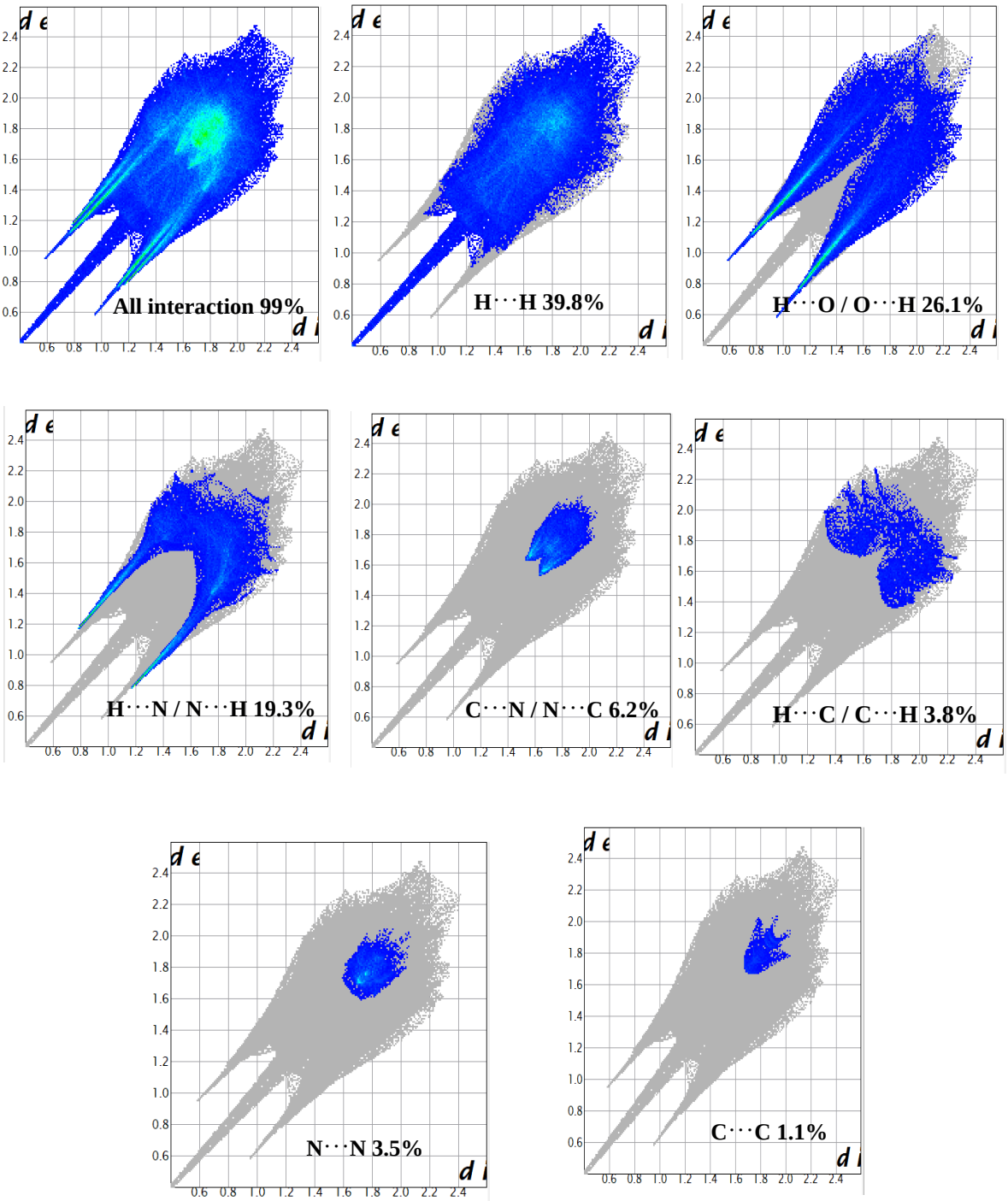

Figure III.4. 2D fingerprint plots showing the percentage contacts of on the total Hirshfeld surface.

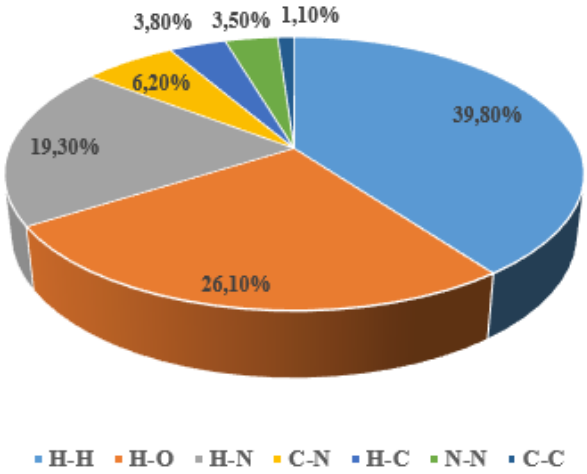

Figure III.5. Percentages of short contacts contributing to the total HS area.

III.3. Spectroscopic study

III.3.1. UV-Visible spectroscopy

The absorption electronic spectrum (Figure III.6) shows that the title hybrid material is transparent in the entire visible and UV near visible domains, in the far UV domain, it is characterized by a strong absorption band at 206 nm, that can be assigned to π→π* electronic transition, and an absorption band at 235 nm attributed to n→π*. In addition, the gap energy (Eg) is an energy width where no electronic levels exist between HOMO and LUMO, and gives information about the reactivity of molecules, the Eg value can be calculated form the absorption electronic spectrum. According to the Kubelka–Munk formula [12,13], the absorption coeffiients "F(R)" can be derived from the reflctance curves "R":

$$F(R) = (1 - R)^2 / 2R \qquad \textbf{III.3}$$

Eg considering direct transitions is estimated from the Tauc plots by extrapolating of the linear part of the curve $(F(R).h\nu)^2$ versus photon energy (hv) [14.15], as shown in the insert (b) of Figure III.6. The Eg was found to be 5.05 eV

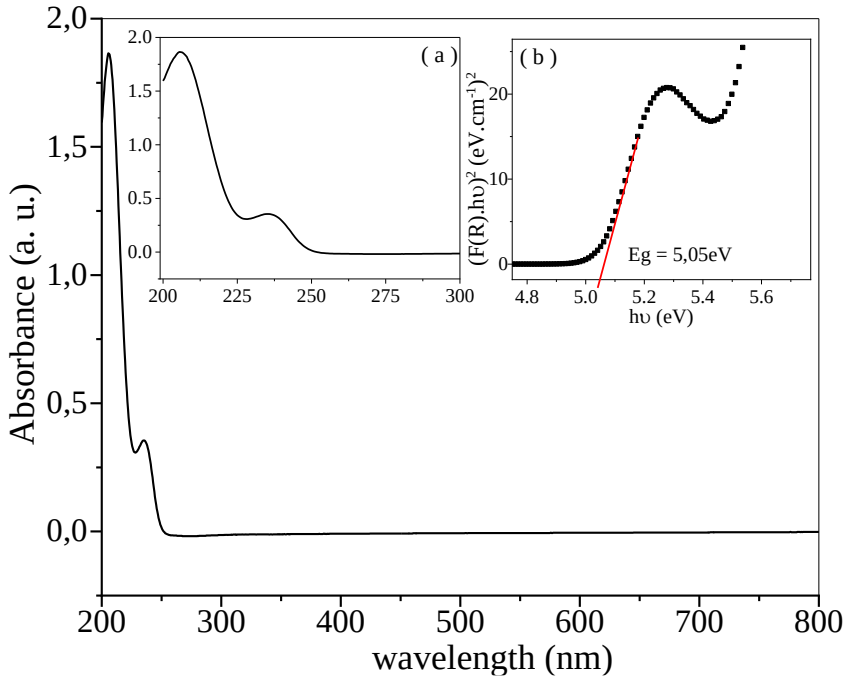

Figure III.6. UV–Visible absorption electronic spectrum of $3C_3H_7N_6^+.HPO_4^{2-}.H_2PO_4^-.4H_2O$ insert (a): magnification around the absorption bands, insert (b): caculation of the gap energy Eg.

III.3.2. FT-IR spectroscopy

The Figure III.7 shows FT-IR spectrum of $3C_3H_7N_6^+.HPO_4^{2-}.H_2PO_4^-.4H_2O$ material. The characteristic vibrational frequencies were assigned to the various functional groups of the molecular structure and listed in Table III.4, arising from internal vibrations of melaminium cation, monodrogenphosphate and dihydrogenphosphate anions, the water molecules and the vibrations of hydrogen bonds.

Table III.4. FT-IR vibrationnal wavenumbers (cm^{-1}) and assignements.

FT-IR (cm^{-1})	Assignments
3414	O–H stretching of water
3331	N–H stretching of NH_2
3076	N–H···O, N–H···N stretching
2823	P–O–H asymmetric stretching of hydroxide group
2681	P–O–H symmetric stretching of hydroxide group
2344	O–H···O asymmetric stretching, with water molecules
2330	Vibrations of hydrogen bonds formed by water molecules
1723	NH_2 bending
1668	H_2O in plane bending
1615	Ring: quadrant stretching; NCN bending + ring deformation
1554	H_2O in plane bending
1513	Side-chain asymmetric C–N stretching
1485	Ring triazine
1406	Ring: semi-circle stretching + exogenous C–N contract
1371	Ring: semi-circle stretching + exogenous C–N contract
1334	Ring: semi-circle stretching
1330	Ring: semi-circle stretching
1265	P=O stretching
1087	P–O asymmetric stretching
1033	Triazine ring vibration
1022	P–O symmetric stretching
998	Triazine ring N, in phase radial type of vibration
930	P–O–H deformation
772	Ring sextant out of plane bending
543	Symmetric type triazine ring

The bands appearing at 3414, 3331 and 3076 cm^{-1} are due to O–H vibrations of water molecules, NH_2 groups and the vibrations of hydrogen bonds respectively [12,16]. The medium and broad bands at 2823 and 2681 cm^{-1} are attributed to P–OH stretching [1,13,16], while vibrations of hydrogen bands formed by water molecules appeared at 2344 and 2330 cm^{-1} [1,3,14-16]. The two strong bands at 1723 and 1668 cm^{-1} are attributed to the bending mode of N–H [16,17] and OH respectively. In addition, the bands observed in the range of 1615–1330 cm^{-1} are due to triazine ring stretching. The medium bands at 1265, 1087 and 878 cm^{-1} are assigned to the stretching vibrations of P=O, P–O and P–O(H) respectively, these bands indicate the presence of HPO_4^- and HPO_4^{-2} entity in the structure of the material [1,16,18]. The band at 1033 cm^{-1} is assigned to triazine ring breathing mode [17,19],

however, the band at 998 cm^{-1} was attributed to in-plane vibration of the triazine ring [20]. The IR band at 930 cm^{-1} is due to P–O–H deformation vibration. Furthermore, the medium band at 772 cm^{-1} is due to sextant out of plane bending vibration [20]. The IR band at 543 cm^{-1} can be attributed to side chain in plane C–N bending vibration. All this assignment bands agree well with SXRD results.

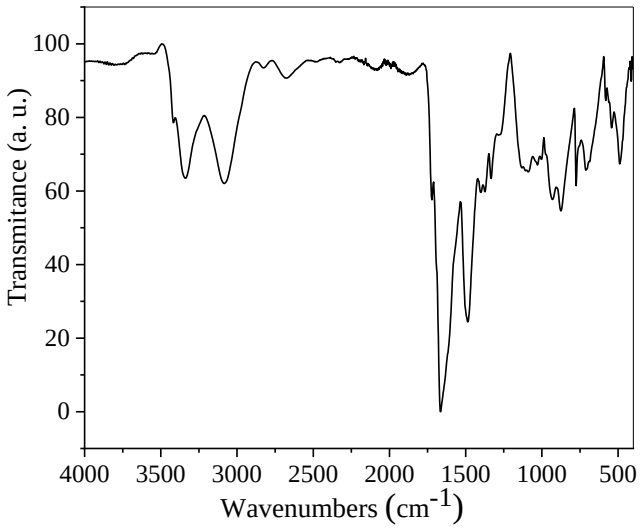

Figure III.7. FT-IR spectrum of $3C_3H_7N_6^+.HPO_4^{2-}.H_2PO_4^-.4H_2O$.

III.4. Thermogravimetric and Differential Scanning Calorimetry (DSC) studies

The TGA/DTG curves recorded for the synthesized $3C_3H_7N_6^+.HPO_4^{2-}.H_2PO_4^-.4H_2O$ material are shown in the Figure III.8.

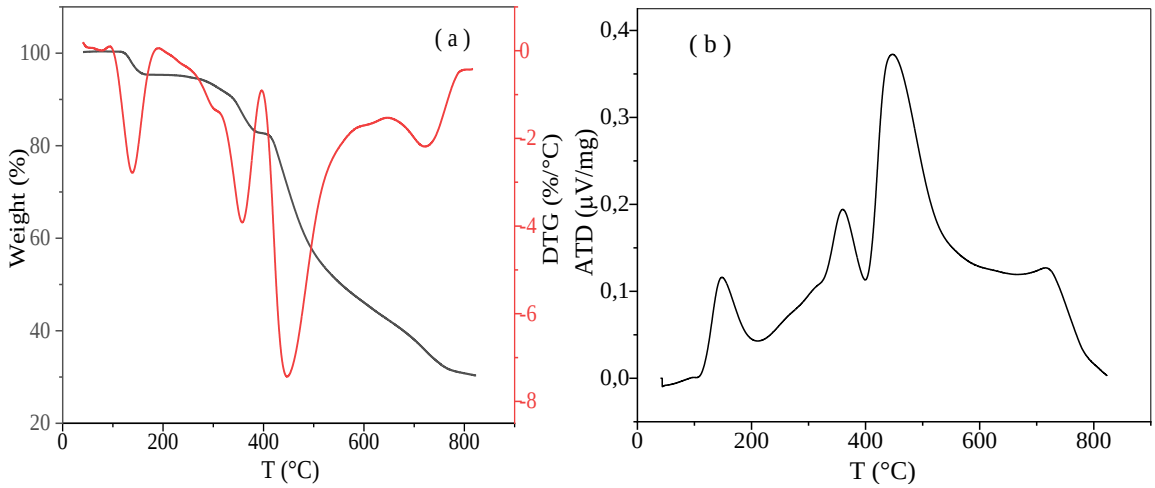

Figure III.8. (a) TGA-DTA, (b) DCS thermograms of $3C_3H_7N_6^+.HPO_4^{2-}.H_2PO_4^-.4H_2O$.

The TGA curve shows that the decomposition until 30 % of $3C_3H_7N_6^+.HPO_4^{2-}.H_2PO_4^-.4H_2O$ occurs in four stages involving dehydration and decomposition, noting the absence of melting point. The first decomposition stage was observed between 130 and 160 °C, indicating that hydrated water molecules of this hybrid material was eliminated with a weight loss of 4.7 %. The second and third stages of decomposition take place in the temperature range from 350 to 370 °C and from 410 to 460 °C, with significant weight loss of 12.31% and 52.06%, and are due to the elimination of melaminium cations, these two stages correspond to DTA peaks at 358 °C and 447 °C respectively. Generally, thermal decomposition of melamine proceeds in stages and is accompanied by the detachment of ammonia. Melamine first decomposes into melam and then melon. The NH_2 groups in melam can be replaced by other atoms and groups [21]. The last stage takes place from 500 to 790 °C suggesting that monohydrogenphosphate and dihydrogenphosphate anions are eliminated from the structure of the title compound with 30.33 % weight loss and a corresponding DTA peak centered at 722 °C. Noting that, the compound is thermally stable before and after dehydration until 127 and 340 °C respectively.

The DSC thermogram of the title hybrid material (Figure III.8 (b)) exhibits four exothermic peaks at 147, 359, 477 and 715 °C. Those peaks are correlated with TGA analysis results.

Conclusion

In this work, a new hybrid material ionic Tris(melaminium) monodrogenphosphate dihydrogenphosphate tetrahydrate $3C_3H_7N_6^+.HPO_4^{2-}.H_2PO_4^-.4H_2O$ as a single crystal was synthesized and its chemical formula, molecular and crystal structures were identified by using single crystal X-ray diffraction. The Hirshfeld surface analysis revealed that the H···H intermolecular contacts have the major contribution in the stabilization of the crystal structure of Tris(melaminium) monodrogenphosphate dihydrogenphosphate tetrahydrate. The UV–Vis. spectrum shows a good optical transparence in the entire visible and UV near visible domains with an absorption threshold at 235 nm, this low value may be useful for opto-electronic applications in the ultraviolet domain. Moreover, vibrational modes were studied by FT-IR spectroscopy and correlated to the affined structure. In addition, from the thermal analysis, it was found that the synthesized hybrid material divulges a good thermal stability better than the pristine melamine. This finding may be helpful in polymer processing.

References

[1] R. Bourzami, H. C. AitYoucef, N. Hamdouni, M. Sebais, Synthesis, crystal structure, vibrational spectra and thermal properties of novel ionic organic-inorganic hybrid material, Chem. Phys. Lett. 711(2018) 220-226.

[2] R. J. Gillespie, The valence-shell electron-pair repulsion (VSEPR) theory of directed valency. J. Chem. Educ. 40 (1963) 295-301.

[3] H. C. AitYoucef, R. Bourzami, Synthesis, single crystal X-ray structure and vibrational spectroscopic characterization study of a new hybrid material crystal: Bis (2, 4, 6-trihydroxy-1, 3, 5-triazin-1-ium), J. Mol. Struct. 1191 (2019) 218–224.

[4] S. Çakmak, S. Kansiz, M. Azam, A. Veyisoglu, H. Yakan, K. Min, Synthesis, Spectroscopic Characterization, Single-Crystal Structure, Hirshfeld Surface Analysis, and Antimicrobial Studies of 3-Acetoxy-2-methylbenzoic Anhydride, ACS. Omega. 7 (2022) 17192−17201.

[5] M. A. Spackman, D. Jayatilaka, Hirshfeld surface analysis. Cryst. Eng. Comm. 11 (2009) 19–32.

[6] A. Hasnaouia, I. Hdoufaneb, A. Alahyanec, A. Nayada, D. Cherqaouib, M. Ait Alia, L. El Firdoussi, Di-μ-oxidovanadium(V) di-nuclear complexes: Synthesis, X-ray, DFT modeling, Hirshfeld surface analysis and antioxidant activity. Inorg. Chim. Acta 501 (2020) 11927.

[7] J. J. McKinnon, D. Jayatilaka, M. A. Spackman, Towards quantitative analysis of intermolecular interactions with Hirshfeld surfaces. Chem. Commun. 37 (2007) 3814–3816.

[8] Z. Fellahi, H. C. Aityoucef, D. Hannachi, A. Djedouani, L. Ouksel, M. François, S. Fleutot, R. Bourzami, Synthesis, X-ray crystallography, Hirshfeld surface analysis, thermal properties and DFT/TD-DFT calculations of a new material hybrid ionic ($C_{10}H_{18}N_2O_8^{2+}\cdot 2ClO_4^-.4H_2O$), J. Mol. Struct. 1244 (2021) 130955.

[9] A. Y. L. Meyer, The size of molecules. Chem. Soc. Rev. 15 (1986) 449–474.

[10] J. Rudnick, G. Gaspari, The asphericity of random walks. J. Phys. A: Math. Gen. Phys. 19 (1986) 191–193.

[11] A. Baumgartner, Shapes of flexible vesicles at constant volume. J. Chem. Phys. 99 (1993) 7496–7501.

[12] N. B. Colthup, L. H. Daly, S. E. Wiberley, Introduction to Infrared and Raman Spectroscopy, 3rd ed. London: Academic Press, Inc., 1990.

[13] D. E. C. Corbridge, M. Grayson, E. J. Griffith, Topics in Phosphorus Chemistry. New York: Interscience, 6 (1964).

[14] M. K. Marchewka, Infrared and Raman spectra of melaminium chloride hemihydrate. Mater. Sci. Eng. B. 95 (2002) 214-221.

[15] M. K. Marchewka, Infrared and Raman spectra of melaminiumbis (4-hydroxybenzenesulfonate) dehydrate. Acta. Chim. Solv. 50(2) (2003) 239-250.

[16] H. AitYoucef, S. Chafaa, R. Doufnoun, T. Douadi, Synthesis, characterization and thermal behavior of tetrakis (melamine2+) bis (melamine+) pentakis (monohydrogenphosphate) tetrahydrate, J. Mol. Struct.1123 (2016) 138-143.

[17] W. J. Jones, W. J. Orville-Thomas. Trans. Faraday Soc. 55 (1959) 193-202.

[18] L. C. Thomas, Interpretation of the Infrared Spectra of Organophosphorus Compounds, Heyden, London, 1974.

[19] Y. L. Wang, A. M. Mebel, C. J. Wu, Y. T. Chen, C. E. Lin, J. C. Jiang, IR spectroscopy and theoretical vibrational calculation of the melamine molecule. J. Chem. Soc. Faraday Trans. 93 (1997) 3445-3451.

[20] P. J. Larkin, M. P. Makowski, N. B. Colthoup, The form of the normal modes of s-triazine: infrared and Raman spectral analysis and ab initio force field calculations. Spectrochim. Acta A, 55 (1999) 1011-1020.

[21] E. C. Franklin, The ammono carbonic acids. J. Am. Chem. Soc. 44 3 (1922) 486–509.

CHAPTER IV:
Synthesis, structural characterization and thermal behavior of Hyb 2 and its complex Cu(II)

In this chapter, we present the synthesis of a new single-crystal hybrid ionic material called 2,4,6-triamino-1,3,5-triazinium perchlorate monohydrate (Hyb 2) and its complex Cu(II). The studies of structure of Hyb 2 by single crystal X-ray diffraction, as well as, the 3D-supramolecular structure basing on the SXRD data. Additionally, the studied UV-visible and FT-IR spectroscopies have also been studied to establish optical and vibrational properties. The study of thermal decomposition of hybrid material was also occurred by TGA/DTG techniques.

IV.1. Synthesis and crystallization

The solution of perchloric acid was added drop by drop to the aqueous solution of melamine in hot distilled water, in the 1:1 molar ratio. Then the reaction mixture was brought under magnetic stirring to reflux for 6 hours. No precipitate was observed; the mixture was allowed to evaporate slowly at room temperature. After one day, colorless transparent single crystals are formed; filtered and washed with ethanol, and then dried in air. The reaction scheme is shown in Scheme IV.1.

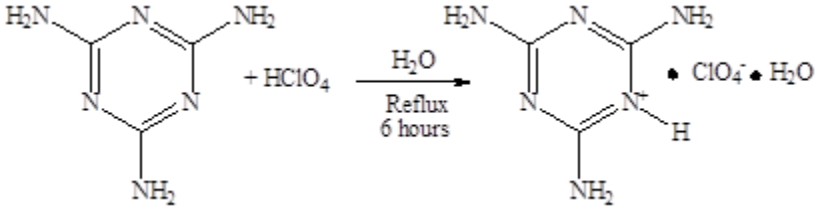

Scheme IV.1. Reaction scheme of the 2, 4, 6-triamino-1, 3, 5-triazinium perchlorate monohydrate.

IV.2. Structural Characterization

IV.2.1. Single crystal study

The asymmetric unit of the title material is depicted in Figure IV.1. It is made up of a water molecule, a single negative charge perchloric acid anion ClO_4^-, and a single proton melamine M^+ cation at N atom of the s-triazine ring. Together, these components give the chemical formula $C_3H_7N_6^+.ClO_4^-.H_2O$.

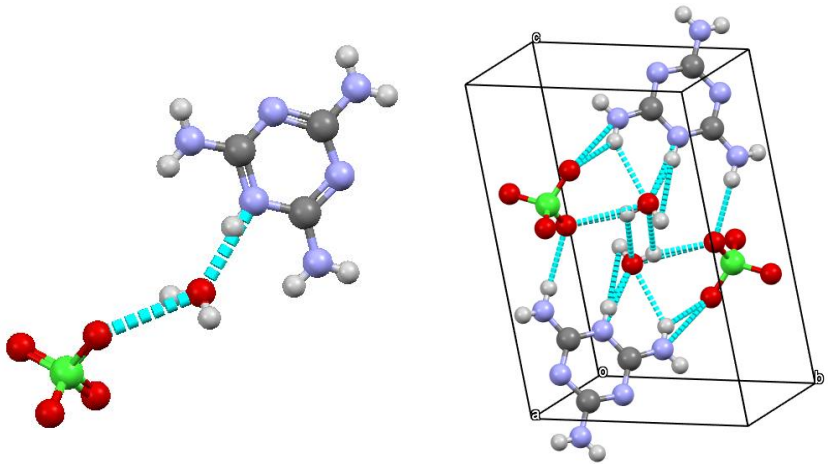

(a) (b)

Figure IV.1. Crystal data (a) asymmetric unit, and (b) unit cell, both provided by hydrogen bonding system.

Furthermore, the experimental crystal data and structural refinement parameters are listed in the Table IV.1. Two asymmetric units (Z = 2) form the triclinic unit cell, which has space group P_1^- and the cell parameters a = 5.6698 (4), b = 7.5566 (6), c = 11.9230 (9) Å, α = 102.738 (2), β = 94.527 (3), and γ = 110.673 (2). Instead of being centrosymmetric, the unit cell has an identity symmetry and an initial center of inversion at the origin (000). In addition, the found triclinic unit cell with space group P1 was published for the first time in the crystallography report of M. M. Zhao and al. in (2010) [1], and were then confirmed by powder-XRD in (2013) by N. Kangathara and al [2]. In addition, the R-factor is less than 0.05 (0.03), and the goodness is close to 1 (S=1.09) indicating a high confidence level in the described supramolecular structure [3].

Table IV.1. Crystal data, data collection and structure refinement parameters.

Empirical formula	$C_3H_9ClN_6O_5$
Crystal system	Triclinic
Molecular weight (g/mol)	244.61
Space group	P_1^-
a (Å)	5.6698 (4)
b (Å)	7.5566 (6)
c (Å)	11.9230 (9)
α (°)	102.738 (2)
β (°)	94.527 (3)
γ (°)	110.673 (2)
V (Å^3)	459.25 (6)
Z	2
Crystal size (mm^3)	0.60*0.58*0.52
Crystal color/habit	Colourless/Prism
D_{calc} (mg/m^3)	1.769
$\lambda_{MoK\alpha1}$ (Å)	0.71073
Temperature (K)	150
μ (mm^{-1})	0.44
F (000)	676
θ Range (°)	3.0→27.4
Δ ρ_{max} (eÅ^{-3})	0.63
Δ ρ_{min} (eÅ^{-3})	-0.45
h	-7→7
k	-9→9
l	-15→15
Measured reflections	10223
Independent reflections	2080
reflections with I>2σ(I)	1929
No. of parameters	502

R_{int}	0.041
R [F^2>2σ(F2)]	0.030
wR(F^2)	0.076
S	1.09

Furthermore, SXRD shows that weak bonds, primarily hydrogen ones, preserve the crystal structure, producing a type I hybrid material, counting 13 hydrogen bonds per asymmetric unit of type N–H···N, N–H···O, N^+–H···O, and O–H···O, under 3.2 Å as the greatest distance between donor and acceptor. The hydrogen bonds of a formal asymmetric unit are listed in Table IV.2 along with their properties, including bond lengths, angle measurements, and symmetry codes.

Table IV.2. Hydrogen-bond geometry and their symmetry codes.

D—H···A	D—H	H···A	D···A	D—H···A
N1—H1N···O5	0.87 (2)	1.87 (2)	2.7262 (16)	167 (2)
N6—H6A···N3^{i}	0.83 (2)	2.26 (2)	3.0867 (17)	174.5 (18)
N4—H4A···O4^{ii}	0.86 (2)	2.19 (2)	2.9889 (18)	154.2 (19)
N6—H6B···O2^{iii}	0.82 (2)	2.23 (2)	3.0397 (16)	169.5 (19)
N5—H5A···O2^{iv}	0.85 (2)	2.23 (2)	2.8923 (16)	134.8 (19)
N5—H5A···O5	0.85 (2)	2.46 (2)	3.1554 (17)	138.8 (18)
O5—H5W1···O3^{iv}	0.85 (3)	2.16 (3)	2.9669 (17)	157 (2)
O5—H5W1···O5^{v}	0.85 (3)	2.63 (3)	3.081 (2)	114 (2)
N4—H4B···O3^{vi}	0.87 (2)	2.33 (2)	3.0980 (18)	147 (2)
N4—H4B···O4^{vii}	0.87 (2)	2.53 (2)	3.1197 (18)	126.1 (19)
O5—H5W2···O1	0.80 (3)	2.18 (3)	2.8919 (16)	149 (3)
O5—H5W2···O4^{vii}	0.80 (3)	2.46 (3)	2.8733 (16)	113 (2)
N5—H5B···N2^{viii}	0.85 (2)	2.16 (2)	3.0065 (17)	178 (2)

Symmetry codes: (i) −x, −y+2, −z+2; (ii) −x+1, −y+2, −z+1; (iii) x−1, y, z+1; (iv) −x+2, −y+1, −z+1; (v) −x+1, −y+1, −z+1; (vi) x−1, y, z; (vii) −x+2, −y+2, −z+1; (viii) −x+1, −y+1, −z+2.

IV.2.1.1. 3D-supramolecular network

The molecules in the self-assembled 3D-supramolecular network of the title material form a three-dimensional complex arrangement; the hydrogen bonding system has been proposed as the mechanism that organizes molecules in this paragraph.

Linear supramolecular chains along the diagonal direction of the plane (Oab) can be seen in the melamine molecules, in which every two successive molecules have a point of symmetry, they are inverted, attributing consequently a zigzag form to the supramolecular chains. The melaminium molecules on the chain are linked by hydrogen bonds of the type N─H···N, and the distance between donor and acceptor is 3.086 Å (Figure IV.2 (a)). The organic chains are aligned parallel to each other with a separation distance of 5.67 Å, which any hydrogen bond can be remarked at this distance, and they are bonded indirectly via the inorganic part (Figure IV.2 (b)).
Regarding the inorganic part, linear supramolecular chains are observed along the direction (Ob), these chains are made of an alternation of water and perchlorate anion molecules, and hydrogen bonds of type O5─H···O4 binds the molecules in the chain, with donor-acceptor distances of 2.462 Å as depicted in (Figure IV.2 (c)).

Moreover, the organic and the inorganic components are mainly interconnected by electrostatic interactions and a hydrogen bond between melaminuim molecules and perchlorate anions of the type N4─H4···O4 and N1─H1N···O5, with donor-acceptor distances of 2,989 and 2,726 Å respectively as shown in (Figure IV.2 (d)).
Finally, an alternation of the organic and inorganic components is formed, giving the 3D-supramolecular network a layered structure in the direction (Oc), in which each organic or inorganic layer is made up of two supra-molecular sub-layers as illustrated in (Figure IV.2 (e)).

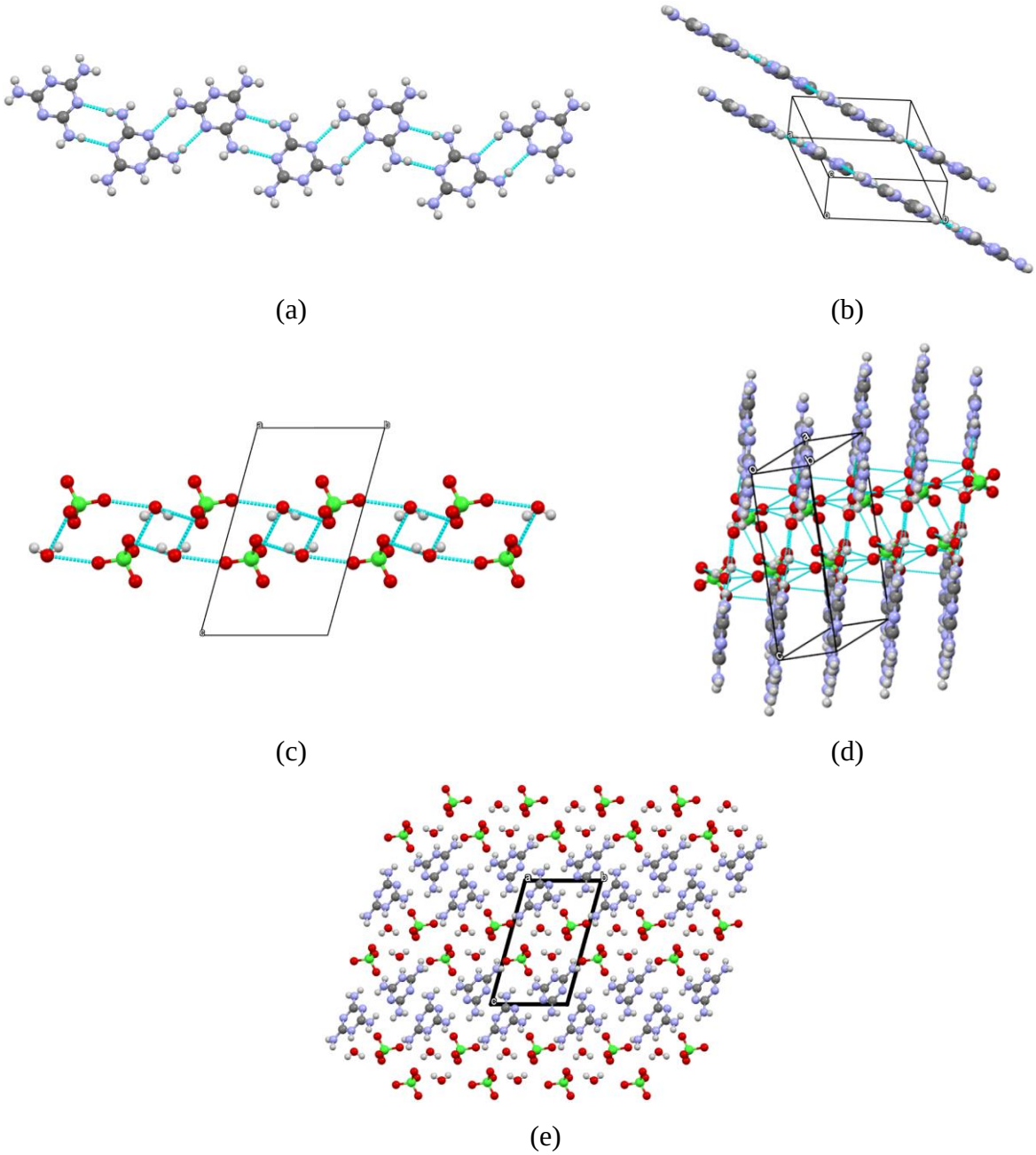

Figure IV.2. 3D-supramolecular network (a and b) Linear supramolecular chains along the diagonal direction of the plane (Oab) (c) linear supramolecular chains are observed along the direction (Ob) in the inorganic part (d) illustration of the interconnection of the organic and the inorganic parts (e) 3D-supramolecular network illustrating the layered structure in the direction (Oc).

IV.2.1.2. Hirshfeld surface (HS) analysis

The HS was generated based on the d_{norm}, shown in Figure IV.3(a). In this illustration, the white surface corresponds to contact distances equal to the sum of van der Waals radii. Furthermore, interactions are highlighted by colors: red indicates closer contacts (shorter distances than van der Waals radii), while blue indicates contacts that are more distinct (longer distances than van der Waals radii) [4]. This analysis provides a visual insight into the nature and strength of intermolecular interactions present in the crystal of the material.

The shape index surface is a crucial visual tool for identifying specific stacking modes in molecular structures, including planar stacking as well as aromatic interactions such as C-H···π and π···π. The interactions C-H···π interactions are specifically represented as 'red p-holes', signalling electronic interactions between CH groups and the aromatic centers of the adjacent molecular rings. This visual representation makes it easier to understand the geometric arrangements and electronic interactions within molecular assemblies. In this way, the Figure IV.3 (b) reveals that material lacks any C-H···π interactions. In contrast, the Hirshfeld surface shape index persuasively highlights the π···π stacking across the adjacent red and blue triangles, confirming these interactions for material.

Furthermore, the curvedness, which reflects the mean square curvature of the surface, the green regions (relatively flat) with dark blue edges (high positive curvature). The flat regions observed on the curvature surface in Figure IV.3(c) also confirm the presence of π···π interactions in material.

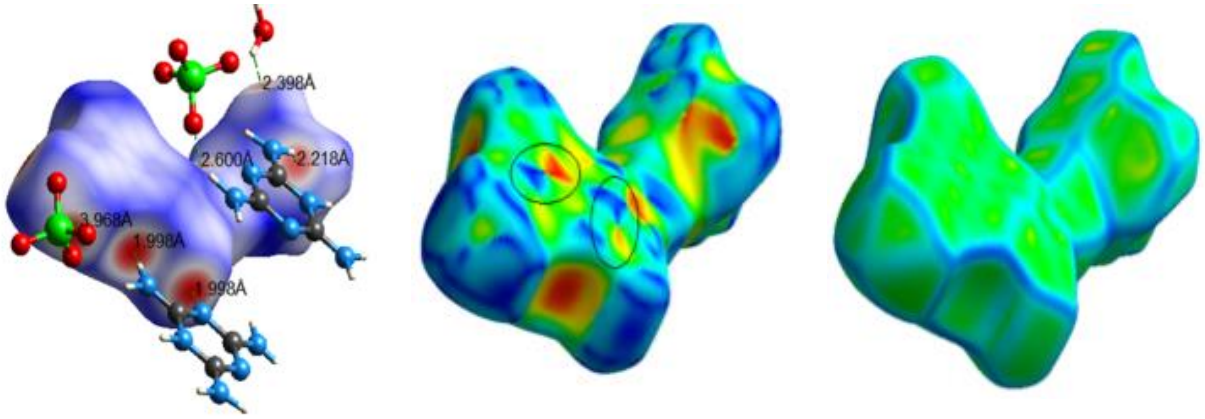

(a) (b) (c)

Figure IV.3. Views of the Hirshfeld surfaces of the title material plotted over: (a) d_{norm}, (b) shape-index map and (c) curvedness map.

The Figure IV.4 (a) presents the overall two-dimensional fingerprint plots, subdivided into various interactions crucial for understanding crystal packing. These interactions are detailed in Figure II.4 (a to j), illustrating H...O/O...H, H...N/N...H, H...H, N...O/O...N, C...O/O...C, H...C/C...H, O…O, N…N, and C...N/N...C interactions, along with their respective contributions to the HS [5].

Among these interactions, OH…H/H…OH contacts are particularly significant, constituting 48.7 % of the overall crystal stacking, depicted by widely dispersed blue points. This prevalence is attributed to the substantial hydroxyl content of the molecule, with the end at de = 1.2 Å, di = 0.8 Å.

In the presence of C–H···π interactions, distinctive wing-shaped patterns, with tips located at the combined distances of de + di = 3.80 Å, are observable in the fingerprint trace enclosed by H···C/C···H contacts (Figure IV.4 (g)), contributing 3.2% to the HS. The structural characteristics are further emphasized by a notable proportion of H···N/N…H contacts, constituting approximately 17.4 % of the molecular surface, the corresponding fingerprint plot (Figure IV.4(c)) illustrate the shortest H···N contacts as a pair of spikes at de + di ≈ 2 Å.

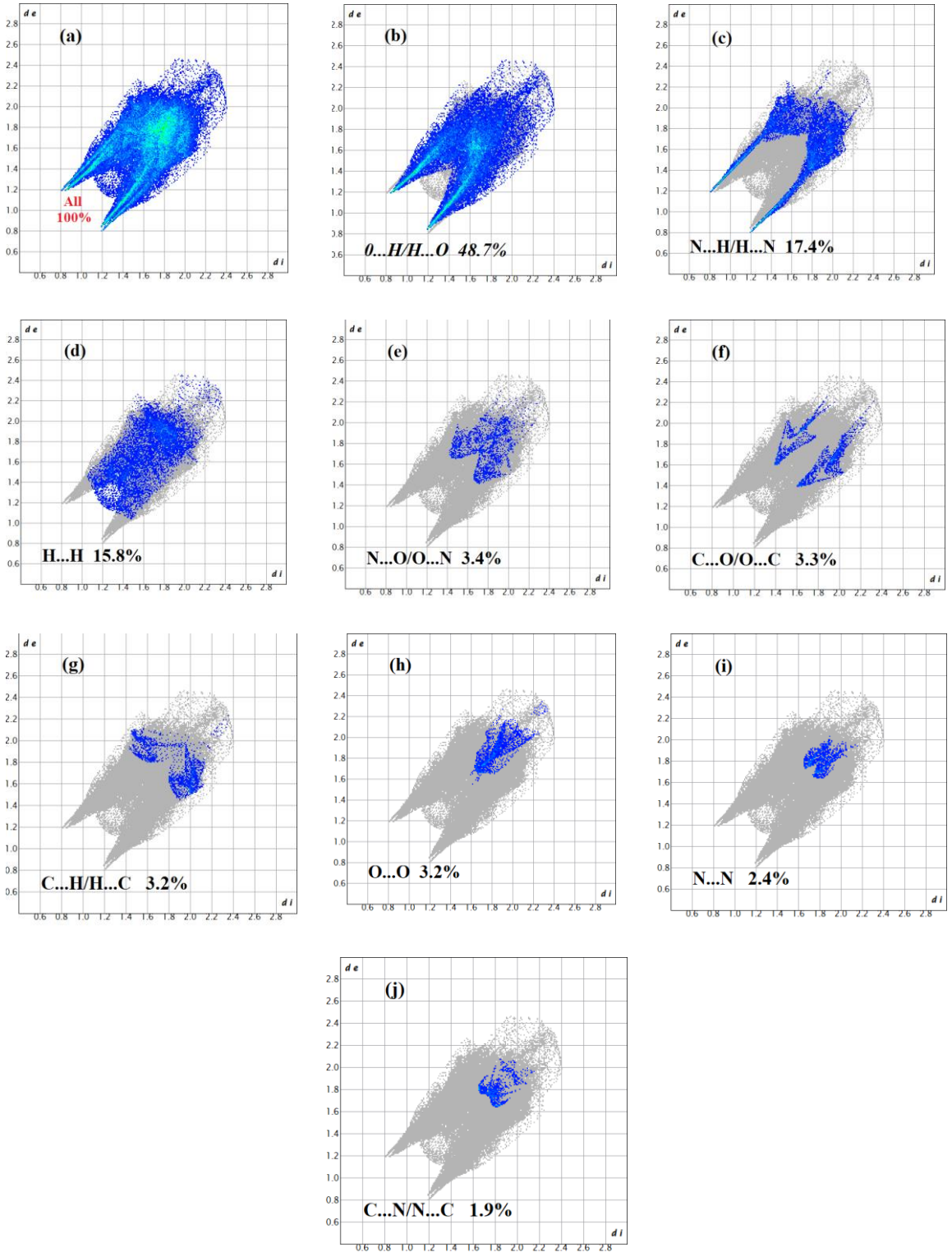

Figure IV.4. 2D fingerprint plots of the material showing the percentages of contacts contributed to the total Hirshfeld surface.

IV.3. Spectroscopy results

IV.3.1. UV-Visible spectroscopy

The electronic absorption spectrum of the 2, 4, 6-triamino-1, 3, 5-triazinium perchlorate monohydrate was recorded in distilled water at room temperature in the range 200-800 nm and shown in Figure IV.5. It shows two absorption bands, the first one at 210 nm, that can be attributed to the $\pi \rightarrow \pi^*$ electronic transition of the triazine ring, while the second absorption band at 238 nm, that can be assigned to $n \rightarrow \pi^*$. This may be due to nitrogen-containing aromatic systems or electronic excitation in this region [6-8]. Around the gap, more tightly the valence electrons that are closer to the nucleus. A high energy excites the electrons to higher energy bands, giving an absorption of the incident light, in opposite, the light with an energy far in the gap is unable to rise electrons to next band and pass through the structure without absorption. Over the cut-off wavelength λ=252 nm to λ=800 nm corresponding to the near UV and the visible domains, the hybrid material is transparent.

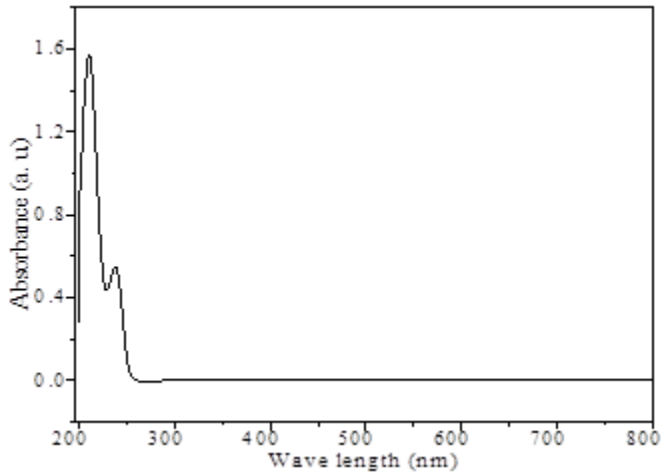

Figure IV.5. UV–Visible absorption electronic spectrum of the 2,4,6-triamino-1,3,5-triazinium perchlorate monohydrate in water solution.

IV.3.2. FT-IR spectroscopy

The FT-IR spectrum of the hybrid material was obtained over a spectral range of 4000-450 cm^{-1} (Figure IV.6). The absorption bands observed in the range 3600-3120 cm^{-1} are attributed to the stretching vibration of H_2O, NH_2 groups and vibrations of hydrogen bonds [9-13]. As well as, the bands related to the bending vibrations of NH and OH are located at 1695 and 1629 cm^{-1} respectively [9-12]. The combination tone: NH_2 symmetric stretch-side chain out of plane C-N bonds appeared at 2722 cm^{-1} and C-N bending vibration observed at 574 cm^{-1}

[12]. The IR bands corresponding to the stretching vibrations of the triazine-ring appear in the range 1600-1520 cm^{-1}. Moreover, the two absorption bands at 1059 cm^{-1} and 628 cm^{-1} are due to the asymmetric and symmetric stretching vibration of ClO_4^- respectively [14-16].

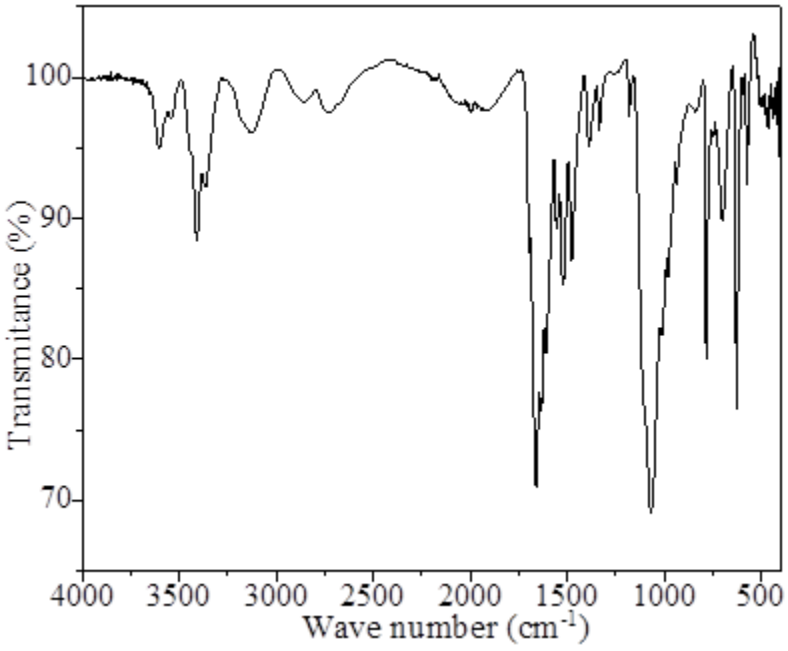

Figure IV.6. FT-IR spectrum of the 2, 4, 6-triamino-1, 3, 5-triazinium perchlorate monohydrate crystal.

The most significant infrared adsorption wavenumbers detailed are reported in the Table IV.3:

Table IV.3. Most significant FT-IR vibrationnal wavenumbers (cm^{-1}) and their assignements.

Wavenumber	Assignments
3547	O–H symmetric stretching of water
3404	NH_2 symmetric stretching of vibration
3363	NH_2 asymmetric stretching of vibration
3121	Vibrations of hydrogen bonds
2722	Combination tone: NH_2 symmetric stretch-side chain out of plane C-N bonds
1660	H_2O in plane bend
1552	H_2O in plane bending
1476	Side-chain asym C-N stretch
1059	ClO_4^- asymmetric stretching vibration
628	ClO_4^- asymmetric bending type of vibration
574	C-N bending vibration

All this assignment bands agree well with single-crystal XRD results, and with our previous similar hybrid material [9,10,14,17,18].

IV.4. Thermogravimetric study

The Figure IV.7 presents the TGA/DTG curves recorded on the 2, 4, 6-triamino-1, 3, 5-triazinium perchlorate monohydrate crystal. The TGA curve proves that this hybrid is stable until 117 °C before dehydration and 315 °C after dehydration, while its total decomposition is achieved at 800 °C, and occurred in seven stages, involving dehydration and decomposition. The elimination of the structural water molecule was observed in the first decomposition stage on the mass loss curve between 120 °C and 169 °C, accompanied by a DTG peak at 123 °C. Whereas, the second, third, fourth and fifth stages of decomposition took place in the temperature range from 285 to 472 °C, and are due to the elimination of melaminium moiety, and the corresponding DTG peaks were obtained at 300, 370, 384 and 428 °C respectively. The thermal decomposition of melamine occurs in multiple stages. Its accompanies by the detachment of ammonia. The melamine decomposes into melam and then melon. Other groups can replace the NH_2 groups of melam. Whereas, the two last stages observed from 676 to 773 °C accompanied by an elimination of perchlorate anion moieties, and the corresponding DTG peak were obtained at 713 and 744 °C. In addition, about 30% of the residue remains after temperatures surpassing 550°C. For example, this characteristic could

potentially improve the thermal properties of organic materials as polymer matrices, as well as other related applications [19-24].

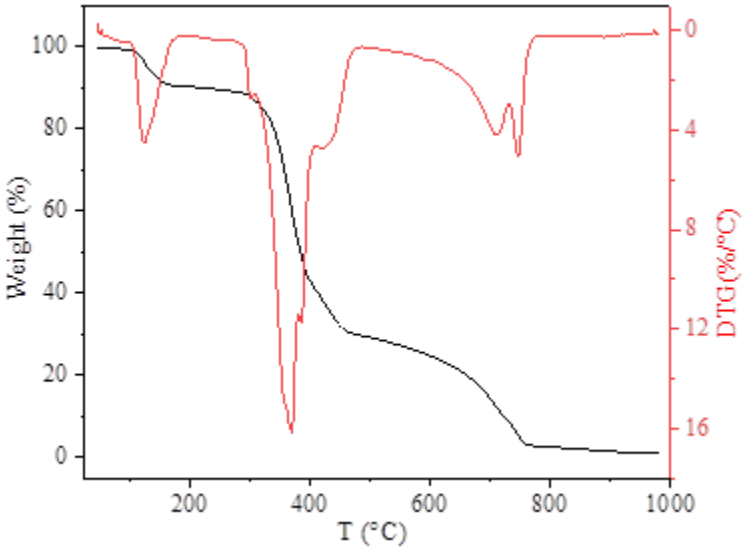

Figure IV.7. TGA-DTG curves of $C_3H_7N_6^+.ClO_4^-.H_2O$ 2, 4, 6-triamino-1, 3, 5-triazinium perchlorate monohydrate crystal.

Reference

[1] M. M. Zhao, P. P. Shi, Melaminium perchlorate monohydrate. Acta crystallogr. E, 66(6) (2010) 1463- 1463.

[2] N. Kanagathara, M.K. Marchewka, M. Drozd, N.G. Renganathan, S. Gunasekaran, G. Anbalagan, FT-IR, FT-Raman spectra and DFT calculations of melaminium perchlorate monohydrate, Spectrochim. Acta A: Mol. Biomol, 112 (2013) 343–350.

[3] J. F. Stoddart, Supramolecular Chemistry: From Molecular Information to the Design of Functional Systems. Nature Reviews Chemistry, 1(4) (2017) 1-18.

[4] S. Dekar, M. Merzougui,J. Weiss, K. Ouari. Structural investigations and catalytic performances of a new oxovanadium complex derived from 1, 2-bis ((E)-5-bromo-2-hydroxybenzylideneamino)-4-methylbenzene. J. Mol. Struct. 1261 (2022) 132888.

[5] M. Sessolo and H. J. Bolink, "Hybrid organic-inorganic light-emitting diodes," Adv. Mater.23 (16) (2011) 1829–1845.

[6] K. Kirubavathi, K. Selvaraju, S. Kumararaman, Growth and characterization of a new metal-organic nonlinear optical bis (thiourea) cadmium zinc chloride single crystals. Spectrochim. Acta A 71 (2008)1–4.

[7] G. Madhurambal, B. Ravindran, M. Mariappan, S.C. Mojumdar, Thermal, UV and FTIR spectral studies in alkali metal cinnamates. J. Therm. Anal. Calorim. 100 (2010) 811–815.

[8] V. Sangeetha, K. Gayathri, P. Krishnan, N. Sivakumar, N. Kanagathara, G. Anbalagan, Growth, optical, thermal, dielectric and microhardness characterizations of melaminium bis (trifl uoroacetate) trihydrate single crystal, J. Cryst. Growth. 389 (2014) 30–38.

[9] H. AitYoucef, S. Chafaa, R. Doufnoun, T. Douadi, Synthesis, characterization and thermal behavior of tetrakis (melamine2+) bis (melamine+) pentakis (monohydrogenphosphate) tetrahydrate, J. Mol. Struct.1123 (2016) 138-143.

[10] M. Latoui, H. C. AitYoucef, F. Benghanem, V. Dorcet, R. Bourzami. New organic-inorganic hybrid ionic material Tris (melaminium) monodrogenphosphate dihydrogenphosphate tetrahydrate: Synthesis, single-crystal structure, Hirshfeld surface analysis, spectroscopic characterization, and thermal behavior. J. Mol. Struct. 1300 (2024) 137312.

[11] N.B. Colthup, L.H. Daly, S.E. Wiberley, Introduction to Infrared and Raman Spectroscopy, third ed., Academic Press Inc, London, 1990.

[12] W.J. Jones, W.J. Orville-Thomas, The infra-red spectrum and structure of dicyandiamideTrans. Faraday Soc. 55 (1959) 193-202.

[13] H. Tanak, M. K. Marchewka, M. Drozd. Molecular structure and vibrational spectra of Bis (melaminium) terephthalate dihydrate: A DFT computational study. Spectrochim. Acta. A. Mol. Biomol. Spectrosc. 105 (2013) 156-164.

[14] Z. Fellahi, H. C. Aityoucef, D. Hannachi, A. Djedouani, L. Ouksel, M. François, S. Fleutot, R. Bourzami, Synthesis, X-ray crystallography, Hirshfeld surface analysis, thermal properties and DFT/TD-DFT calculations of a new material hybrid ionic ($C_{10}H_{18}N_2O_8^{2+}\cdot 2ClO_4^-.4H_2O$), J. Mol. Struct. 1244 (2021) 130955.

[15] M.K. Marchewka, M. Drozd, A. Pietraszko, Structure, spectra and phase transition in p-nitroanilinium perchlorate crystal. Mater. Sci. Eng. B100 (2003) 225–233.

[16] M.K. Marchewka, Infrared and Raman spectra of melaminium bis (4-hydroxybenzenesulfonate) dihydrate, Acta Chim. Solv. 50 (2003) 239-250.

[17] R. Bourzami, H. C. AitYoucef, N. Hamdouni, M. Sebais, Synthesis, crystal structure, vibrational spectra and thermal properties of novel ionic organic-inorganic hybrid material, Chem. Phys. Lett. 711(2018) 220-226.

[18] H. C. AitYoucef, R. Bourzami, Synthesis, single crystal X-ray structure and vibrational spectroscopic characterization study of a new hybrid material crystal: Bis (2, 4, 6-trihydroxy-1, 3, 5-triazin-1-ium), J. Mol. Struct. 1191 (2019) 218–224.

[19] G. Bertelli, P. Busi, L. Costa, G. Camino, R. Locatelli, Polym. Degrad. Stab. 18 (4) (1987) 307-319.

[20] S. Boryniec, A. Michalski, J. Debski, Fib. Text. East. Eur. 7 (1) (1999) 58-60.

[21] Y. Liu, Q. Wang, G. Fei, Y. Chen, Preparation of polyamide resin-encapsulated melamine cyanurate/melamine phosphate composite flame retardants and the fire-resistance to glass fiber-reinforced polyamide 6, J. Appl. Polym. Sci. 102 (2) (2006) 1773-1779.

[22] W. Y. Chen, Y. Z. Wang, F. C. Chang, Thermal and Flame Retardation Properties of Melamine Phosphate-Modified Epoxy Resins, J. Polym. Res. 1 (2004)

109-117.

[23] J.R.A. Braodbent, M.M. Hirschler, Red phosphorus as a flame retardant for a thermoplastic nitrogen-containing polymer, J. Eur. Polym. 20 (1984) 1087-1093.

[24] J. Xiao, Y. Hu, L. Yang, Y. Cai, L. Song, Z. Chen, W. Fan, Fire retardant synergism between melamine and triphenyl phosphate in poly (butylene terephthalate) ,Polym. Degrad. Stab. 91 (9) (2006) 2093-2100.

CHAPTER V: RESULTS OF THE ELECTROCHEMICAL STUDY

V. Study of the electrochemical behavior of the compounds.

This chapter is devoted to the presentation of the study results electrochemical by cyclic voltammetry, potentiodynamic polarization (polarization curves) and electrochemical impedance spectroscopy (SIE).

V.1. Study of the electrochemical behavior of the compound Hyb 2

In this part of the research work, we present the electrochemical behavior of the synthesized compound $C_3H_7N_6^+.ClO_4^-.H_2O$. The study is carried out by cyclic voltamperometry on a platinum electrode in dimethylsulfoxide (DMSO) medium in the presence of lithium perchlorate ($LiClO_4$) 0.1 M in a potential range from +1600 to -1600 mV/SCE.

The domain of electroactivity is represented by the cyclic voltamogram of DMSO in the presence of 0.1 M of $LiClO_4$ in the potential range between +2200 to -2200 mV/SCE with an acquisition rate of 50 mV/s (Figure V.1).

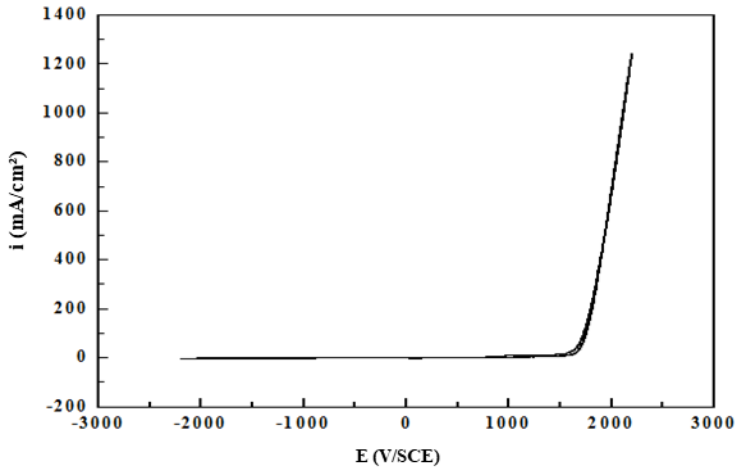

Figure V.1. Cyclic voltammogram defining the electroactivity domain of the study medium (DMSO+$LiClO_4$) 0.1 M, v =50 mV/s.

The electrochemical behavior of the $C_3H_7N_6^+.ClO_4^-.H_2O$ H solution at a concentration of 10^{-4} M was studied by cyclic voltammetry in a potential range from 0 to -1600 mV/ECS and at different scanning speeds (FigureV.2).

In the cathodic field a reduced peak located at E_{pc}= - 1120 mV/ SCE is observed, attributed to the reduction of the C=N bond. On anodic scanning, a peak at E_{pa}= -330 mV/ SCE corresponding to the reoxidation of the reduced species appears.

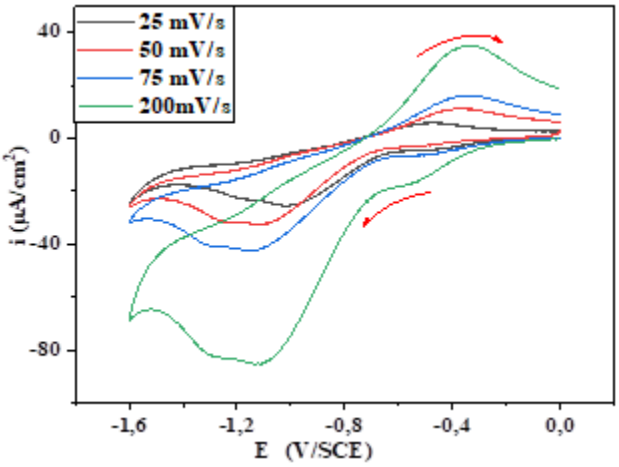

Figure V.2. Cyclic voltammograms of $C_3H_7N_6^+.ClO_4^-.H_2O$ (C=10^{-4} M) in DMSO/$LiClO_4$ 0.1 M at different scan speeds.

To study the kinetics of the electrochemical reactivity of the hybrid material, we varied the scanning speed (v = 25 to 200 mV/s). The corresponding cyclic voltammograms (Figure V.2) show that the increase in sweep speed implies an increase in peak current density. A slight shift of peak potentials is noted as the scanning speed increases. The electrochemical characteristics of the hybrid are summarized in Table V.1.

Table V.1. Electrochemical parameters of the ligand $C_3H_7N_6^+.ClO_4^-.H_2O$ (C=10^{-4} M) at different scanning speeds in DMSO/$LiClO_4$ 0.1 M.

v (mV/s)	$v^{1/2}$ (mV/s)$^{1/2}$	Log (v) (mV/s)	$-E_{pa}$ (V/SCE)	$-E_{pc}$ (V/SCE)	ΔE (V/SCE)	$-i_{pc}$ (µA/cm²)	i_{pa} (µA/cm²)	$\frac{ipa}{ipc}$
25	5	1.39	0.47	1.01	0.54	25.46	5.98	0.23
50	7.07	1.69	0.35	1.12	0.77	32.42	11.30	0.35
75	8.66	1.87	0.34	1.15	0.81	42.39	16.23	0.38
200	14.14	2.3	0.33	1.12	0.71	85.34	35.15	0.41

The evolution of peak current as a function of the scan rate (Figure V.3) and the variation of peak potential as a function of log v (FigureV.4) confirm the reduction reaction is controlled by pure diffusion and that the charge transfer process is slow.

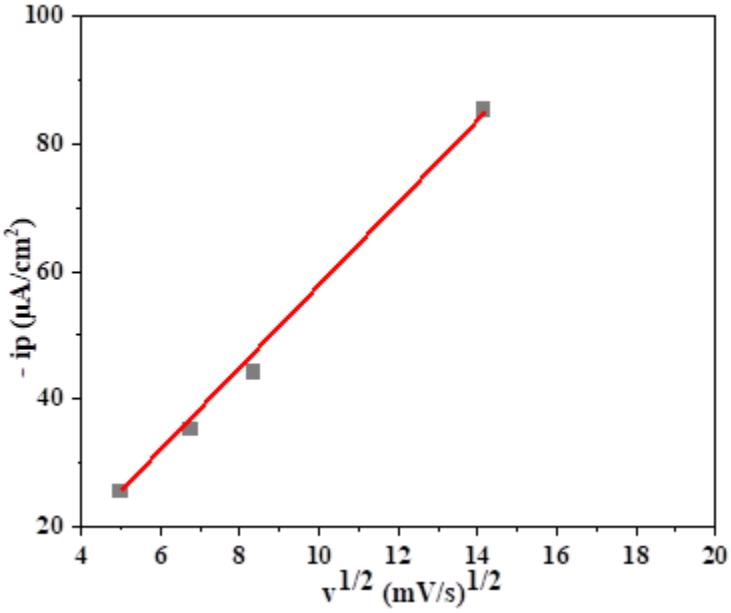

Figure V.3. Evolution of $i_{pc} = f(v^{1/2})$ for the reduction of $C_3H_7N_6^+ . ClO_4^- .H_2O$ (10^{-4}M) in (DMSO + $LiClO_4$) 0.1 M.

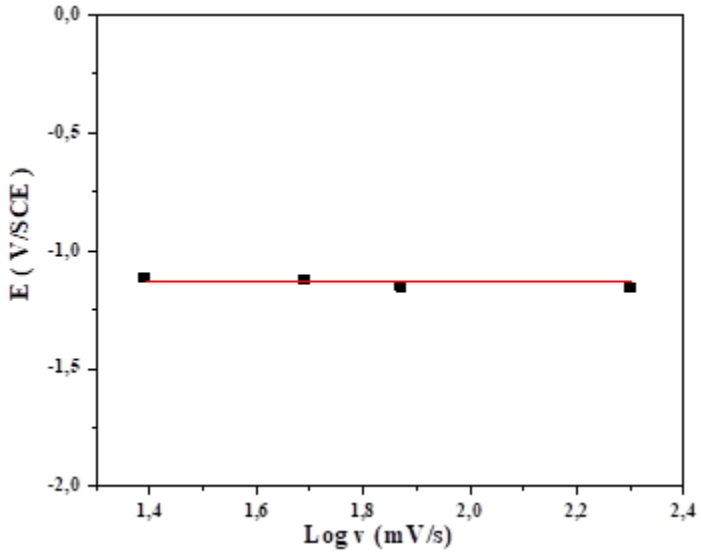

Figure V.4. Evolution of $E_{pc} = f(\log v)$ for $C_3H_7N_6^+ . ClO_4^- .H_2O$, 10^{-4}M (DMSO + $LiClO_4$) 0.1M

The cyclic voltammogram of $C_3H_7N_6^+.ClO_4^-.H_2O$ (C=10^{-4} M) recorded in a potential range of 0 to 1600 mV/ECS in DMSO/$LiClO_4$ 0.1 M (Figure V.5) shows no oxidation peaks.

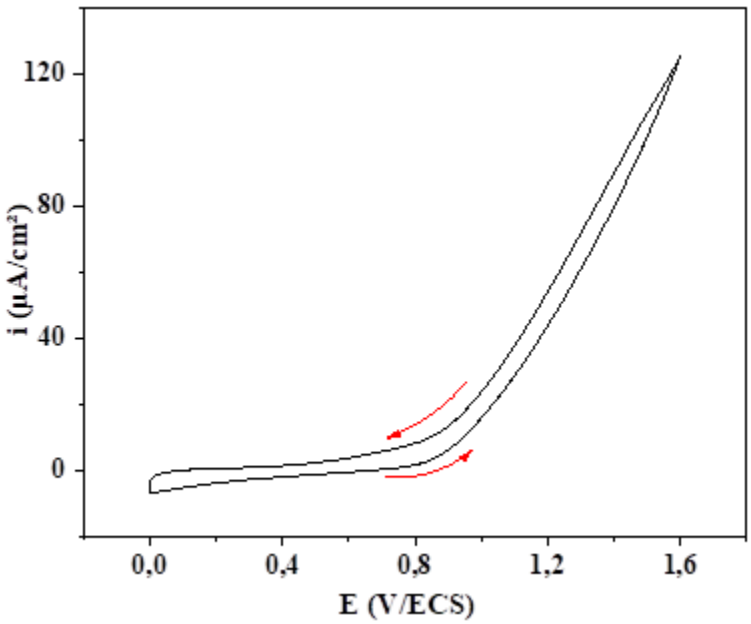

Figure V.5. Cyclic voltamperogram of $C_3H_7N_6^+.ClO_4^-.H_2O$ (C=10^{-4} M) in DMSO/$LiClO_4$ 0.1 M at v =100 mV/s.

V.2. Study of the corrosion inhibition of carbon steel X48 of hyb 1 and hyb 2 in 1M HCl medium

This part is devoted to the study of corrosion inhibition of carbon steel X48 by hyb1 and hyb 2 in 1 M HCl medium by varying the concentration and temperature. This study is carried out by electrochemical techniques such as potentiodynamic polarization and impedance spectroscopy. The thermodynamic parameters of the absorption process were determined from the absorption isotherms. To confirm the protective layer, we used atomic force microscopy (AFM).

V.2.1. Effect of the concentration of hyb 1 and hyb 2 on the electrochemical behavior of carbon steel X48 in HCl medium 1M

V.2.1.1. Polarization curves

The anodic and cathodic polarization curves of carbon steel X48 in HCl 1 M, in the absence and presence of different concentrations of hyb 1 and hyb 2 after 30 min of immersion and at ambient temperature (25°C) are shown in Figure V.6.

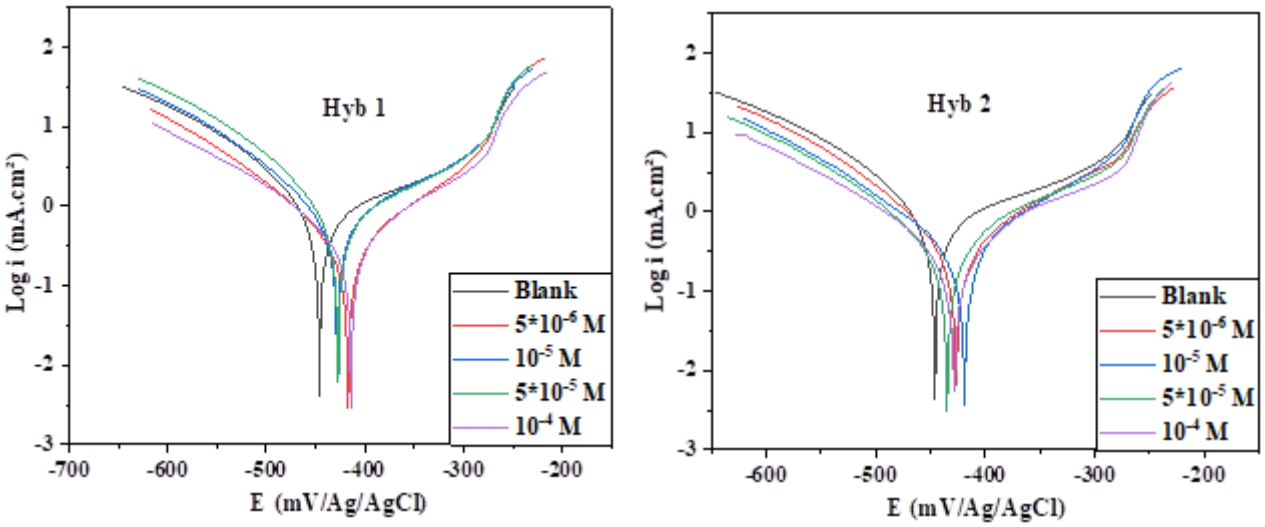

Figure V.6. Polarization curves for carbon steel X48 in 1 M HCl in the absence and presence of different concentrations of the compounds studied at T = 298 K.

Electrochemical parameters such as corrosion potential (E_{corr}), cathodic and anodic Tafel slopes (β_a, β_c), corrosion current density (i_{corr}) and inhibitory efficiency (EI_p (%)) are grouped in Table IV.4. The inhibitory efficacy (EI_p (%)) is calculated according to the following equation

$$EI_p(\%) = \frac{i^0_{corr} - i_{corr}}{i^0_{corr}} \times 100 \qquad \textbf{V.1}$$

With:

i^o_{corr} and i_{corr} represent the corrosion current density values obtained by extrapolating the anodic and cathodic Tafel lines, in the absence and presence of the inhibitor respectively, after 30 minutes of immersion in 1 M hydrochloric acid medium.

Table V.2. Electrochemical corrosion parameters of carbon steel X48 in 1 M HCl in the absence and presence of different concentrations of inhibitors.

Medium	C (M)	$-E_{corr}$ (mV/Ag/AgCl)	i_{corr} (mA/cm²)	β_a (mV.dec^{-1})	$-\beta_c$ (mV.dec^{-1})	EI_p (%)
Hyb 1	Blank	446	0.786	248.1	95.3	**
	$5*10^{-6}$	428.1	0.596	149	98	24.17
	10^{-5}	434.8	0.349	114.4	82.8	55.59
	$5*10^{-5}$	416.8	0.298	117.4	100.3	62.08
	10^{-4}	414.9	0.248	94.9	95.8	68.44
Hyb 2	Blank	446	0.786	248.1	95.3	**
	$5*10^{-6}$	436.2	0.374	138.8	109.8	52.41
	10^{-5}	418.7	0.371	124.4	118.8	52.79
	$5*10^{-5}$	426	0.301	110.7	85.3	61.70
	10^{-4}	429.2	0.287	121.9	115.8	63.48

According to the results obtained, it is noted that the addition of the two hybrids results in a decrease in corrosion rate and a shift of the corrosion potential to more positive values. This behavior can be attributed to the increase in the protective layer by adsorbed synthesized hybrids.

Both anodic and cathodic current branches are affected. This confirms the inhibitory action of the compounds studied. The cathodic and anodic polarisation curves are straight lines, indicating that the hydrogen reduction reaction at the steel surface takes place according to a pure activation mechanism:

$$2H^+ + 2e^- \rightarrow H_2$$

The action of the inhibitors results in a reduction in the anodic and cathodic currents. This result shows that the addition of inhibitors reduces the anodic dissolution of iron and delays the evolution of the H^+ ion discharge [1].

$$Fe \rightarrow Fe^{2+} + 2e^{-}$$

Corrosion current densities (i_{corr}) decrease as the concentration of inhibitors increases. The inhibitory efficacy of both hybrids increases with increasing concentration. The inhibition rates of hyb 1 and hyb 2 are 68.44 % and 63.48 % respectively at an optimal concentration of 10^{-4} M. Hyb1 and hyb2 have good inhibitory efficacy against corrosion of carbon steel X48 in HCl 1M medium. This is probably due to the presence of heteroatoms in both hybrids. The molecule contains heteroatoms like oxygen and nitrogen. The presence of free nitrogen and oxygen electron pairs in the inhibitors, which can form bonds with Fe^{2+} metallic sites [2-4], explains adsorption.

An inhibitor is considered to be classified as a cathodic or anodic inhibitor if the displacement of corrosion potential when the inhibitor is added is greater than 85 mV compared with the corrosion potential of the inhibitor-free steel [5]. The inhibitor is considered mixed if this displacement is less than 85 mV [6]. From the results grouped in table IV.2 we find that the variation of the value of the corrosion potential compared to the potential for white corrosion varies from 10 mV to 32 mV/Ag/AgCl. This confirms that hyb1 and hyb2 are mixed type inhibitors.

The analysis of the results obtained clearly shows that hyb1 and hyb2 compounds have good corrosion inhibitory properties of carbon steel X48 in medium HCl 1 M. This behavior is probably due to the good adsorption of the hyb1 and hyb2 compounds on the metal surface.

V.2.1.2. Electrochemical impedance spectroscopy

To further our study, we used the method of electrochemical impedance. The electrochemical impedance diagrams of corrosion of carbon steel X48 in the absence and presence of different concentrations of hyb1 and hyb2 are illustrated in Figure V.7

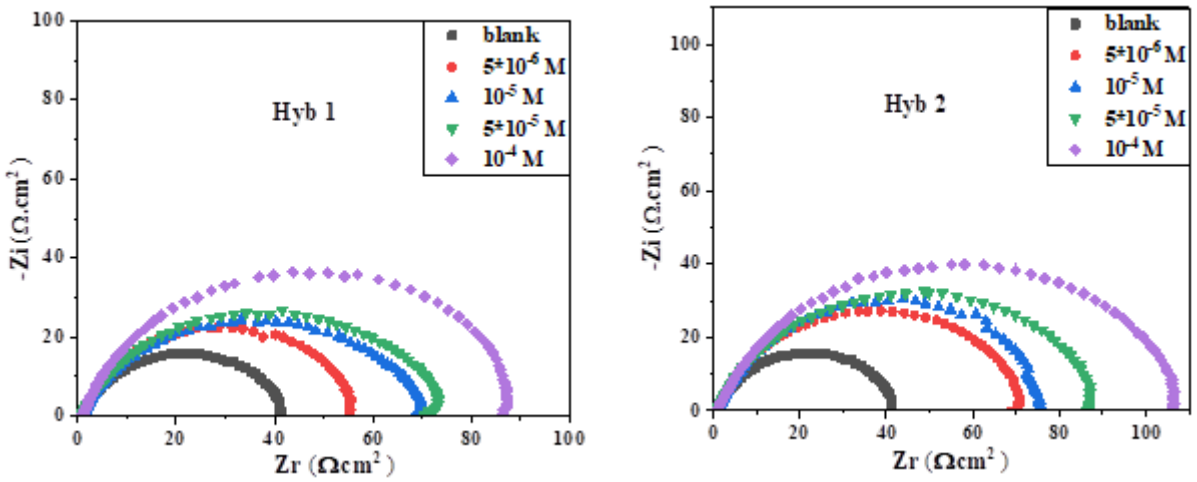

Figure V.7. Nyquist diagrams of carbon steel X48 steel in 1M HCl without and with the addition of different inhibitors concentrations at 298K.

We note that the Nyquist diagrams obtained are semicircular and that their diameters are affected by changes in the concentration of the compound studied. It can be seen that the diameter of the semicircle increases with increasing concentration. This confirms the adsorption of compound molecules on the surface of X48 carbon steel. These results show that the corrosion of X48 carbon steel 1 M HCl medium is controlled by the charge transfer process [7]. Nyquist diagrams show non-perfect semicircles, this is often due to frequency dispersion resulting from the inhomogeneity and roughness of the steel surface of the steel surface. We can notice that the addition of inhibitors does not change the profile of the Nyquist plots, which means that the inhibitor restrains metallic corrosion by increasing the polarization resistance instead of affecting the nature of the corrosion reaction [8].

The relationship below can be used to calculate the inhibitory efficiency (EI_z (%)) of X48 carbon steel from the charge transfer resistance (R_{ct}).

$$EI_z(\%) = \frac{R_{cti} - R_{ct0}}{R_{cti}} \times 100 \qquad \textbf{V.2}$$

with:

R_{ct0} and R_{cti} are the values of the charge transfer resistance of the steel after immersion in 1 M HCl in the absence of an inhibitor respectively.

The electrochemical parameters obtained by impedancemetry from the Nyquist diagrams are given in Table V.3.

Table V.3. Electrochemical impedance parameters relating to the corrosion of X48 carbon steel in 1 M HCl (T=298K) in the absence and presence of different concentrations of the inhibitors.

Medium	**Concentration (M)**	**R_s ($\Omega.cm^2$)**	**R_{ct} ($\Omega.cm^2$)**	**C_{dl} ($\mu F/cm^2$)**	**EI_z (%)**
Hyb 1	Blank	1.077	41.58	428.6	**
	$5*10^{-6}$	0.890	56.39	395.0	26.26
	10^{-5}	0.836	70.82	283.1	41.28
	$5*10^{-5}$	0.640	75.24	423.0	44.73
	10^{-4}	1.090	91.44	309.7	54.52
Hyb 2	Blank	1.077	41.58	428.6	**
	$5*10^{-6}$	0.797	72.47	614.8	42.62
	10^{-5}	1.106	77.14	206.3	46.09
	$5*10^{-5}$	0.828	90.28	352.5	53.94
	10^{-4}	0.979	109.50	325.4	62.02

Table V.3 shows that increasing the concentration leads to a decrease in the values of the double-layer capacitance (C_{dl}) and an increase in the charge transfer resistance (R_{ct}) and the inhibitory efficiency (EI_z). This is due to a decrease in corrosion rate when the protective film has adequate thickness and morphology. The increase in the values of R_{ct} and EI_z (%) indicates that the quantity of inhibitor molecules adsorbed on the metal surface of the steel has increased. These molecules form a protective layer on the surface of X48 carbon steel.

The decrease in the capacitance of the double layer can be attributed to the decrease in the local dielectric constant (ε) or the increase in the thickness of the double layer, resulting from the

adsorption of the molecule studied onto the metal surface [9] according to the expression of the double layer capacitance presented in the Helmotz model:

$$C_{dl} = \frac{\varepsilon_0 \varepsilon}{e}.S \qquad \textbf{V.3}$$

With:

S: Surface area of the electrode.

ε: Dielectric constant.

ε_0: Permittivity of the medium.

e: Thickness of the double layer.

Bode and phase angle curves for carbone steel X48 in 1 M HCl solution with and without inhibitors are displayed in Figure V.8. The absolute impedance Z increases at low frequencies. The rise of IE in larger concentrations is attributable to the adsorption of hybrid compounds (Hyb 1 and 2) on the steel surface. Furthermore, the negative shift in phase angle values indicates that the basic function of compounds is to provide a thin coating on the steel surface [10].

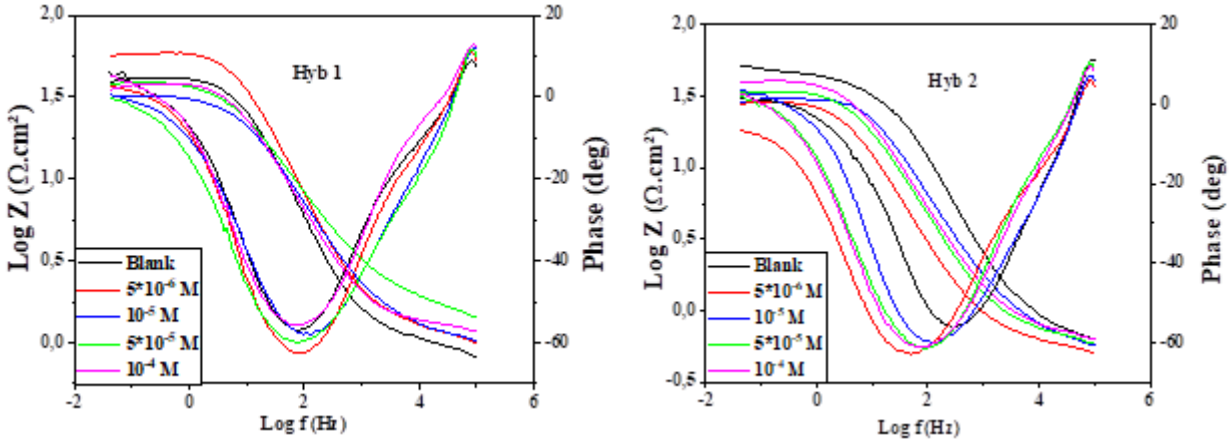

Figure V.8. Bode diagrams of XC48 steel in 1M HCl in the presence and absence of different concentrations of Hyb 1 and Hyb 2 at 293 K.

The equivalent circuit model shown in Figure V.9 was used to analyze the Nyquist curves. Nyquist curves. It consists of the double layer capacitance (C_{dl}), the charge transfer resistance (R_{ct}), and the solution resistance (R_s).

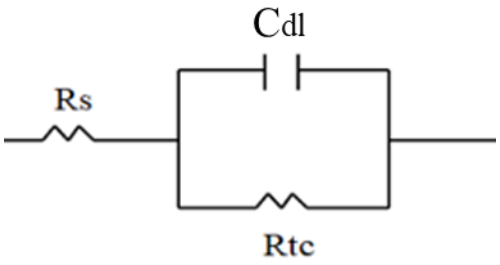

Figure V.9. Equivalent circuit used to analyze impedance spectra

The results obtained by impedance are in good agreement with those of potentiodynamic polarization.

V.2.1.3. Adsorption isotherms

The interaction between molecules with polar groups or atoms adsorbed on the cathodic or anodic sites of the metal surface plays an important role in the adsorption phenomenon.

To find the most significant adsorption isotherm, several types of Langmuir, Temkin, Frumkin, and Freundlich isotherms were tested to fit the recovery rate values ($\theta = EI\ (\%)/100$) to the standard isotherm. All these isotherm models were compared using the correlation coefficient R^2 [11]. The isotherms tested are represented by the following equations [12,13]:

Langmuir adsorption isotherm.

$$\frac{C_{inh}}{\theta} = \frac{1}{K} + C_{inh} \qquad \textbf{V.4}$$

Temkin adsorption isotherm.

$$Exp(-2a\theta) = KC_{inh} \qquad \textbf{V.5}$$

Frumkin adsorption isotherm.

$$\left(\frac{\theta}{1-\theta}\right) Exp(-2a\theta) = KC_{inh} \qquad \textbf{V.6}$$

Freundlich isotherm

$$\theta = K_{ads} C_{inh}^{n} \quad 0 \prec n \prec 1 \ . \qquad \textbf{V.7}$$

with:

K: Equilibrium constant.

θ: Recovery rate.

n: Degree of non-linearity between θ and C_{inh}.

C_{inh}: Inhibitor concentration.

a: Interaction constant between adsorbed particles

Figures V.10-13 represent the different adsorption isotherms Langmuir, Temkin, Frumkin and Freundlich obtained by plotting polarization curves and impedance diagrams.

The C_{inh}/θ curve for hyb1 and hyb2 are linear with correlation coefficient values between 0.9 and 1 for both methods. We find that the best fit is obtained with the Langmuir isotherm. This shows that the adsorption of hyb1 and hyb2 on the surface of X48 carbon steel in 1 M hydrochloric acid medium obeys the Langmuir adsorption isotherm. This model assumes that the surface of the shelf contains adsorption sites and that each site contains an adsorbed molecule [11].

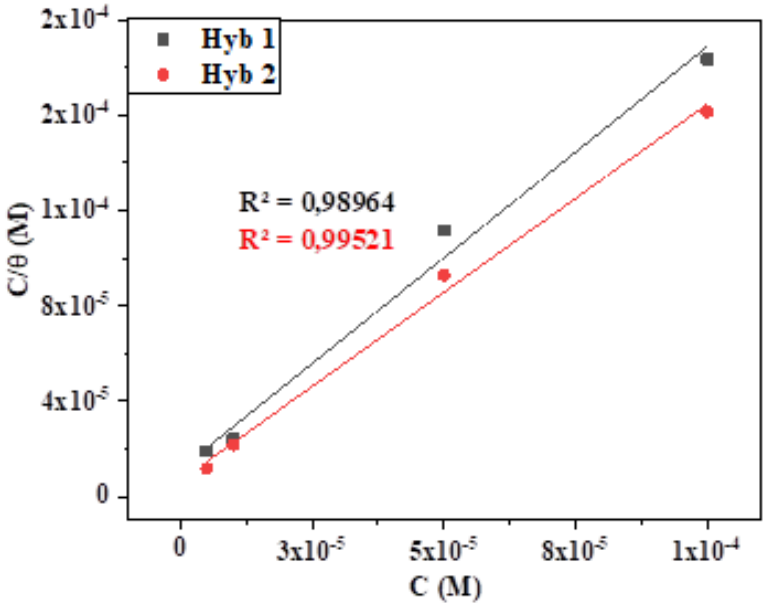

Figure V.10. Langmuir adsorption isotherm for X48 carbon steel in 1 M HCl in the presence of inhibitors for the two methods.

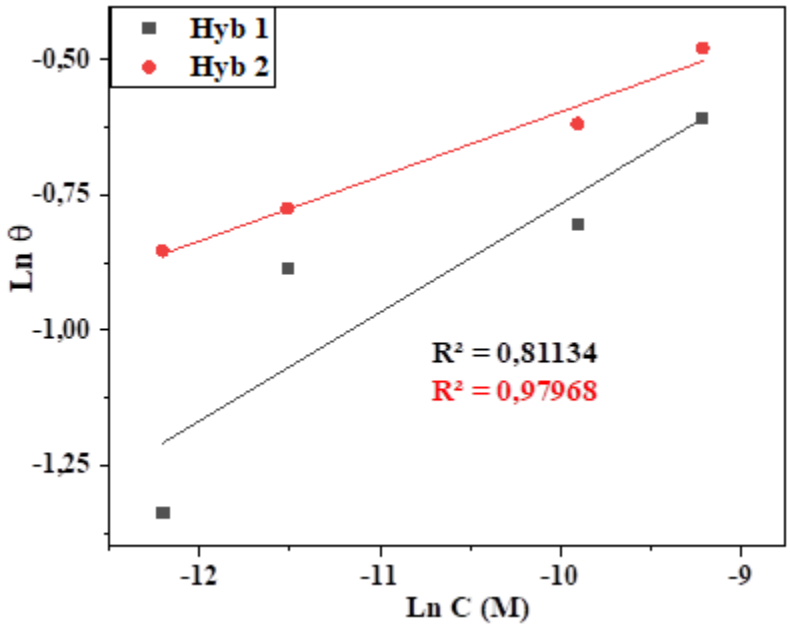

Figure V.11. Freundlich adsorption isotherm for X48 carbon steel in 1 M HCl in the presence of inhibitors for the two methods.

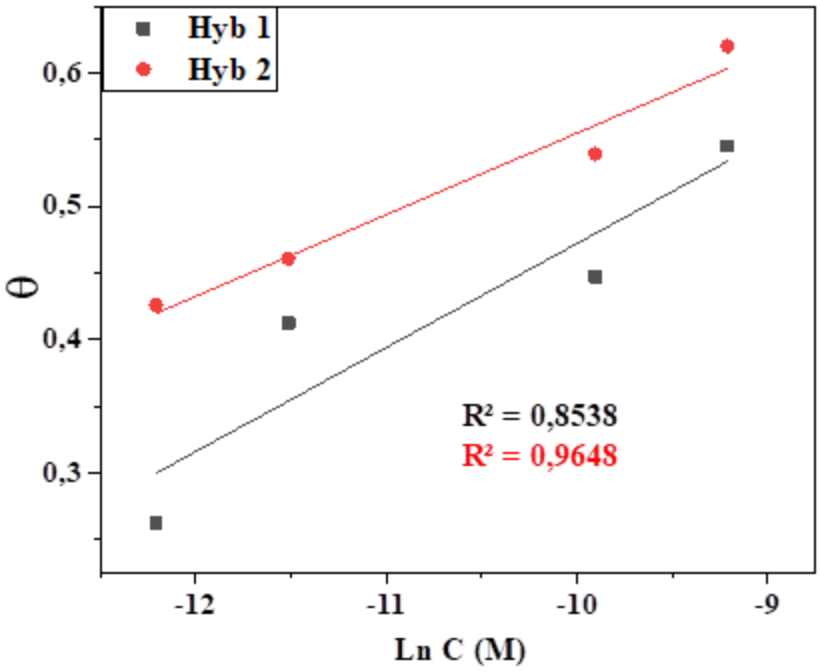

Figure V.12. Temkin adsorption isotherm for X48 carbon steel 1 M HCl in the presence of inhibitors for the two methods.

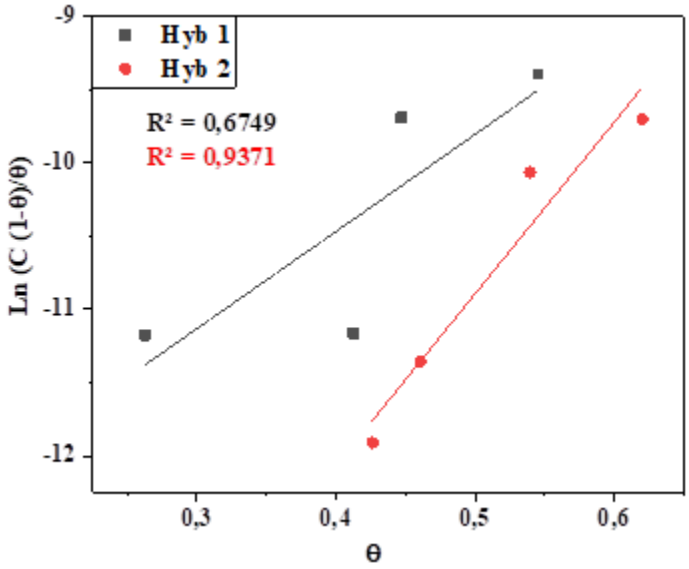

Figure V.13. Frumkin adsorption isotherm for X48 carbon steel in 1M HCl in the presence of inhibitors for the two methods.

Table V.4 summarizes the values of the adsorption constant (K_{ads}) and standard free energy (ΔG_{ads}) calculated from the Langmuir isotherm. According to the following equation, the adsorption constant K_{ads} is related to the standard free energy ($\Delta G°_{ads}$).

$$K_{ads} = \frac{1}{55.55} Exp\left(\frac{-\Delta G°_{ads}}{RT}\right) \qquad \textbf{V.8}$$

Table V.4 Thermodynamic parameters of adsorption of Hyb 1 and Hyb 2 on carbon steel X48 in HCl 1 M

Medium	K_{ads} 10^{-4} (M^{-1})	ΔG° (kJ/mol.K)
HCl	***	***
Hyb 1	8.65	- 38
Hyb 2	1.48	- 39.43

K_{ads} values are characteristic of the strong adsorption of the inhibitor on the steel surface and high negative values of standard free adsorption energy ($\Delta G°_{ads}$) are attributed to strong, spontaneous interactions between the inhibiting molecules and the metal surface [14].

According to the literature, the value of $\Delta G°_{ads}$ close to -20 kJ/mol means an electrostatic reaction between the charged species and the steel surface (physisorption). Suppose the value of

$\Delta G°_{ads}$ is close to -40 kJ/mol. This shows a charge transfer between the inhibitory molecules and the metal surface by forming either covalent or coordination bonds (chemisorption) [15].

In our study, free energy standard of adsorption hybrids ranges from -38 to -39.43 kJ/mol, depending on the two techniques employed. This suggests that the products exhibit mixed adsorption, or chemisorption and physisorption. Chemical adsorption is more significant than physical adsorption because the values of Δ Gads are near -40 KJ/mol [16].

V.2.2. Effect of temperature in 1 M HCl medium on the inhibitor

The aim of this study is to test the effect of temperature on hyb1 and hyb2 inhibitory efficiency by the two electrochemical techniques, namely potentiodynamic polarization and impedance spectroscopy. We have undertaken a study in varying the temperature from 298 to 328 K in HCl 1M in the absence and presence of 10^{-4} M of the inhibitors and determining the thermodynamic parameters.

V.2.2.1. Polarization curves

Figure V.14 shows the polarisation curves for X48 carbon steel in 1 M HCl in the absence and presence of the inhibitors at the optimum concentration of 10^{-4} M and at different temperatures from 298 to 328 K after 30 minutes' immersion time.

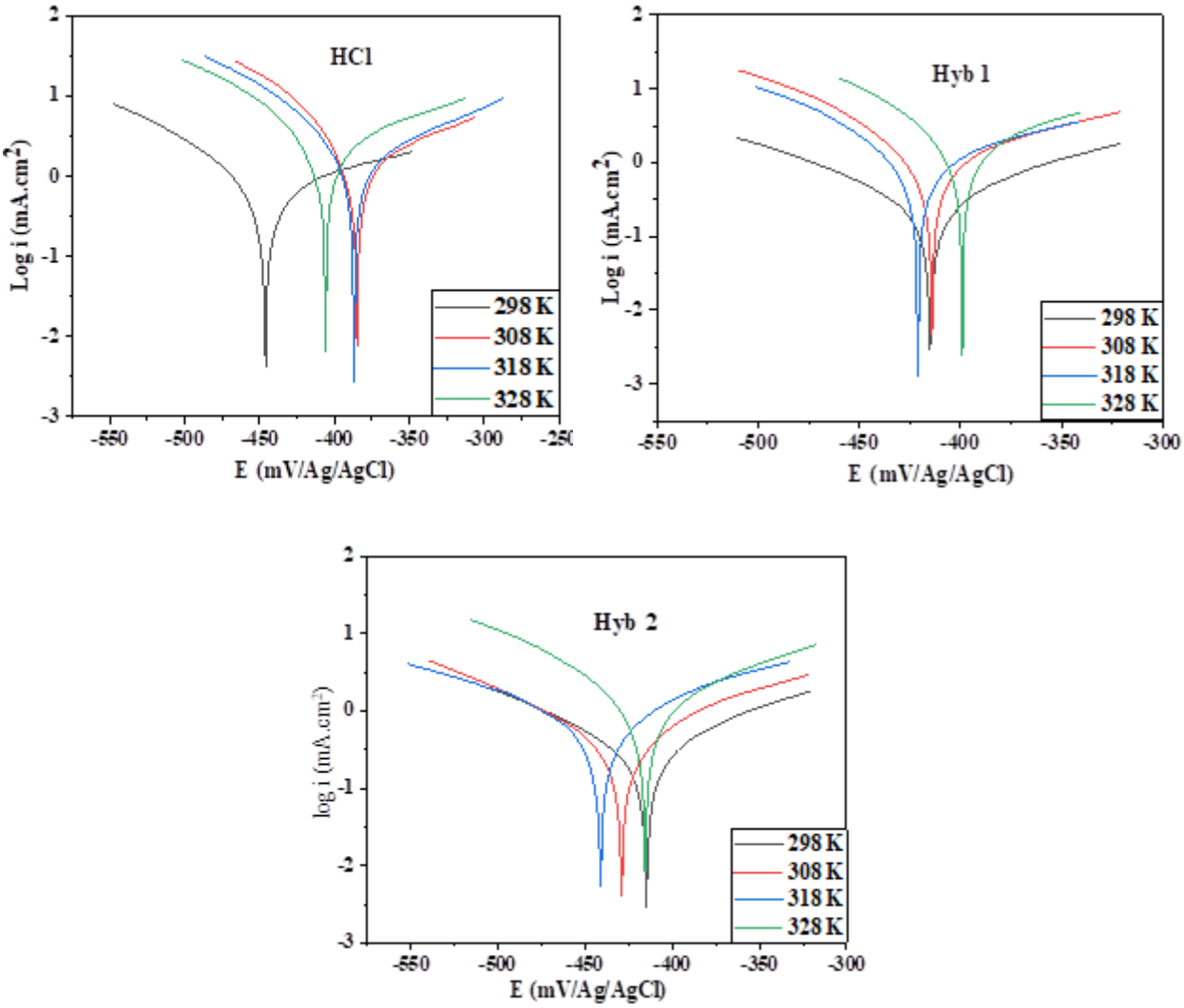

Figure V.14. Polarisation curves for carbon steel X48 in 1 M HCl in the absence and presence of the inhibitors at different temperatures.

The values of the inhibitory efficiencies and the electrochemical parameters associated with the corrosion of steel in 1M HCl in the absence and presence of 10^{-4} M of the inhibitors and at different temperatures are given in Table V.5.

Table V.5. The inhibitory efficiencies and the electrochemical parameters associated with steel corrosion in 1M HCl in the absence and presence of 10^{-4} M of the inhibitors and at different temperatures.

Medium	T (K)	$-E_{corr}$ (mV/Ag/AgCl)	i_{corr} (mA/cm²)	β_a (mV.dec^{-1})	$-\beta_c$ (mV.dec^{-1})	EI_p (%)
HCl	298	446	0.786	248.1	95.3	**
	308	358.1	1.118	101.6	43.8	**
	318	387	1.588	133.8	63.5	**
	328	406.1	2.392	157.9	78.6	**
Hyb 1	298	414.9	0.248	94.9	95.8	68.44
	308	414.1	1.118	143	69.2	29.59
	318	421	0.798	106.5	61.0	28.62
	328	399	1.778	127.7	65.7	25.66
Hyb 2	298	429.2	0.287	121.9	115.8	63.48
	308	428.1	0.496	106.9	102.5	55.63
	318	441.2	0.57	71.9	78.3	49.96
	328	414.9	1.306	131.1	87.6	45.40

We find that the current densities increase with increasing temperature. The corrosion potential (E_{corr}) moves to negative values for two hybrids hyb1 and hyb2 while it moves to positive values for HCl. We also note that the anodic and cathodic Tafel slopes (β_a and β_c) vary with temperature. The cathodic and anodic Tafel branches show the same mechanism for proton reduction at the steel surface and steel dissolution. These results corroborate those in the literature [14]. The inhibitory effectiveness of the product decreases with increasing temperature [18-20]. The structures of both hybrids are efficient because of the presence of the nitrogen atom and oxygen.

V.2.2.2. Electrochemical impedance spectroscopy

Figure V.15 shows the Nyquist impedance diagrams obtained for X48 carbon steel in HCl 1 M in the absence and presence of 10^{-4} M of hyb1 and hyb2 at different temperatures. These diagrams refer to capacitive loops, their sizes decreasing with the increase of temperature.

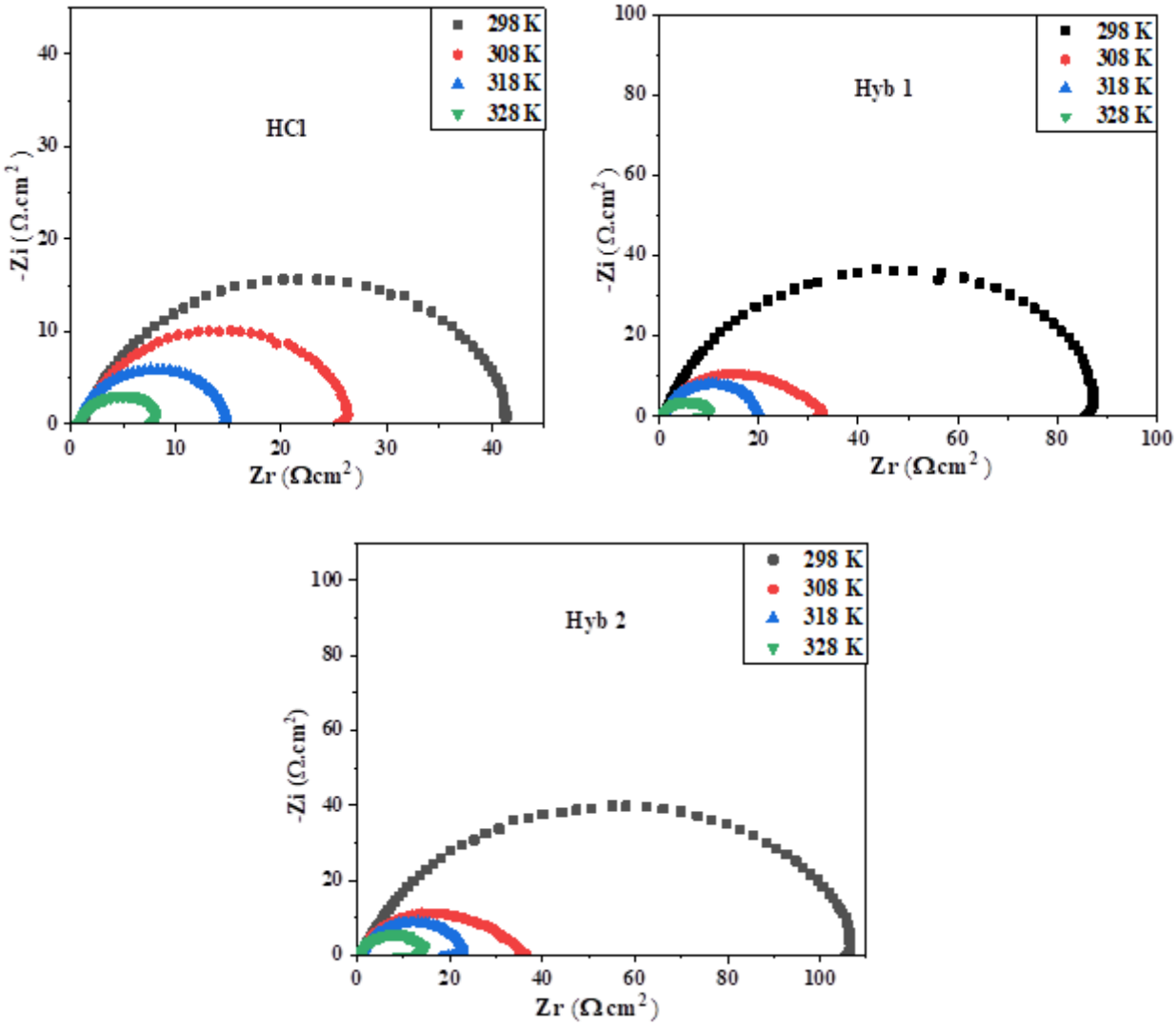

Figure V.15. Nyquist impedance diagrams obtained for carbon steel X48 in 1 M HCl in the absence and presence of 10^{-4} M of the hybrid at different temperatures.

TableV.6 shows the electrochemical parameters and inhibitory efficiency (EI_z) obtained by EIS of corrosion of carbon steel X48 in HCl 1 M in the absence and presence of 10^{-4} M of hyb1 and hyb 2 at different temperatures.

Table V.6. Electrochemical parameters and corrosion inhibiting efficacy of X48 carbon steel in 1 M HCl in the absence and presence of 10^{-4} M of the hybrid at different temperatures.

Medium	T (K)	R_s (Ω.cm²)	R_{ct} (Ω.cm²)	C_{dl} (µF/cm²)	EI_Z (%)
HCl	298	1.077	41.58	428.6	**
	308	0.822	26.58	670.4	**
	318	0.734	14.38	349.5	**
	328	0.881	7.64	370.4	**
Hyb 1	298	1.090	91.44	309.7	54.52
	308	0.912	19.37	205.3	25.73
	318	0.756	09.51	334.4	19.66
	328	0.781	31.76	178.3	16.30
Hyb 2	298	0.979	109.50	325.4	62.02
	308	0.837	14.19	125.5	46.15
	318	0.749	23.15	137.4	37.88
	328	0.553	31.82	125.0	16.46

According to the results obtained, we find that the charge transfer resistance decreases with increasing temperature. The values of the charge transfer resistances of both hybrids are higher than those of HCl. The inhibitory efficacy of both hybrids decreases with increasing temperature

V.2.2.3. Determination of activation energies

The corrosion process's activation parameters at different temperatures, in the absence and presence of 10^{-4} M inhibitor, are calculated. The activation energy (E_a) is determined from the polarisation curves using Arrhenius law [21].

$$i_{corr} = \frac{RT}{Nh}\exp(-\frac{\Delta Sa^{o}}{RT}) \qquad \textbf{V.9}$$

The activation enthalpy (ΔH_a) and activation entropy (ΔS_a) were determined from the alternative formula of the following Arrhenius equation [22]:

$$i_{corr} = \frac{RT}{Nh}\exp(\frac{\Delta Sa^{o}}{R})\exp(-\frac{\Delta H_{a}}{RT}) \qquad \textbf{V.10}$$

with:

i_{corr}: Corrosion current density.

K: Arrhenius constant.

R: Gas constant (8.314 $J \cdot mol^{-1} \cdot K^{-1}$).

T: Temperature.

N: Avogadro number.

h: Plank constant.

The variation of the corrosion current density logarithm as a function of the reciprocal of the absolute temperature is a straight line in the absence and presence of the inhibitor (Figure V.16). The activation energy is determined by linear regression.

To determine the values of ΔH_a and ΔS_a, we plotted the variation of ln (i_{corr}/T) as a function of the reciprocal of the temperature, this is a straight line with a slope equal to - $\Delta H°_a/R$ and a y-intercept equal to ln R/Nh +$\Delta S°_a/R$ (Figure V.17).

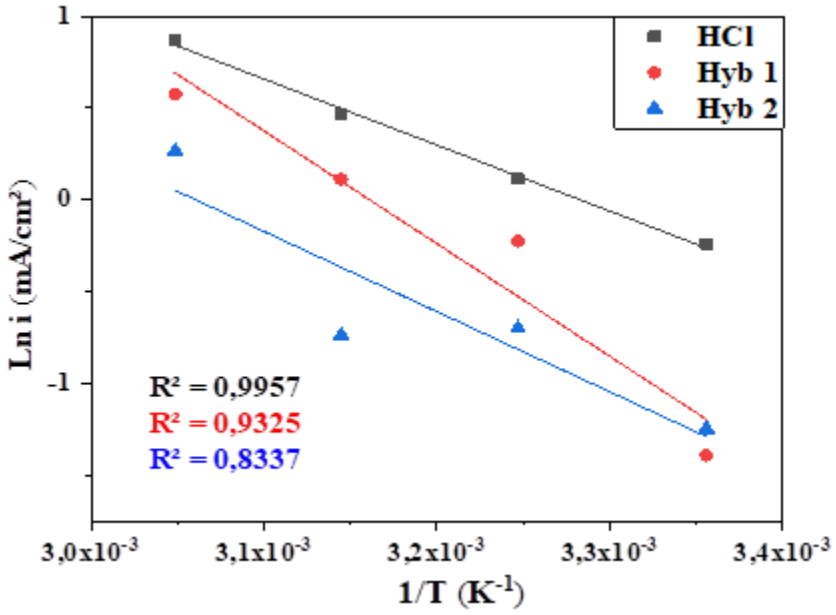

Figure V.16. Arrhenius diagrams in the absence and presence of 10^{-4} M inhibitor in 1 M HCl at different temperatures.

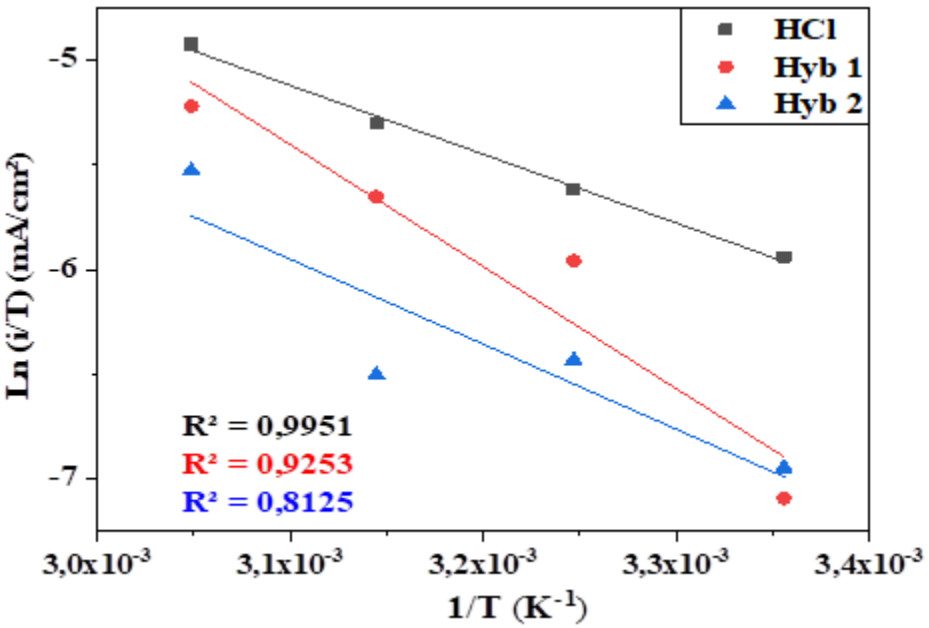

Figure V.17. Plots of ln (i_{corr}/T) versus 1/T in the absence and presence of 10^{-4} M inhibitor in 1 M HCl at different temperatures.

The values of activation energies (E_a), activation enthalpies (ΔH_a), and activation entropies (ΔS_a) are given in Table V.7.

Table V.7. Thermodynamic characteristics of the inhibitor on the surface of X48 carbon steel.

Medium	E_a (kJ/mol)	ΔH_a (kJ/mol)	ΔS_a (J/mol.K)
HCl	29.92	27.32	-174.44
Hyb 1	51.031	48.5	-111.13
Hyb 2	36.35	33.75	-161.5

According to Radovic's theory [23], we can see that:

- ✓ If E_a(inh) > E_a(HCl) the molecules adsorb on the surface by weak bonds (physisorption) sensitive to temperature.
- ✓ If E_a(inh) < E_a(HCl) the molecules are adsorbed on the surface by strong bonds (chemisorption) which increase the protection of the metal against corrosion and become stronger with increasing temperature.

- ✓ If $E_a(inh) = E_a(HCl)$ the compounds show no protective power with increasing temperature.

The activation energy of the inhibitor is greater than that of hydrochloric acid. This is attributed to physisorption of the molecule on the steel surface [24].

The positive enthalpy of activation values (ΔH_a) confirms that the dissolution of carbon steel X48 is endothermic [18].

The negative value of the entropy of activation (ΔS_a) for the compound confirms that there is a decrease in disorder and the transformation of the reactants into an activated fer molecule complex in solution [25].

V.2.3. Atomic force microscopy (AFM)

The surface of the polished steel appears rather uniform with only tiny scratches [23], whereas after 24 h immersion in the 1 M HCl solution, the surface of the steel appears rough, badly damaged, and severely corroded. Surface roughness is one of the most important topographical parameters that can be derived from the analysis of information obtained by AFM [26-30]. It can be seen visually that in the presence of the inhibitors Hyb 1 and Hyb 2, the surfaces are less rigorous, the values of the peak to valley are 0.254, 0.03 and 0.284 µm, while the RMS values are 0.726, 0.369 and 0.330 µm for the pieces without and with Hyb 1and Hyb 2 inhibitors respectively. These findings indicate that the Hyb 2 inhibitor is better than the Hyb 1 inhibitor.

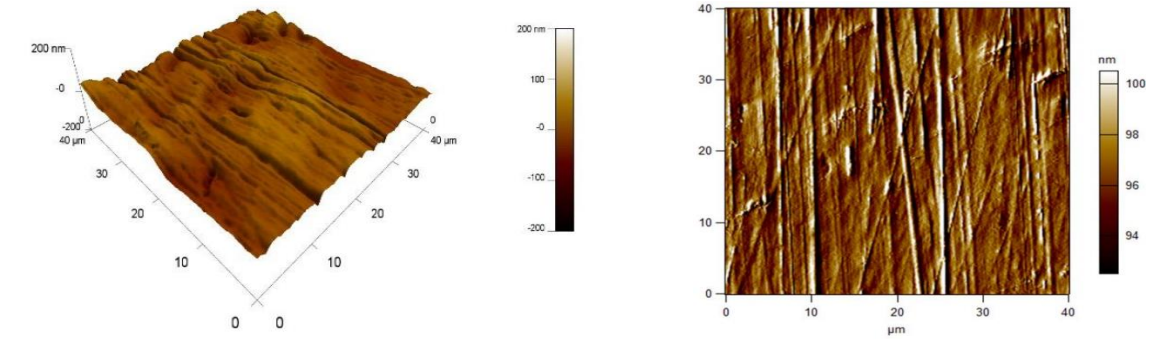

steel alone

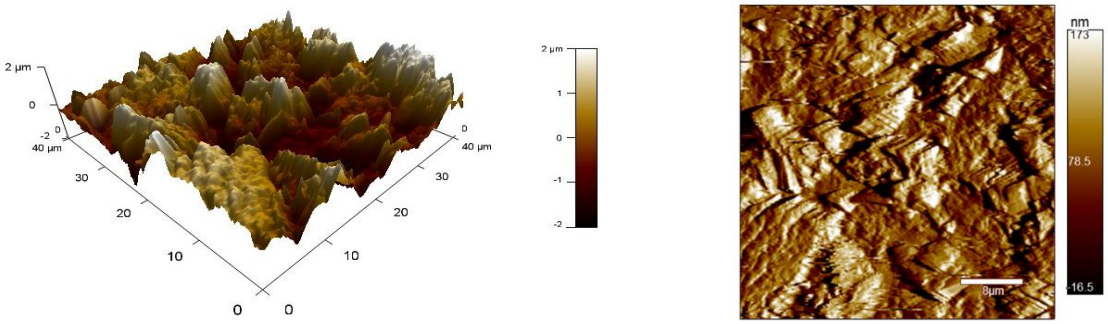

Without inhibitor (HCl)

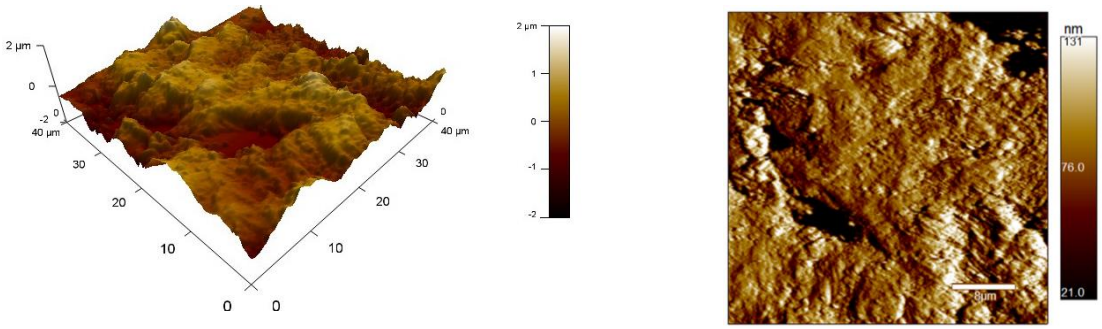

With (Hyb 1)

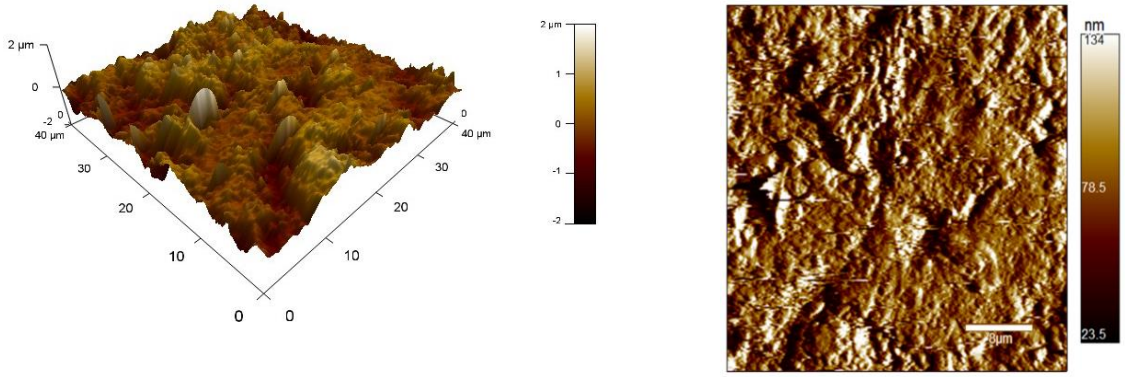

With (Hyb 2)

Figure V.18. AFM results with and without the presence of the inhibitors.

References

[1] M.A. Hegazy, A novel Schiff base-based cationic gemini surfactants: synthesis and effect on corrosion inhibition of carbon steel in hydrochloric acid solution. Corros. Sci. 51(11) (2009) 2610-2618.

[2] R. Kooliyat, J.T. Kakkassery, V. P. Raphael, S.V. Cheruvathur, B.M. Paulson, synthesis, cyclic voltammetric, electrochemical, and gravimetric corrosion inhibition investigations of schiff base derived from 5, 5-dimethyl-1, 3-cyclohexanedione and 2-aminophenol on mild steel in 1M HCl and 0.5M H_2SO_4. Int. J. Electrochem. 2019 (2019) 1-13.

[3] M.M. Elajaily, F.I. Abdullah, R.A. Akasha, Synthesis, characterization, and corrosion inhibition of cobalt (II) azo Schiff base chelate. J. Chem. Pharm. Res. 5(12) (2013) 1144-1151.

[4] Y. Qiang, S. Zhang, L. Guo, X. Zheng, B. Xiang,S. Chen, Experimental and theoretical studies of four allyl imidazolium-based ionic liquids as green inhibitors for copper corrosion in sulfuric acid. Corros. Sci. 119 (2017) 68-78.

[5] R.K. Mehta, S.K. Gupta, M. Yadav, Studies on pyrimidine derivative as green corrosion inhibitor in acidic environment: Electrochemical and computational approach. J. Environ. Chem. Eng. 10 (2022) 108499.

[6] A. Singh, V.K. Singh, M.A. Quraishi, Inhibition of Mild Steel Corrosion in HCl Solution Using Pipali (Piper longum) Fruit Extract. Arab. J. Sci. Eng. 38 (2013) 85-97.

[7] K. Zakaria, M.A. Abbas, M.A. Dedair, Herbal expired drug bearing glycosides and polysaccharides moieties as green and cost-effective oilfield corrosion inhibitor: Electrochemical and computational studies. J. Mol. Liq. 352 (2022) 118689.

[8] M.A. Mostafa, A.M. Ashmawy, M.A. Reheim, M.A. Bedair, A.M. Abuelela, Molecular structure aspects and molecular reactivity of some triazole derivatives for corrosion inhibition of aluminum in 1 M HCl solution. J. Mol. Struct. 1236 (2021) 130292.

[9] X. Wang, H. Yang, F. Wang, An investigation of benzimidazole derivative as corrosion inhibitor for mild steel in different concentration HCl solutions. Corros. Sci. 53 (2011) 113-121.

[10] X. Ma, J. Wang, J. Xu, J. Jing, J. Li, H. Zhu, Z. Hu, Sunflower head pectin with different molecular weights as promising green corrosion inhibitors of carbon steel in hydrochloric acid solution. Acs Omega. 4(25) (2019) 21148-21160.

[11] H. Elmsellem, A. Aouniti, Y. H. ToubiSteli, M. Elazzouzi, S. Radi, Y. El, Inhibition of mild steel corrosion in hydrochloric acid solution by new synthesized Schiff Base. Der Pharma Chem. 7 (7) (2015) 353-364.

[12] E. A. Noor, A. H. Al-Moubaraki, Thermodynamic study of metal corrosion and inhibitor adsorption processes in mild steel/1-methyl-4 [4′(-X)-styryl pyridinium iodides/hydrochloric acid systems. Materials Chemistry and Physics, 110(1) (2008) 145-154.

[13] A. Dehghani, G. Bahlakeh, B. Ramezanzadeh, M. A Ramezanzadeh, Combined experimental and theoretical study of green corrosion inhibition of mild steel in HCl solution by aqueous Citrullus lanatus fruit (CLF) extract. J. Mol. Liq. 279 (2019) 603-624.

[14] O. Olivares-Xometl, E. Álvarez-Álvarez, N.V. Likhanova, I.V. Lijanova, R.E. Hernández-Ramírez, P. Arellanes-Lozada, J.L. Varela-Caselis; J. Adhes. Sci. Tech. 32 (10) (2018) 1092-1113.

[15] S.A. Soliman, M.S. Metwally, S.R. Selim, M.A. Bedair, M. A. Abbas, Corrosion inhibition and adsorption behavior of new Schiff base surfactant on steel in acidic environment: Experimental and theoretical studies. J. Ind. Eng. Chem. 20 (6) (2014) 4311 -4320.

[16] S. Mouzali, D. Haffar, L. Bouzidi, Z. Bouanane, Saida, M., Djahida, H., Leila, B., & Zohra, B. (2017). Synthesis, characterization and inhibition effect of a new schiff base (E)-3-(((2-amino-4-methylphenyl) imino) methyl) naphthalen-2-ol on the corrosion of carbon steel X48 in acidic medium, Int. J. Electrochem. Sci. 12 (2017) 11042-11063.

[17] N. Zulfareen, K. Kannan, T. Venugopal, S. Gnanavel, Synthesis, characterization and corrosion inhibition efficiency of N-(4-(Morpholinomethyl Carbamoyl Phenyl) Furan-2-Carboxamide for brass in HCl medium. Arab. J. Chem. 9(1) (2016) 121-135.

[18] F. Boudjellal, H. B. Ouici, A. Guendouzi, O. Benali, A. Sehmi, Experimental and theoretical approach to the corrosion inhibition of mild steel in acid medium by a newly synthesized pyrazole carbothioamide heterocycle. J. Mol. Struc, 1199 (2020) 127051.

[19] S. Shahabi, S. Hamidi, J. B. Ghasemi, P. Norouzi, A. Shakeri, Synthesis, experimental, quantum chemical and molecular dynamics study of carbon steel corrosion inhibition effect of two Schiff bases in HCl solution. J. Mol. Liq. 285 (2019) 626-639.

[20] G. Khan, W. J. Basirun, S. N. Kazi, P. Ahmed, L. Magaji, S. M. Ahmed, A. B. B. M. Badry, Electrochemical investigation on the corrosion inhibition of mild steel by Quinazoline Schiff base compounds in hydrochloric acid solution J. Colloid. Interface. Sci.502 (2017) 134-145.

[21] T. A. Salman, A. A. Al-Amiery, L. M. Shaker, A. Kadhum, M. S. Takriff, A study on the inhibition of mild steel corrosion in hydrochloric acid environment by 4-methyl-2-(pyridin-3-yl) thiazole-5-carbohydrazide. Int. J. Corros. Scale Inhib, 8(4) (2019) 1035.

[22] M. Barrahi, H. Elhartiti, A. El Mostaphi, N. Chahboun, M. Saadouni, R. Salghi, M. Ouhssine, Corrosion inhibition of mild steel by Fennel seeds (Foeniculum vulgare Mill) essential oil in 1M hydrochloric acid solution. Int. J. Corros. Scale Inhib., 8(4) (2019) 937-953.

[23] O. Radovici; Proceedings of the 2nd European Symposium on Corrosion Inhibitors, Ferrara. (1965).

[24] P. R. Ammal, M. Prajila, A. Joseph, Effective inhibition of mild steel corrosion in hydrochloric acid using EBIMOT, a 1, 3, 4-oxadiazole derivative bearing a 2-ethylbenzimidazole moiety: Electro analytical, computational and kinetic studies. Egypt. J. Pet. 27(4) (2018) 823-833.

[25] D. K. Lavanya, F. V. Priya, D. P. Vijaya, Green Approach to Corrosion Inhibition of Mild Steel in Hydrochloric Acid by 1-[Morpholin-4-yl (thiophen-2-yl) methyl] thiourea. . Fail. Anal. Prev. 20 (2020) 494-502.

[26] D. Wang, B. Xiang, Y. Liang, S. Song, C. Liu, Corrosion control of copper in 3.5 wt.% NaCl solution by domperidone: experimental and theoretical study. Corros. Sci. 85 (2014) 77-86.

[27] E. Barrera, M. P. Pardavé, I. González, Formation mechanisms and characterization of black and white cobalt electrodeposition onto stainless steel. J. Electrochem. Soc. 147(5) (2000) 1787.

[28] N. M. Martyak, R. Seefeldt, Additive-effects during plating in acid tin methanesulfonate electrolytes. Electrochim. Acta, 49(25) (2004) 4303-4311.

[29] J. R. Smith, S. Breakspear, S. A. Campbell, AFM in surface finishing: Part I. An introduction. Transactions of the IMF, Journal 81(2), (2003) 26-29.

[30] R. Sekar, C. Eagammai, S. Jayakrishnan, Effect of additives on electrodeposition of tin and its structural and corrosion behavior. J. Appl. Electrochem. 40 (2010) 49-57.

General Conclusion

General Conclusion

In this work of this thesis, two new organic–inorganic ionic materials named tris (2,4,6-triamino-1,3,5-triazinium) monodrogenphosphate dihydrogenphosphate tetrahydrate ($3C_3H_7N_6^+.HPO_4^{2-}.H_2PO_4^-.4H_2O$) and tris (2,4,6-triamino-1,3,5-triazinium) perchlorate monohydrate ($C_3H_7N_6^+.ClO_4^-.H_2O$) as a single crystal have been synthesized and their molecular structures and 3D supramolecular network were affined and discussed via single crystal X-ray diffraction and Hirshfeld surface analysis. The complex of Cu (II) with $C_3H_7N_6^+.ClO_4^-.H_2O$ was also synthesized and all the compounds were characterized by FT-IR, and UV-Vis spectroscopy. In addition, the thermal behavior was effectuated by TGA/DTG.

The UV-Vis absorption spectra of these hybrid materials reveal that they are transparent in the visible region, and have a good optical transmittance in the entire visible and visible domain, and it is characterized by strong absorption in ultraviolet germicidal with an absorption threshold at 235 nm and 255 nm respectively, these low values are sufficient for laser doubling frequency and other related opto-electronic applications in ultraviolet domain. Whereas the UV-Visible spectrum of the copper complex has an absorption band at 430 nm which confirms its formation.

Moreover, the FT-IR spectra show the vibration modes and correlated to the functional groups of these hybrid materials single crystal, were studied based on crystallographic analysis structures, coherent and provide spectroscopic evidence for the crystal formation, which an accordance was found between the FTIR-spectroscopy and XRD data. The appearance, disappearance and displacement of peaks in the infrared spectrum of the copper complex confirms its formation.

In addition, the thermal behavior of these compounds divulges that they have a good thermal stability and offers better thermal stability than pure melamine which makes them suitable for thermal applications. This helps in polymer processing steps and this enables the suitability of the crystal, can be used to predict the useful product lifetimes of some polymeric materials, such as the coatings for electrical or telecommunication cables. Organic–inorganic ionic materials based on melamine are very promising light emitting materials due to their good thermal stability. Further research has to be carried out and can be extended to several industrial and research applications.

The electrochemical study by cyclic voltammetry of tris (2,4,6-triamino-1,3,5-triazinium) perchlorate monohydrate shows that it reduces in a single step.

The inhibitory efficacy of both hybrid against corrosion of carbon X48 steel in HCl 1 M was examined by the use of potentiodynamic polarization and electrochemical impedance spectroscopy. The results show that the inhibitory efficacy increases with the increasing concentration of hybrid. The two hybrids are mixed type inhibitors.

The inhibitory efficacy of both compounds decreases with increasing temperature.

The calculated ΔG^{o}_{ads} values indicate that these hybrids are chemisorbed on the metal surface and the adsorption process follows the Langmuir isotherm.

Thermodynamic characteristics such as $\Delta G°_{ads}$, $\Delta E°_{a}$ and K_{ads} confirmed that both hybrids are effectively adsorbed to the steel surface.

AFM analysis confirms the adsorption of the two hybrids studied on the surface of carbon steel X48 in chlorhydric acid 1M. This is due to the interactions between the inhibitory molecules and iron forming a protective layer on steel.

The results obtained from the two electrochemical techniques used corroborate.

The compounds tris(melaminium) monodrogenphosphate dihydrogenphosphate tetrahydrate and 2,4,6-triamino-1,3,5-triazinium perchlorate monohydrate are promoters for reducing corrosion phenomena in industry.

Abstract
In this work, two new single-crystals hybrid ionic materials tris(2,4,6-triamino-1,3,5-triazinium) monodrogenphosphate dihydrogenphosphate tetrahydrate ($3C_3H_7N_6^+.HPO_4^{2-}.H_2PO_4^-.4H_2O$) and 2,4,6-triamino-1,3,5-triazinium perchlorate monohydrate ($C_3H_8\ N_6^+.ClO_4^-.H_2O$) were synthesized, their structures were affined by single-crystal X-ray diffraction the 3D-supramolecular structure has been investigated basing on the SXRD data. Moreover, UV-visible and FT-IR spectroscopy have been used to establish optical and vibrational properties. The study of the thermal decomposition of these hybrid materials was also occurred by TGA/DTG techniques. These hybrids were examined as corrosion inhibitors using electrochemical methods. The electrochemical properties were studied by cyclic voltammetry. These inhibitors are effectively adsorbed by a chemisorption process to the steel surface. The adsorption of these compounds follows the Langmuir isotherm in the studied medium. The results show that these compounds have good reactivity and high inhibition efficiency.
Keywords: Hybrid ionic material, Melamine, Thermal stability, Corrosion inhibitor, Steel

الملخص
في هذا العمل، تم تصنيع مادتين أيونيتين هجينتين أحاديتي البلورات جديدتين هما ثلاثي (2،4،6-ثلاثي أمينو-1،3،5-ثلاثي آزينيوم) أحادي فوسفات ثنائي هيدروجين رباعي الهيدرات $3C_3H_7N_6^+.HPO_4^{2-}.H_2PO_4^-.4H_2O$ وبيركلورات ثلاثي أمينو-1،3،5-ثلاثي آزينيوم أحادي الهيدرات($C_3H_8\ N_6^+.ClO_4^-.H_2O$) ، وتم تحديد بنيتهما بواسطة الأشعة السينية أحادية البلورة، وتم التحقيق في البنية الفوق جزيئية ثلاثية الأبعاد بناءً على بيانات SXRD. علاوة على ذلك، تم استخدام الأشعة فوق البنفسجية والمرئية وتحت الحمراء لتحديد الخصائص البصرية والاهتزازية. كما تم دراسة التحلل الحراري لهذه المواد الهجينة بواسطة تقنيات TGA/DTG. وتم فحص هذه المواد الهجينة كمثبطات للتآكل باستخدام الطرق الكهروكيميائية. تمت دراسة الخواص الكهروكيميائية باستخدام الفولتميتر الدوري. يتم امتصاص هذه المثبطات بشكل فعال عن طريق عملية الامتصاص الكيميائي على سطح الفولاذ. يتبع امتصاص هذه المركبات منحنى لانجمويير في الوسط المدروس. تظهر النتائج أن هذه المركبات لها تفاعلية جيدة وكفاءة تثبيط عالية.
الكلمات المفتاحية: مادة أيونية هجينة، الميلامين، الاستقرار الحراري، مثبط التآكل، الفولاذ

Résumé
Dans ce travail, deux nouveaux matériaux ioniques hybrides monocristaux, le tris(2,4,6-triamino-1,3,5-triazinium) monodrogenphosphate dihydrogenphosphate tétrahydraté ($3C_3H_7N_6^+.HPO_4^{2-}.H_2PO_4^-.4H_2O$) et le 2,4,6-triamino-1,3,5-triazinium perchlorate monohydraté ($C_3H_8N_6^+.ClO_4^-.H_2O$), ont été synthétisés, leurs structures ont été affinées par diffraction des rayons X sur monocristal, la structure supramoléculaire 3D a été étudiée sur la base des données SXRD. De plus, la spectroscopie UV-visible et FT-IR a été utilisée pour établir les propriétés optiques et vibrationnelles. L'étude de la décomposition thermique de ces matériaux hybrides a également été réalisée par des techniques TGA/DTG. Ces hybrides ont été examinés comme inhibiteurs de corrosion en utilisant des méthodes électrochimiques. Les propriétés électrochimiques ont été étudiées par voltamétrie cyclique. Ces inhibiteurs sont efficacement adsorbés par un processus de chimisorption à la surface de l'acier. L'adsorption de ces composés suit l'isotherme de Langmuir dans le milieu étudié. Les résultats montrent que ces composés ont une bonne réactivité et une efficacité d'inhibition élevée.
Mots clés : Matériau ionique hybride, Mélamine, Stabilité thermique, Inhibiteur de corrosion, Acier